

Shock-Induced Damage in Rocks: Application to Impact Cratering

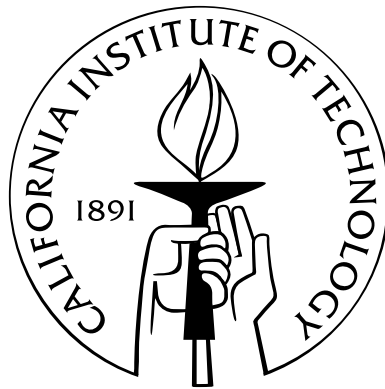
Thesis by

Huirong Ai

In Partial Fulfillment of the Requirements

for the Degree of

Doctor of Philosophy



California Institute of Technology

Pasadena, California

2006

(Defended May 8, 2006)

© 2006

Huirong Ai

All Rights Reserved

To My Parents

Acknowledgements

I would like to express my sincere gratitude to my thesis advisor, Thomas Ahrens, who gave me the chance to explore the shockwave field, and supported me both spiritually and financially, in a very generous way, through the past years. His enthusiasm toward science, and amazing supervision over the group have always impressed me and will benefit my career in the future.

I need extend my greatest gratitude to my thesis committee, Jason Saleeby, who is also my academic advisor, Rob Clayton, and Guruswami Ravichandran for their trust, understanding, support, encouragement, and valuable feedback despite their busy schedules. Also thanks to Ken Farley for his support. Special thanks to Ravi for letting me use the ultrasonic apparatus in his lab.

This thesis would not have been possible without the support of the whole shockwave group. I express my appreciation to Mike Long, Papo Gelle, and Russell Oliver for their assistance with my experiments, as well as to Sue Yamada, for her excellent cooking, the inspiration on knitting and crocheting during free time, and her kindness to us international students. I benefited a lot from discussions with Andy Shen, Michael Willis, Mikhail Rashedy, Daoyuan Sun, Shenlian Luo, and Michael Heinrich. Also, the time spent at work became more enjoyable because of them.

I am very grateful to Joann Stock, Rob Clayton, and Mark Simons for the help during my oral projects. Especially to Joann and Rob for the support during my first three years, and their patience with the Manihiki paper, although I did not include it in this thesis.

I owe a lot to all the previous and present members of Seismological lab, in particular, Sidao Ni, Chen Ji, Kaiwen Xia, Magali Billen, Patricia Persaud, Leo Eisner, and Sarah Stewart, who were always patient to answer all kinds of questions I had. In the meantime, my journey at Caltech became so meaningful and enjoyable because of my officemates and my friends. Thank you for your company and sharing the great moments in my life.

Finally but foremost, I would like to express my deepest gratitude to my parents for their endless love, unconditional support, and the sacrifice they made for me all these years. Without them, it is impossible for me to reach this point of my life. And this dissertation is dedicated to them.

Abstract

Shock-induced damage beneath impact craters is studied in this work. Two representative terrestrial rocks, San Marcos granite and Bedford limestone, are chosen as test target. Impacts into the rock targets with different combinations of projectile material, size, impact angle, and impact velocity are carried out at cm scale in the laboratory.

Shock-induced damage and fracturing would cause large-scale compressional wave velocity reduction in the recovered target beneath the impact crater. The shock-induced damage is measured by mapping the compressional wave velocity reduction in the recovered target. A cm scale nondestructive tomography technique is developed for this purpose. This technique is proved to be effective in mapping the damage in San Marcos granite, and the inverted velocity profile is in very good agreement with the result from dicing method and cut open directly. But it is not a good method for Bedford limestone, since the wave attenuation is too high to have a recordable signal. Instead, dicing method is used for studying the shock-induced damage in Bedford limestone.

Both compressional velocity and attenuation are measured in three orthogonal directions on cubes prepared from one granite target impacted by a lead bullet at 1200 m/s. Anisotropy is observed from both results, but the attenuation seems to be a more useful parameter than acoustic velocity in studying orientation of cracks.

Our experiments indicate that the shock-induced damage is a function of impact conditions including projectile type and size, impact velocity, and target properties. Combined with other crater phenomena such as crater diameter, depth, ejecta, etc., shock-induced damage would be used as an important yet not well recognized constraint for impact history.

The shock-induced damage is also calculated numerically to be compared with the experiments for a few representative shots. The Johnson-Holmquist strength and failure model, initially developed for ceramics, is applied to geological materials. Strength is a complicated function of pressure, strain, strain rate, and damage. The JH model, coupled with a crack softening model, is used to describe both the inelastic response of rocks in the compressive field near the impact source and the tensile failure in the far field. The model parameters are determined either from direct static measurements, or from indirect numerical adjustment. The agreement between the simulation and experiment is very encouraging.

Contents

Acknowledgements	iv
Abstract	vi
1 Introduction and Background	1
1.1 Background	1
1.2 Organization of this dissertation	4
2 Dynamic Tensile Strength of Terrestrial Rocks	5
2.1 Introduction	5
2.2 Significance and lithologies of rocks	6
2.3 Experimental techniques	8
2.4 Results and discussion	13
2.4.1 Reduction of velocity by cracks	26
2.4.2 Interpretation of V_p/V_s	29
2.4.3 Strain-rate effect	30
2.5 Conclusion	32
3 Tomography Study of Shock-Induced Damage beneath Craters	34

3.1	Introduction	34
3.2	Experimental procedure	35
3.2.1	Cratering	35
3.2.2	Tomography technique	35
3.3	Results and discussion	41
3.3.1	Tomography inversion	41
3.3.2	Test problems	43
3.3.3	Experimental results	47
3.4	Concluding remarks	61
4	Effects of Shock-Induced Cracks on the Ultrasonic Velocity and Attenuation in Granite	62
4.1	Introduction	62
4.2	Experimental technique	64
4.3	Experimental results	69
4.3.1	Compressional wave velocity measurements	69
4.3.2	Attenuation measurements	74
4.4	Analysis and discussion	76
4.5	Concluding remarks	84
5	Scaling Law	86
5.1	Introduction	86
5.2	Dimensional analysis	87
5.3	Experimental data and discussion	90

5.4	Summary	102
6	Shock-Induced Damage beneath Oblique Impact Craters	104
6.1	Introduction	104
6.2	Experiments	107
6.3	Results and discussion	107
6.3.1	Experimental results	107
6.3.2	Discussion	115
6.4	Conclusion	119
7	Numerical Modelling of Shock-Induced Damage for Granite under Dynamic Loading	121
7.1	Introduction	121
7.2	Related work	123
7.2.1	An overview of AUTODYN	123
7.2.2	Description of brittle material model	124
7.2.2.1	JH-2 model	124
7.2.2.2	Tensile crack softening model	127
7.3	Determination of model constants for granite	128
7.3.1	Pressure	128
7.3.2	Strength	131
7.3.3	Damage	133
7.3.4	Tensile cracking softening	134
7.4	Examples	134

7.4.1	Lead bullet impacting granite	134
7.4.2	Copper ball impacting granite	140
7.4.3	Plate impact of Al flyer plate into granite	140
7.4.4	Oblique impact	141
7.4.5	Effect of gravity on damage and cracks	146
7.5	Conclusion	146
8	Future Work	148

List of Figures

1.1	Schematic illustration of pressure near site of an impact by a projectile at 10 km/s and its implication for final state of target.	3
2.1	One-dimensional impact setup showing recovery tank, sample, and alignment.	10
2.2	Recovered samples showing radial and spall cracks.	14
2.3	Velocity measurements for San Marcos gabbro experiments.	21
2.4	Velocity measurements for San Marcos granite experiments.	22
2.5	Velocity measurements for Sesia eclogite experiments.	23
2.6	Velocity measurements for Coconino sandstone experiments of duration time of (a) 2.4 μ s and (b) 1.4 μ s. Dashed lines indicate the same as those in Figure 2.5.	24
2.7	Velocity measurements for Bedford limestone. (a) 0.5 μ s and (b) 1.3 μ s. (From <i>Ahrens and Rubin</i> [1993], Fig. 2.)	25
2.8	Post-shot V_p/V_s values versus computed tensile stress.	27
2.9	Normalized tensile strengths as a function of strain rate for ice and rocks. . .	32
3.1	(a) Cross section of tomography measurement setup; (b) Enlarged side view of position of 0.08 cm diameter steel impactor sphere.	36
3.2	Typical ultrasonic source and receiver signal.	37

3.3	Tomographic straight ray diagram for pre-shot San Marcos granite.	39
3.4	Tomographic straight ray diagram for post-shot San Marcos granite.	40
3.5	Test of the cm-scale tomography method developed above using a homogeneous velocity structure. (a) Forward velocity model. Velocity of the 20x15 cm structure is 6.4 km/s; (b) Inverted velocity structure using the tomography method with straight ray assumption.	45
3.6	Test of the cm-scale tomography method developed above using a heterogeneous velocity structure. (a) Forward velocity structure; (b) Inverted velocity structure.	46
3.7	Inversion solution of compressional wave velocity structure of pre-shot San Marcos granite using straight ray deploy.	48
3.8	Compressional wave velocity structure of post-shot San Marcos granite of shot 117 from top surface to depth of 10 cm using straight ray deploy.	49
3.9	Diagram showing minimum travel time rule for a stress wave traveling between point A and point B.	50
3.10	51
3.10	Diagram of procedure to obtain minimum time path from source (S) to receiver (R).	52
3.11	Diagram showing a few typical curve ray paths using method described in Figure 3.10 and shown velocity model.	53
3.12	Comparison of straight ray and curve ray assumption for the second iteration.	54

3.13	Histogram of relative error to measured value. (a) For straight ray assumption; (b) For curve ray assumption, second iteration.	55
3.14	Histogram of relative error to measured value for curve ray assumption, fourth iteration.	56
3.15	Diagonal values of model resolution matrix. (a) Matrix plot of the 4 th iteration; (b) Comparison for four iterations, cells 1 to 200 (See Figure 3.3 for cell index).	57
3.16	Compressional wave velocity structure of post-shot San Marcos granite of shot 117 from top surface to depth of 10 cm.	58
3.17	Cross section of shot 117, recovered granite impacted by 3.2 g lead bullet at 1200 m/s showing different types of cracks and damage depth. Cracks highlighted by dye coolant.	59
4.1	Pulse transmission ultrasonic system (modified from <i>Weidner</i> [1987]).	64
4.2	Sketch of attenuation measurement system (modified from <i>Winkler and Plona</i> [1982]).	65
4.3	Typical ultrasonic record for attenuation measurements and spectral amplitude of signals.	67
4.4	Calculated relative spectral amplitude of signals. Peak amplitude for surface A happens at frequency ~ 4.5 MHz.	68
4.5	P wave velocities as a function of distance from z axis at indicated depths within sample. (a) x direction; (b) y direction; (c) z direction.	71

4.6 P wave velocities as a function of distance from z axis in x, y and z directions at 4.5 cm depth below surface. 72

4.7 Plot of all velocity measurements in three directions as function of distance from crater center. 73

4.8 Attenuation coefficients as a function of normalized radial distance from impact point for three directions. Lines are power decay fit of data. (a) x; (b) y; (c) z. 75

4.9 Schematic diagram showing effect of aligned cracks on elastic waves propagating at different directions. 77

4.10 Damage parameters as a function of normalized radial distance from impact point for three directions. Lines are power decay fit of data. 79

4.11 Crack densities inverted from measured P-wave velocity by using model of *O’Connell and Budiansky* [1974] as function of normalized radial distance from impact point for three directions. Lines are power decay fit of data. (a) x; (b) y; (c) z. 81

4.12 Attenuation coefficients versus damage parameter for three directions. (a) x; (b) y; (c) z. Lines are linear fit of data. 82

5.1 Shot 1208, granite impacted by ~25 g lead ball (with sabot) at 800 m/s. Scale is 5 cm. 96

5.2 Shot 1209, limestone impacted by ~16 g (with sabot) lead ball at 590 m/s. Scale is 5 cm. 97

5.3	Normalized crater damage depth by apparent projectile radius, D_d/a_{pa} , over projectile-density ratio, ρ_p/ρ_t , as power-law function of strength parameter, $\pi_3 = Y/\rho_t U^2$	99
5.4	Normalized crater volume by apparent projectile volume, $\rho_t V/m$ as a function of strength parameter, π_3	100
5.5	Plot of crater depth as a function of crater diameter. Linear relation is observed, and slope is 0.12.	101
6.1	Peak shock pressure contours in the plane of impact for a series of 3D hydrocode simulations at various impact angles.	106
6.2	(a) Oblique impact geometry. Tomography measurement carried out on two central planes; (b) Diagram showing orientation for dicing method for limestone.	108
6.3	Inverted compressional wave profiles of two planes for oblique impact crater in San Marcos granite, shot No. 121, using tomography method.	110
6.4	Inverted compressional wave profiles of same central planes as in Figure 6.3, except that 1 cm top surface layer is cut off. See Figure 6.3 for explanation of <i>Vectors</i> . (a) Plane A; (b) Plane B.	111
6.5	Compressional wave profiles of two planes for oblique impact crater in Bedford limestone, shot 122, using dicing method.	115
6.6	Compressional wave profiles of plane B for shot 122 using dicing method. All notes same as in Figure 6.5. (a) x direction; (b) z direction. Asymmetry is not observed.	116

7.1	Description of JH2 model for brittle materials (from <i>Johnson and Holmquist</i> [1999], Figure 1).	125
7.2	Strength, damage, and fracture under a constant pressure and strain rate for the JH2 model (from <i>Johnson and Holmquist</i> [1999], Figure 2).	127
7.3	Test data and model for shock pressure-volume response of granite.	130
7.4	Test data and model for strength of intact and damaged granite.	131
7.5	(a) Initial setup for simulating shot 117, lead bullet into 20x20x15 cm granite block at velocity of 1.2 km/s, and location of gauge points; (b) Peak pressure of gauges versus normalized distance from impact. r is distance, a is radius of projectile. Red line is exponential fit of data.	136
7.6	Simulated damage contour for shot 117 at several times during impact event.	137
7.7	Cross section of granite impacted by lead bullet at 1200 m/s illustrating crack distribution. Normal impact. (a) Experimental result; (b) AUTODYN-2D simulation at 0.03 ms. Left panel illustrates material status; right panel illustrates damage.	138
7.8	Cross section of granite impacted by copper ball at 690 m/s. Normal impact. (a) experimental result; (b) simulation at 0.04 ms. Others are the same as in Figure 7.7b.	139
7.9	Simulated damage for plate impact of Aluminum flyer plate into San Marcos granite at different velocities. Flyer plate not shown here.	142
7.10	Cross section of granite impacted by copper ball at 1000 m/s, experimental result. <i>Vector</i> shows impact angle at 45° . Visible tensile cracks are highlighted.	143

7.11	Simulated result at 0.1 ms for shot shown in Figure 7.10.	144
7.12	Simulated result shown effect of gravity on formation of tensile cracks. Normal impact. (a) 500 g, $a_p=3$ mm; (b) 1 g, $a_p=1500$ mm. Left panel illustrates material status, right panel for damage status. Notice different scales on the two plots. See text for discussion.	145

List of Tables

2.1	Mineralogical composition of San Marcos granite	7
2.2	Physical properties of experimental materials	9
2.3	One-dimensional tensile strain impact parameters and pre-shot and post-shot ultrasonic compressional and shear velocities.	15
2.4	Tensile strengths (in MPa) of ice and rocks at different strain rates.	31
4.1	Compressional wave velocity beneath impact crater in San Marcos granite, shot 117.	70
5.1	Summary of experimental parameters	91
6.1	Compressional wave velocity beneath oblique impact crater in Bedford lime- stone, shot 122, plane A, along projectile trajectory.	113
6.2	Compressional wave velocity beneath oblique impact crater in Bedford lime- stone, shot 122, plane B, Normal to projectile trajectory.	114
7.1	JH2 baseline and crack softening constants for granite	129
7.2	One-dimensional impact parameters, as well as pre- and post-shot compres- sional wave velocities for Al2024 flyer plate into San Marcos granite.	133

Chapter 1

Introduction and Background

1.1 Background

Impact cratering is a universal process in the solar system. Significant geophysical features for impact craters include gravity and magnetic anomaly, electrical property change of rocks such as resistivity below impact craters, seismic profiles showing low velocity zone, etc [Pilkington and Grieve, 1992]. These features are caused directly or indirectly by the precedence of shock-induced damage and cracks in rocks beneath the crater, which in turn are related to the pressure profiles in the impacted targets.

The peak shock pressure in an impacted target displays four regimes [Ahrens and O'Keefe, 1987]. Regime 1 is the impedance match regime, extending to a few projectile radii into the target, where the peak shock pressure is roughly given by the planar impedance match method [Ahrens, 1987]. Since materials achieve peak shock pressure, rock is vaporized upon impacts of >10 km/s, melted upon impact of >5 km/s and is massively powdered at >1 km/s. Regime 2 is the shock decay regime, which extends to the distance where the pressure equals the Hugoniot elastic limit (HEL) of the target. Pressure in this regime at distance r from the impact point, P_r , follows the relation [Ahrens and

O'Keefe, 1987]:

$$P_r = P_0 (r/r_0)^{-n} \quad (1.1)$$

where r_0 is the radius of the projectile and n is the attenuation index. For nonporous silicate projectile and target, n is defined as:

$$n \cong -0.625 \log_{10} U - 1.25 \quad (1.2)$$

where U is the impact velocity. Shear and concentric cracks are formed in this regime. Beyond this is regime 3, the elastic decay regime. The magnitude of tensile stress in this regime is in the same order of the shear stress [*Shibuya and Nakahara*, 1968], and radial tensile cracks are produced when the tensile tangential stress exceeds the dynamic tensile strength of the material. Regime 4 is the spalling region near the surface. *Melosh* [1989] has a similar definition for an impact at 10 km/s into the rock target: I. melting; II. region where pressure exceeds HEL; III. Grady-Kipp fragments region, which is defined to be resulted from dynamic tensile stress; IV. spalling region (Figure 1.1).

Damage and cracking in a fractured body reduce the effective elastic moduli of the media, which in turn reduce the elastic velocities [e.g. *O'Connell and Budiansky*, 1974; *Kachanov*, 1993]. Large scale reduction in compressional wave velocity from the intrinsic value caused by the shock-induced cracking of rocks beneath impact craters has long been recognized both in the field [*Ackermann et al.*, 1975; *Pohl et al.*, 1977], and in small-scale craters in the laboratory [*Ahrens and Rubin*, 1993; *Xia and Ahrens*, 2001]. For the Moon, the whole crust suffers shock-induced damage according to *Simmons et al.* [1973].

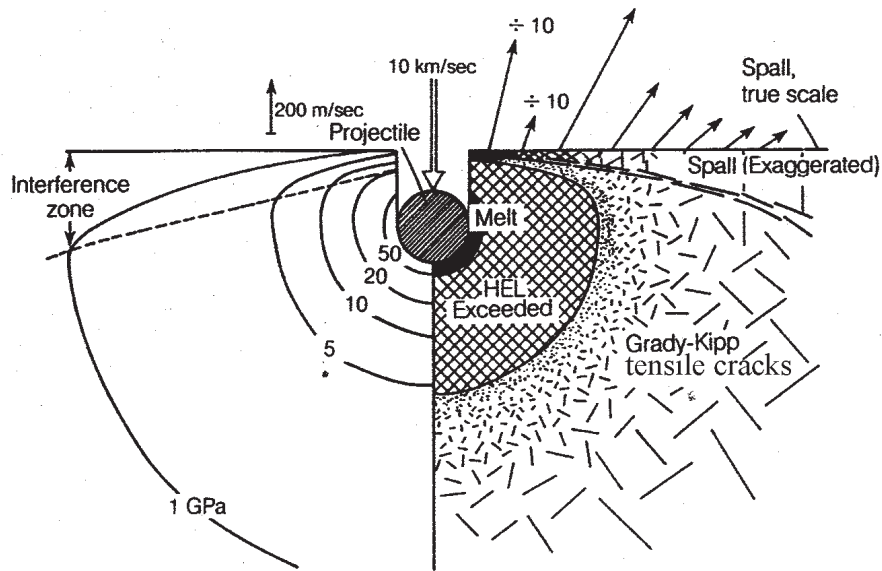


Figure 1.1: Schematic illustration of pressure near the site of an impact and its implication for final state of target. Tensile stresses break rock into Grady-Kipp fragments to great depths below impact site. (From *Melosh* [1989], Figure 5.4, p. 64).

Xia and Ahrens [2001] performed preliminary impact cratering recovery experiments and mapped the damage zones using ultrasonic measurements based on the fact that the shock-induced damage beneath the impact craters would cause large scale compressional wave velocity deficit in the target rocks. They suggested that shock-induced damage and cracking beneath craters, if combined with other constraints such as crater dimension, physical properties of target and projectile obtained from field mapping, could provide important information about the impact conditions.

However, the shock-induced damage beneath impact craters as a potential constraint has not been systematically studied yet. In this work, study of shock-induced damage beneath craters is carried out at cm scale in the laboratory. Two types of rocks, San Marcos granite and Bedford limestone, are chosen in this work for damage study, since they are representative of crustal rocks. In parallel, numerical simulation is performed and compared with

experimental results.

1.2 Organization of this dissertation

From the discussion above, the dynamic fracture behavior of rocks plays an important role in the impact process. For this reason, determination of dynamic tensile strength for four representative terrestrial rocks is first discussed in chapter 2. Chapter 3 describes the newly developed cm scale nondestructive tomography method for mapping the low velocity zone caused by the shock-induced damage and fracturing. The inverted compressional wave velocity profile of one shot, lead bullet launched into a granite target at 1200 m/s, is also shown and compared with the experimental result. After tomography mapping, the same recovered granite target is cut open, and 1 cm cubes are prepared from the center plane for ultrasonic velocity and attenuation measurement. Both results from dicing are presented and discussed in chapter 4. Chapter 5 presents the damage data for the shots carried on in this work for both granite and limestone. A simple scaling law is obtained from the experiments. All the shots in chapter 5 are performed at a vertical angle to the impact surface. However, natural impact craters always happen at impact angles less than vertical [*Gilbert*, 1893; *Shoemaker*, 1962]. Therefore, a few oblique impacts are carried out to study the effect of impact angles on shock-induced damage. Damage information for these oblique impacts is presented in Chapter 6. The last chapter explores the numerical simulation of damage below impact craters. Johnson-Holmquist [*Johnson and Holmquist*, 1999] strength model is applied to geological materials for the first time. Several calculations are done and compared with available experimental data.

Chapter 2

Dynamic Tensile Strength of Terrestrial Rocks

2.1 Introduction

The dynamic fracture behavior of rocks plays an important role in fracturing and fragmentation procedures, which vary from industrial processes, such as coal and oil shale fragmentation [Murri *et al.*, 1977], quarrying and mining operations [Carter, 1978], impact or explosive crater formation [O'Keefe and Ahrens, 1976], and accretion of planetesimals in the early stages of planetary formation [Matsui and Mizutani, 1977].

Dynamic tensile strength experiments on rocks have been carried out by Grady and Hollenbach [1979], Cohn and Ahrens [1981], Lange *et al.* [1984], Ahrens and Rubin [1993] and others. Previously, three quantitative methods have been used to determine the dynamic tensile strength. These are: (1) the free-surface velocity pullback signal method [Grady and Hollenbach, 1979]; (2) terminal examination [Cohn and Ahrens, 1981; Lange *et al.*, 1984]; and (3) ultrasonic post-impact examination [Ahrens and Rubin, 1993]. The free-surface velocity pullback signal method measures the drop in the target's free-surface velocity upon arrival of the compression wave generated by an expanding tensile crack to

determine tensile strength. Method 2 involves microscopic examination of polished thin section made from the recovered samples to determine the incipient spall cracks produced by impact. The stress above which microscopically observable cracks appear is assumed to be the dynamic tensile strength. Post-impact ultrasonic examination measures the pre- and post-shot ultrasonic velocities of the samples and relates the shock-induced damage in rocks to shock-induced one-dimensional tensile stresses. The tensile strengths determined by the free-surface velocity pullback signal method and the terminal examination depends crucially on the properties along the narrow zone of tensile failure where the rock fractures. Moreover we note that the sample-cutting process required to examine recovered samples in method 2 could produce additional damage. The ultrasonic method is a superior method and it is a volume measurement. This method measures crack density instead of the properties of a single crack. For this reason, ultrasonic method 3 is chosen to determine the tensile strength in this work.

Quantitative data on the tensile behavior of many types of rocks and its dependence on strain rate are still lacking. In this study we selected two igneous rocks (San Marcos gabbro and granite), one sedimentary rock (Coconino sandstone) and one metamorphic rock (Sesia eclogite) for determination of the dynamic tensile strength using method 3 above.

2.2 Significance and lithologies of rocks

San Marcos gabbro from Escondido, a well-studied rock [*Lange et al.*, 1984; *Ahrens and Rubin*, 1993; *Xia and Ahrens*, 2001], is chosen for comparison with previous studies. *Lange et al.* [1984] reported that the density of this rock is 2.867 g/cm^3 , the dynamic tensile

strength is 150 MPa, the compressional wave velocity (V_p) is 6.36 ± 0.16 km/s, and it has very low initial crack density. The mineral composition of San Marcos gabbro is 67.9% plagioclase, 22.5% amphibole, 2.6% pyroxene, 1.4% quartz and some trace elements [Lange *et al.*, 1984].

San Marcos granite is also chosen because this is the rock target used for this project. This intrusive granite has the same originality (Escondido, California) as San Marcos gabbro. Mineralogical composition obtained by Scanning Electron Microscopy (SEM) of the thin section for San Marcos granite is shown in Table 2.1. The grain size of quartz and plagioclase is 1 to 2 mm, intergrown with dark minerals including amphibole and some biotite grains, size of which is 1 to 2 mm. On a microscopic level, the rock is essentially crack-free except for microcracks along grain boundaries. The density of San Marcos granite is 2.657 g/cm³, the intrinsic compressional wave velocity (C_p) is 6.31 ± 0.1 km/s, determined at 1 MHz.

Table 2.1: Mineralogical composition of San Marcos granite

Mineral	Area (%)
Quartz	20.9
Plagioclase	51.0
Amphibole	25
Biotite	0.9
Fe ₂ O ₃	0.9
Alkali feldspar	trace
Total	98.7

The dynamic tensile strength of Coconino sandstone from Meteor Crater, Arizona is of interest, as Coconino sandstone is one of the main sedimentary rock types of the crater [Shoemaker, 1963]. The subsurface strata of Meteor Crater have been studied in a refraction survey [Ackermann *et al.*, 1975]. Roddy *et al.* [1980] simulated the formation of this

crater. However, previously only dynamic compressive experiments at different strain rates were performed by *Ahrens and Gregson* [1964] and *Shipman et al.* [1971] on this type of rock. The block from which the samples are made is yellowish-gray or cream colored, contains sub-parallel laminae that are separated by thin laminae containing more than average amounts of silt and clay sized grains. Cross-bedding can be seen clearly on the cutting surfaces. Coconino sandstone is composed of 97% quartz, 3% feldspar, with traces of clay and heavy minerals [*Ahrens and Gregson*, 1964]. Average grain size is in the range of 0.12-0.15 mm and porosity is 24-25% [*Ahrens and Gregson*, 1964; *Shipman et al.*, 1971]. The bulk density of our samples was $2.08 \pm 0.03 \text{ g/cm}^3$, slightly higher than that reported by *Ahrens and Gregson* [1964] and *Shipman et al.* [1971] of 1.99 g/cm^3 . Impact and ultrasonic wave measurements are all normal to the bedding of the sandstone. Eclogite is chosen because it may represent the upper limit of dynamic tensile strength available for terrestrial rocks. The eclogite from Sesia zone of the Austroalpine system in Italy is metamorphic. Thin section analysis of the rock sample shows that it contains 40% garnet, 45% clinopyroxene, 4% mica, trace feldspar and opaques. Grain size is $1 \sim 1.5 \text{ mm}$, and the bulk density is $3.44 \pm 0.04 \text{ g/cm}^3$.

The physical properties of the four types of rocks are listed in Table 2.2.

2.3 Experimental techniques

The dynamic tensile strengths of the San Marcos gabbro, Coconino sandstone, and Sesia eclogite were determined by planar impact experiments using a 40 mm compressed gas gun, similar to that described in [*Cohn and Ahrens*, 1981]. A Lexan projectile carrying a

Table 2.2: Physical properties of experimental materials

Material	Average ρ , g/cm ³	C_p , km/s	C_s , km/s
San Marcos gabbro	2.867 ²	6.65 ¹ 6.36 ²	3.57 ¹
San Marcos granite	2.66 ¹	6.4 ¹	3.57 ¹
Coconino sandstone (velocity normal to bedding)	2.08 ¹ 1.99 ³	2.81 ¹	1.82 ¹
Sesia eclogite	3.44 ¹	6.40 ¹	3.78 ¹
PMMA	1.2	2.8	
Aluminum 2024	2.78	6.36	

Sources: ¹This study; ²Lange *et al.* [1984]; ³Ahrens and Gregson [1964].

polymethyl methacrylate (PMMA) or aluminum (Al) flyer plate at its front is accelerated by the expansion of precompressed air to velocities in the 5 to 60 m/s range (Figure 2.1). The initial impact produces compressional shock waves propagating forward into the target and back into the flyer plate. These compressional waves then reflect back as relief waves from the free surfaces of the target and the flyer plate. Tension is produced when the two relief waves meet within the sample. We assume that the magnitude of the tensile stress is equal to that of the original compressive stress, and the initial compressive pulse produced no detectable damage. When the peak tensile stress exceeds the dynamic tensile strength of the rock, cracks start to occur within the sample.

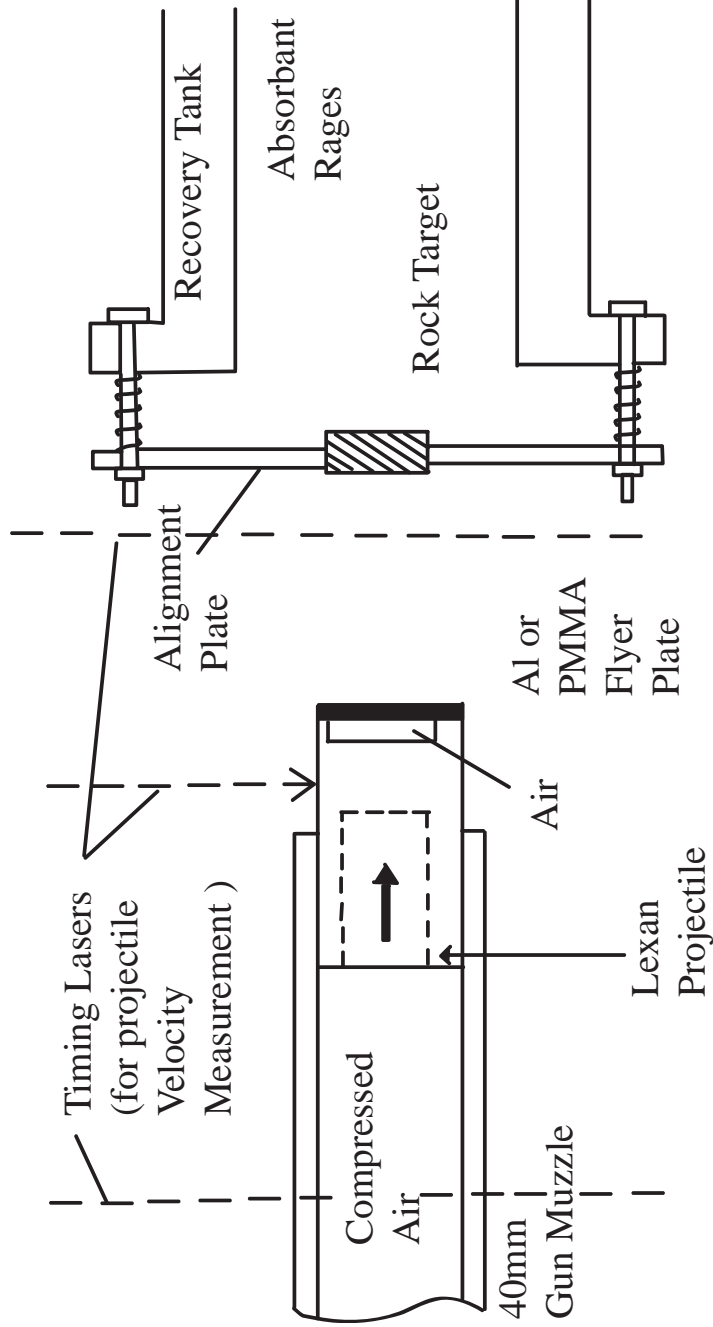


Figure 2.1: Sketch of one-dimensional impact setup showing recovery tank, sample, and alignment. Discs of rock 22 ~ 23 mm in diameter and 6.5 ~ 7 mm in thickness were inserted into a steel alignment plate. Lexan projectiles fitted with Aluminum (Al) or polymethylmethacrylate (PMMA) flyer plates impacted the sample. Velocity of projectile is determined by laser beams. Following impact rock target flies into a cloth recovery tank, where it is protected from further damage.

The choice of PMMA or Al flyer plates depends on the impedances of the rock, defined as the product of the density, ρ , and the compressional velocity, V_p . Al flyer plates are used for San Marcos Gabbro and Sesia Eclogite, with impact velocities of 13 to 30 m/s, and 24 to 60 m/s respectively. PMMA flyer plates are used for Coconino sandstone, with impact velocities of 5 to 22 m/s. The impact velocities are controlled by varying the pressure of the compressed air. Different impact velocities result in different amplitude tensile stresses. The impact velocity is measured in air by the sequential interruption of three laser beams. The impacted target flies free into a recovery tank, where loose rags prevent further damage.

The targets are shaped as discs with diameters of 22 to 23 mm and thickness of 6.5 to 7 mm. Front and rear surfaces are polished. The achieved parallelism of the sample surfaces was ± 0.003 mm for San Marcos gabbro and Sesia eclogite. Surface parallelism ensures that the strain in the ~ 1 cm central region of the sample is approximated by a one-dimensional strain condition. Less parallelism, ± 0.03 mm, was achieved for Coconino sandstone due to its high porosity. This partially explains the relatively large data scatter of ultrasonic measurements for sandstone. Samples of San Marcos gabbro and Sesia eclogite are cut wet and vacuum-dried for 24 hours before the experiments, while samples of Coconino sandstone are cut dry, to avoid changes in the physical properties of the sample.

In our experiments, the impedance of the flyer plate is less than that of the target, resulting in the separation of target and flyer plate [Ahrens and Rubin, 1993]. The tensile stress (σ) within the target is given by the acoustic formula [Cohn and Ahrens, 1981]:

$$\sigma = U_p \frac{\rho_t V_{pt} \rho_i V_{pi}}{\rho_i V_{pi} + \rho_t V_{pt}} \quad (2.1)$$

where U_p is the projectile velocity, V_p is the compressional seismic velocity, ρ is density, and the subscripts i and t refer to the projectile and target, respectively. The individual density of each sample is used for stress calculation.

The duration time (t_d) of the shock can be approximated by:

$$t_d = \frac{2d_i}{V_{pi}} \quad (2.2)$$

where d_i is the thickness of the flyer plate.

Pre-shot and post-shot ultrasonic P and S wave velocities were measured for the targets using the ultrasonic pulse transmission method. The reduction of the velocity gives a measure of degradation of the modulus of a micro-cracked body. The P-wave transducers are Model V103, Panametrics; the S-wave transducers are Model V153, Panametrics. The frequency of transducers used for both wave measurements is 1 MHz. The minimum crack size that the P-wave transducers can detect is about one half of the wavelengths of the ultrasonic waves in the media [Heinrich, 1991]. That is, ~ 2 mm for San Marcos gabbro and Sesia eclogite, and ~ 1 mm for Coconino sandstone. A Caltech-made high-voltage pulser with rise time about $10 \mu\text{s}$ is used as transducer driver. A digital oscilloscope (Gould 4074) is used to record the ultrasonic signals. Panametrics couplant D-12 is used for P-wave measurements and Panametrics couplant SWC is used as S-wave measurements. Alcohol and water were used as P- and S-wave couplant removers, respectively. Aluminum foil (thickness of 0.03 mm) is placed between the sample and the transducers to prevent the samples from being contaminated by the couplants and couplant removers. All the impacts were performed at room temperature and atmospheric pressure.

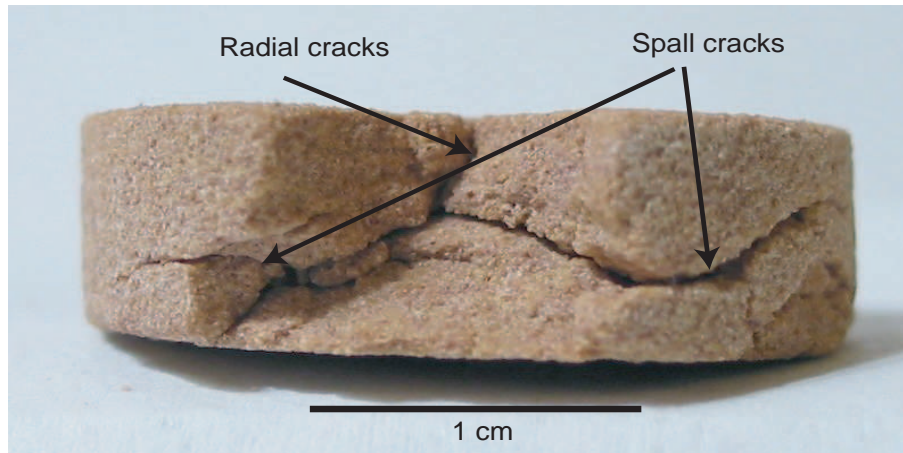
We define the dynamic tensile strength of the rock as the peak stress above which tensile cracks are observed from a decrease in P or S wave velocities, and the fracture strength is the peak stress above which complete fragmentation happens. According to *Ahrens and Rubin* [1993], a 2% reduction in P-wave velocity, or 3% increase in the radii of the largest cracks present, which corresponds to an increase in crack density of 0.016, is the minimum that could be detected by the ultrasonic method. Here crack density is expressed as:

$$\varepsilon = N \langle a^3 \rangle \quad (2.3)$$

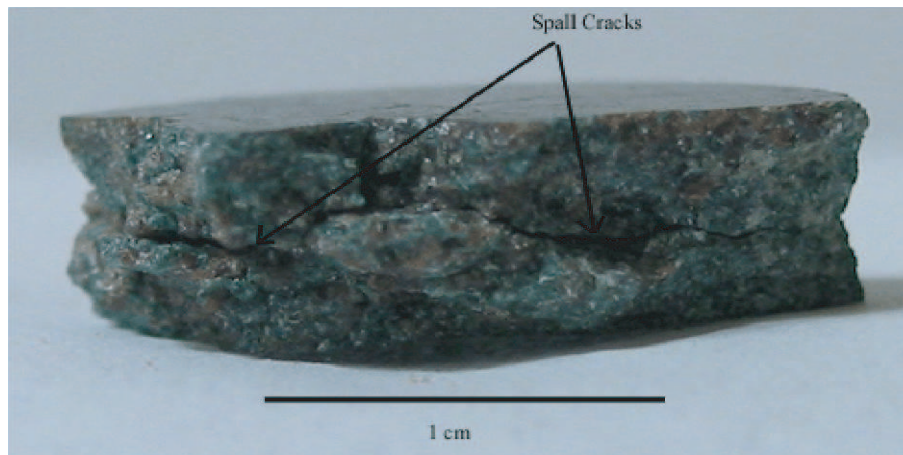
(3) where N is the number of cracks per unit volume and $\langle a^3 \rangle$ is the average of the cube of the crack radii [e.g. *Kachanov*, 1993; *O'Connell and Budiansky*, 1974; *Wepfer and Christensen*, 1990].

2.4 Results and discussion

Figure 2.2 shows the spall cracks observed in the recovered samples. Both pre-shot and post-shot ultrasonic compressional and shear wave velocities in the direction perpendicular to the impact surface, and V_p/V_s are listed in Table 2.4, as well as impact velocities and relative tensile stresses for our experiments. Figure 2.3 to 2.6 show velocity reductions with tensile stresses for the four types of rocks and Figure 2.8 is V_p/V_s ratio versus tensile stresses. Several important effects are identified below:



(a)



(b)

Figure 2.2: Recovered samples: a) CS 27; b) One fragment of SE 5 to show the radial and spall (subhorizontal) cracks observed. The measured velocity reduction of (a) was $\sim 36\%$ and $\sim 40\%$ for P and S wave velocities. The velocity reduction for (b) was unmeasurable.

Table 2.3: One-dimensional tensile strain impact parameters and pre-shot and post-shot ultrasonic compressional and shear velocities.

Shot ^a	Sample ^b	Flyer plate	Projectile		Tensile		Pre-shot		Post-shot		
			velocity	stress	MPa	V_p , km/s	V_s , km/s	V_p/V_s	V_p , km/s	V_s , km/s	V_p/V_s
G23	SMG#21	Al	15.62	147.27	147.27	6.908	3.538	1.95	6.434	3.519	1.83
G24	SMG#22	Al	16.97	159.61	159.61	6.833	3.647	1.87	6.524	3.538	1.84
G26	SMG#25	Al	25.19	227.69	227.69	6.533	3.479	1.88	6.05	3.347	1.81
G28	SMG#28	Al	27.89	253.66	253.66	6.427	3.496	1.84	4.936	3.156	1.56
G29	SMG#29	Al	28.53	272.43	272.43	7.137	4.683	1.52	fragmented	–	–
G30	SMG#30	Al	23.78	222.58	222.58	6.84	3.618	1.89	5.9	3.337	1.77
G31	SMG#31	Al	32.11	297.15	297.15	6.687	3.506	1.91	fragmented	–	–
G32	SMG#32	Al	26.61	247.07	247.07	6.727	3.609	1.86	5.588	3.38	1.65

Table 2.3: (continued)

Shot ^a	Sample ^b	Flyer plate	Projectile		Tensile		Pre-shot		Post-shot	
			velocity m/s	stress MPa	V_p , km/s	V_s , km/s	V_p/V_s	V_p , km/s	V_s , km/s	V_p/V_s
G34	SMG#34	Al	20.1	184.7	6.526	3.474	1.88	6.017	3.379	1.78
G35	SMG#24	Al	13.74	125.89	6.483	3.509	1.85	6.483	3.509	1.85
Ga1	R-Ga#1	Al	19	172.01	6.6	3.38	1.95	5.67	3.33	1.7
Ga3	R-Ga#3	Al	29.93	271.09	6.64	3.65	1.82	fragmented	–	–
Ga5	R-Ga#5	Al	27.85	242.5	6.11	3.45	1.77	4.79	3.0	1.6
Ga7	R-Ga#7	Al	15.57	139.78	6.5	3.5	1.85	5.61	3.41	1.65
Ga8	R-Ga#8	Al	27.06	237.22	6.2	3.6	1.72	4.95	3.09	1.6
Ga9	R-Ga#9	Al	22.66	199.68	6.25	3.52	1.77	5.59	3.22	1.74
Ga11	R-Ga#11	Al	13.47	120.79	6.45	3.66	1.75	6.49	3.47	1.87
Ga12	R-Ga#12	Al	16.37	146.33	6.46	3.62	1.79	6.21	3.44	1.81

Table 2.3: (continued)

Shot ^a	Sample ^b	Flyer plate	Projectile		Tensile		Pre-shot		Post-shot			
			velocity	stress	V_p , km/s	MPa	V_p , km/s	V_s , km/s	V_p/V_s	V_p , km/s	V_s , km/s	V_p/V_s
			m/s									
Ga13	R-Ga#13	Al	24.98	220.24	6.26	3.51	3.51	1.78	5.67	3.22	1.76	
CS8	CS#10	PMMA	22.068	45.26	2.819	1.807	1.807	1.56	fragmented	–	–	
CS9	CS#11	PMMA	21.176	44.05	2.937	1.844	1.844	1.59	fragmented	–	–	
CS10	CS#12	PMMA	20.087	40.94	2.748	1.921	1.921	1.43	fragmented	–	–	
CS11	CS#13	PMMA	16.63	34.54	2.864	1.88	1.88	1.52	1.998	1.299	1.54	
CS12	CS#14	PMMA	18.63	38.99	2.934	1.906	1.906	1.54	1.99	1.476	1.35	
CS13	CS#15	PMMA	15.33	31.32	2.77	1.831	1.831	1.51	2.084	1.482	1.41	
CS14	CS#16	PMMA	13.72	28.08	2.74	1.735	1.735	1.58	2.593	1.51	1.72	
CS15	CS#17	PMMA	11.5	23.69	2.795	1.729	1.729	1.62	2.594	1.515	1.71	
CS16	CS#18	PMMA	8.704	17.84	2.771	1.764	1.764	1.57	2.74	1.722	1.59	

Table 2.3: (continued)

Shot ^a	Sample ^b	Flyer		Projectile		Tensile		Pre-shot		Post-shot		
		plate	velocity m/s	stress MPa	velocity m/s	stress MPa	V_p , km/s	V_s , km/s	V_p/V_s	V_p , km/s	V_s , km/s	V_p/V_s
CS17	CS#19	PMMA	6.413	13.19	6.413	13.19	2.8	1.777	1.58	2.8	1.777	1.58
CS18	CS#20	PMMA	19.28	39.93	19.28	39.93	2.809	1.86	1.51	fragmented	–	–
CS19	CS#21	PMMA	14.923	30.55	14.923	30.55	2.78	1.783	1.56	1.841	1.23	1.5
CS20	CS#22	PMMA	18.476	38.6	18.476	38.6	2.907	1.873	1.55	fragmented	–	–
CS21	CS#23	PMMA	11.828	23.9	11.828	23.9	2.703	1.769	1.53	2.38	1.585	1.5
CS22	CS#24	PMMA	7.688	15.84	7.688	15.84	2.813	1.807	1.56	2.813	1.576	1.78
CS23	CS#25	PMMA	9.984	20.34	9.984	20.34	2.744	1.693	1.62	2.644	1.535	1.72
CS24	CS#26	PMMA	13.729	28.32	13.729	28.32	2.831	1.88	1.51	2.359	1.523	1.55
CS25	CS#27	PMMA	16.357	33.76	16.357	33.76	2.838	1.832	1.55	2.189	1.35	1.62
CS26	CS#28	PMMA	16	32.8	16	32.8	2.766	1.796	1.54	2.023	1.352	1.5

Table 2.3: (continued)

Shot ^a	Sample ^b	Flyer plate	Projectile		Tensile		Pre-shot		Post-shot		
			velocity m/s	stress MPa	V_p , km/s	MPa	V_p , km/s	stress MPa	V_p , km/s	V_s , km/s	V_p/V_s
CS27	CS#29	PMMA	16.709	34.67	2.855	1.845	1.55	1.826	1.11	1.65	
CS28	CS#30	PMMA	15.075	30.98	2.768	1.877	1.47	2.206	1.443	1.53	
SE1	SE#1	Al	60.077	578.12	6.096	3.81	1.6	fragmented	–	–	
SE2	SE#2	Al	48.93	471.34	6.083	3.883	1.57	3.139	2.51	1.25	
SE3	SE#3	Al	42.21	408.76	6.165	3.909	1.58	4.391	3.09	1.42	
SE4	SE#4	Al	33.226	340.7	7.008	3.976	1.76	5.69	3.725	1.53	
SE5	SE#5	Al	55.771	547.56	6.329	3.836	1.65	fragmented	–	–	
SE6	SE#6	Al	24.1	244.86	6.99	3.888	1.8	6.284	3.736	1.68	
SE7	SE#7	Al	38.068	372.15	6.486	3.884	1.67	4.143	3.144	1.32	
SE8	SE#9	Al	28.396	283.16	6.574	3.6	1.83	5.361	3.017	1.78	

Table 2.3: (continued)

Shot ^a	Sample ^b	Flyer	Projectile		Tensile		Pre-shot		Post-shot	
		plate	velocity	stress	m/s	MPa	V_p , km/s	V_s , km/s	V_p/V_s	V_p , km/s
SE9	SE#10	Al	45.92	430.55	5.855	3.389	1.73	3.231	2.38	1.36
SE10	SE#11	Al	30.138	286.37	6.047	3.45	1.75	5.023	2.917	1.72
SE11	SE#8	Al	24.79	246.86	6.771	3.934	1.72	0	3.53	0

^aDuration time is $\sim 1 \mu\text{s}$ for G23 to Ga13, SE1 to SE11; $\sim 2.4 \mu\text{s}$ for CS8 to CS17; $\sim 1.4 \mu\text{s}$ for CS18 to CS28. ^bSMG: San Marcos gabbro; Ga: San Marcos granite; CS: Coconino sandstone; SE: Sesia eclogite.

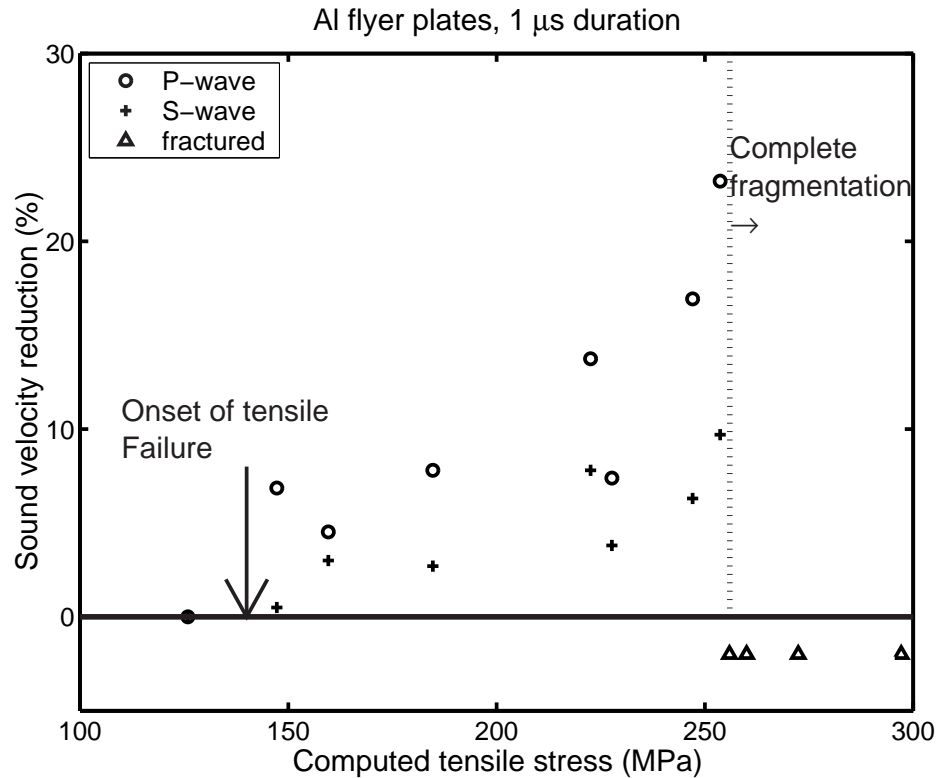


Figure 2.3: Velocity measurements for San Marcos gabbro experiments. Dashed line indicates pressure above which complete fragmentation occurred.

1. P- and S-wave velocity reductions occur with increasing tensile stress for the four types of rocks studied (Figures 2.3 to 2.6). The highest P-wave velocity reduction measured is 27-30% for San Marcos gabbro and granite, and 10-15% for S-wave velocity (Figure 2.3, 2.4). For Sesia eclogite measurements, the results are 48% and 35% for P- and S-wave reduction, respectively (Figure 2.5). In the Coconino sandstone experiment with 2.4 μ s duration time, 30% and 25% are obtained for P- and S-wave reduction, respectively, which increases to 36% and 40% for the 1.4 μ s duration time case (Figure 2.6a, b).
2. Figure 2.3 suggests that the onset of tensile failure of San Marcos gabbro determined

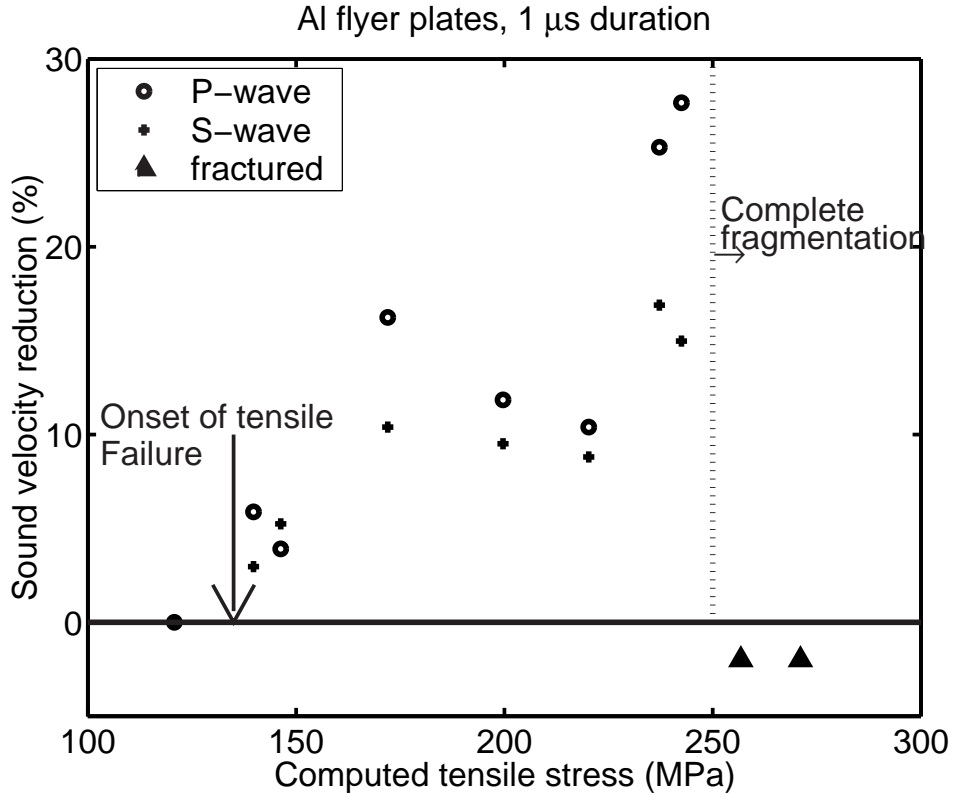


Figure 2.4: Velocity measurements for San Marcos granite experiments. Dashed line indicates pressure above which complete fragmentation occurred.

by the detectable ultrasonic velocity reduction is ~ 150 MPa. This result is comparable with a previous microscopic examination of recovered samples [Lange *et al.*, 1984]. Within this range, Lange *et al.* [1984] reported that incipient cracks, more or less continuous, were observed. This also validates the ultrasonic method for determining dynamic tensile strength. Complete fragmentation occurs above 250 MPa. This is determined to be the fracture strength.

3. Onset of tensile failure of San Marcos granite is ~ 130 MPa (Figure 2.4). Complete fragmentation occurs above 250 MPa, very close to that of San Marcos gabbro.
4. The onset of tensile failure for Sesia eclogite is ~ 240 MPa. This is the highest

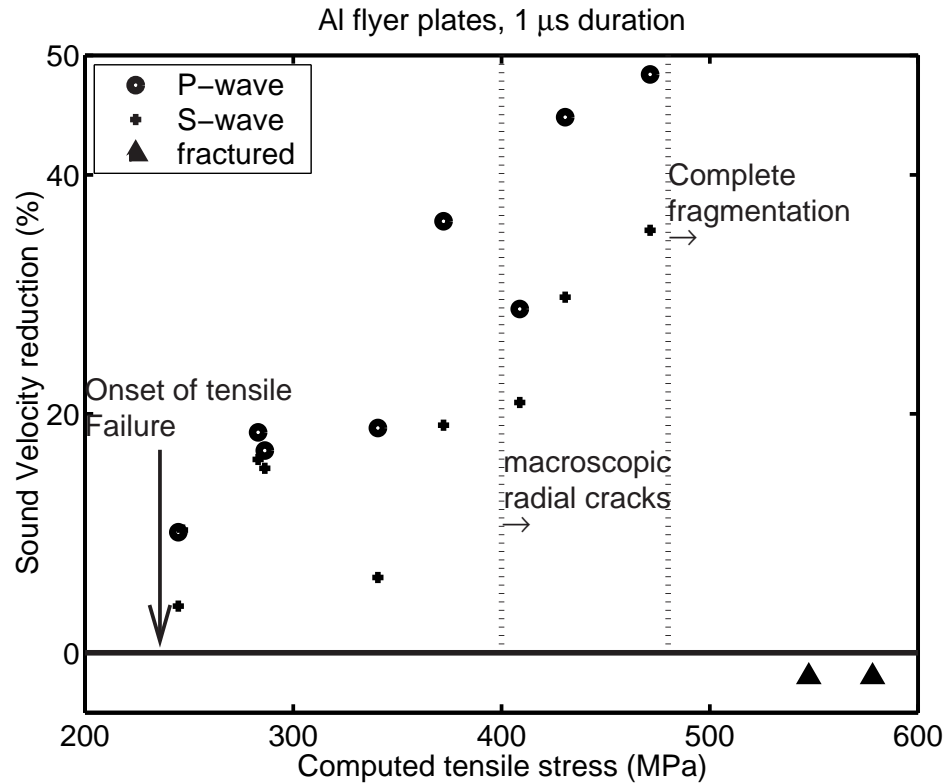
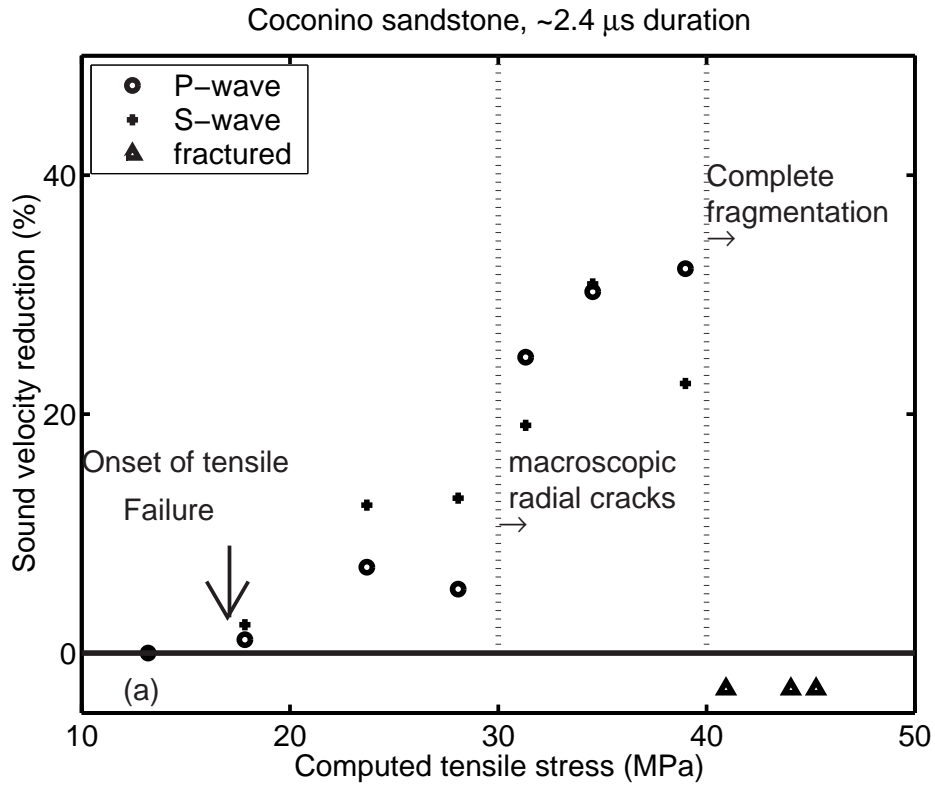


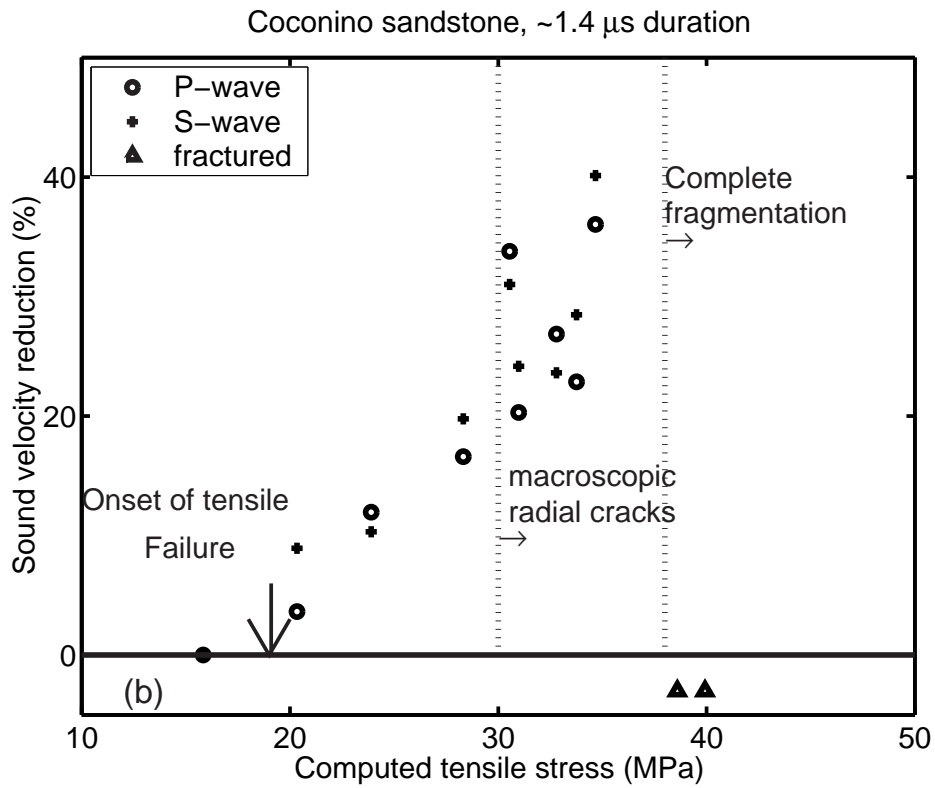
Figure 2.5: Velocity measurements for Sesia eclogite experiments. Dashed lines indicate pressure above which macroscopic radial and complete fragmentation occurred.

known limit of tensile strength measured by experiment for terrestrial rocks. The observable continuous cracks for Sesia eclogite appear around tensile stress about 400 MPa (Figure 2.5). Complete fragmentation occurs above ~ 500 MPa.

5. The onset of tensile failure for Coconino sandstone, determined from detectable ultrasonic velocity reduction, is ~ 17 MPa for the 2.4μ s shock duration time, and ~ 20 MPa for the 1.4μ s duration time. Macroscopic radial cracks appear at ~ 30 MPa and complete fragmentation at ~ 40 MPa for both cases (Figure 2.6).
6. The reduction of P-wave velocity is greater than the reduction of S-wave velocity for both San Marcos gabbro (Figure 2.3) and Sesia eclogite (Figure 2.5). There is no



(a)



(b)

Figure 2.6: Velocity measurements for Coconino sandstone experiments of duration time of (a) $2.4 \mu\text{s}$ and (b) $1.4 \mu\text{s}$. Dashed lines indicate the same as those in Figure 2.5.

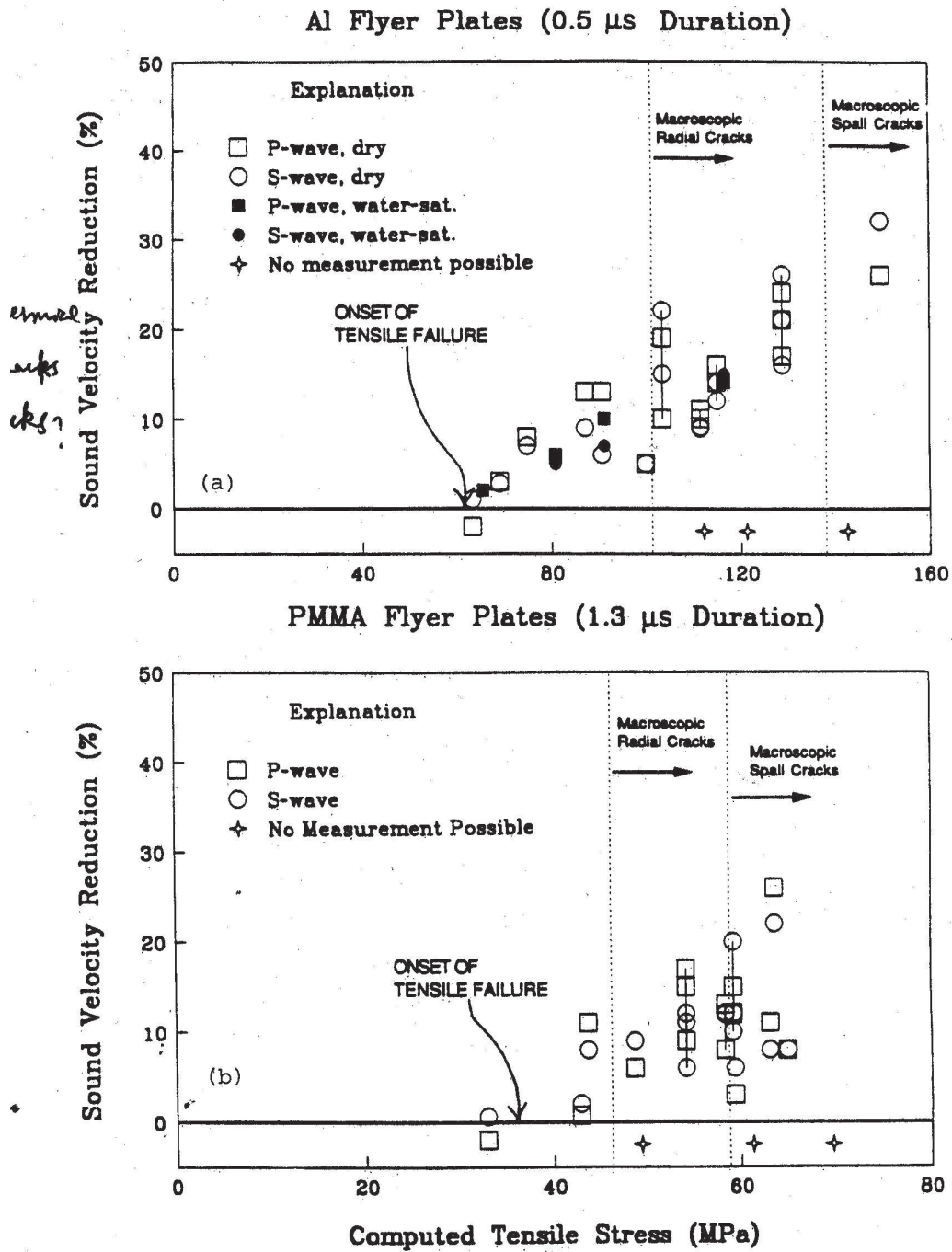


Figure 2.7: Velocity measurements for Bedford limestone. (a) 0.5 μ s and (b) 1.3 μ s. (From Ahrens and Rubin [1993], Fig. 2.)

obvious relation between P- and S-wave reduction for Coconino sandstone.

7. All pre-shot and post-shot V_p/V_s values of the three types of rocks are shown in Figure 2.8. V_p/V_s for pre-shot San Marcos gabbro is 1.9 ± 0.05 . For pre-shot Sesia eclogite, V_p/V_s is 1.7 ± 0.13 , compatible with the value of Healdsburg Eclogite, California (1.74) [Birch, 1960] and that of Sunnmoure Eclogite, Norway (1.66) [McQueen et al., 1967]. For Coconino sandstone, it is 1.5 ± 0.08 . The measurable post-shot V_p/V_s value for both San Marcos gabbro and Sesia eclogite is less than the pre-shot value (Figure 2.8a, b). The post-shot values of both types of rocks decrease with tensile stress and the difference between pre- and post-shot measurements of V_p/V_s increases with tensile stress. No obvious decrease with computed tensile stress of post-shot V_p/V_s for Coconino sandstone is observed.

For comparison, the velocity measurements for Bedford limestone at two different duration time are shown Figure 2.7. The tensile strength at $0.5 \mu\text{s}$ duration is ~ 60 MPa, and ~ 35 MPa for $1.3 \mu\text{s}$ duration.

2.4.1 Reduction of velocity by cracks

The presence of cracks within a rock has long been recognized to decrease the elastic moduli [Birch, 1960]. O'Connell and Budiansky [1974] developed a theory to calculate the effective bulk modulus (\bar{K}), shear modulus (\bar{G}), and Poisson ratio ($\bar{\nu}$), for a body with a random distribution of cracks:

$$\frac{\bar{K}}{K} = 1 - \frac{16}{9} \left(\frac{1 - \bar{\nu}^2}{1 - 2\nu} \right) \varepsilon \quad (2.4)$$

$$\frac{\bar{G}}{G} = 1 - \frac{32(1-\bar{\nu})(5-\bar{\nu})}{45(2-\bar{\nu})}\varepsilon \quad (2.5)$$

$$\bar{\nu} = \nu \left(1 - \frac{16}{9}\varepsilon \right) \quad (2.6)$$

where K is bulk modulus, G is shear modulus, ν is Poisson ratio of the undamaged body, and ε is crack density. From equations above, a crack density of 0.05 would produce $\sim 4\%$ P-wave reduction and $\sim 1.5\%$ S-wave reduction.

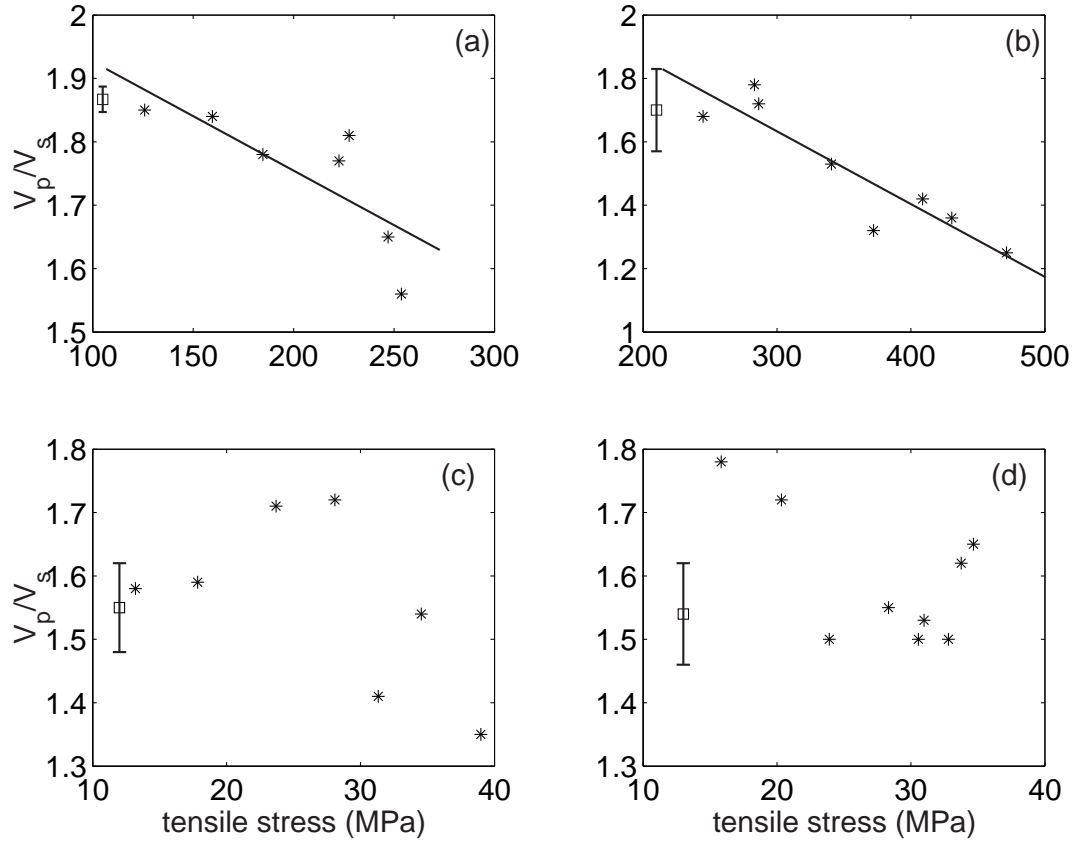


Figure 2.8: Post-shot V_p/V_s values versus computed tensile stress: a) San Marcos gabbro (SMG); b) Sesia eclogite (SE); c) Coconino sandstone (CE) with 2.4 μs duration time; d) sandstone with 1.4 μs duration time. Open squares are average pre-shot V_p/V_s : 1.87 for SMG, 1.7 for SE, and 1.54 for CS. Error bars represent lower and upper limits of pre-shot V_p/V_s value. Stars are post-shot V_p/V_s values. Straight lines in (a) and (b) are linear fit of post-shot results for SMG and SE. Post-shot V_p/V_s decreases with computed tensile stress for both cases. Post-shot V_p/V_s values of CS for two duration time cases are scattered. No obvious relation between post-shot V_p/V_s and tensile stress observed for CS.

For a cracked body, reduction of both P- and S-wave velocities increase with crack density. This is consistent with our experimental results for all the four types of rocks (Figure 2.3 to 2.6). However, the degree of velocity decrease depends on the orientation of cracks. According to theory of *O'Connell and Budiansky* [1974], reduction of S-wave velocity is only slightly less than that of P-wave velocity for dry rock samples with randomly oriented cracks. For example, a 20% reduction in P-wave velocity should be associated with 18% reduction in S-wave velocity. If the cracks had a preferential orientation, they would reduce the P-wave velocity measured in the direction perpendicular to the crack orientation surface much more than the S-wave velocity measured in the same direction. This result has been demonstrated both theoretically [*Anderson et al.*, 1974; *Nishizawa*, 1982] and experimentally [*King*, 2002]. According to the calculation of *Anderson et al.* [1974], for reasonable crack aspect ratios (0.05), a 20% reduction in P-wave velocity is associated only with ~ 5 to $\sim 7\%$ reduction in S-wave velocity.

Interaction of release waves emanating from lateral boundaries and planar-impacted surfaces induce both radial and spall cracks in our experiments. Radial cracks are also observed in similar experiments for Bedford limestone by *Ahrens and Rubin* [1993]. These are generated in non-planar deformation of the sample. We believe a major contribution to the loss of one-dimensional symmetry is rarefaction waves reflected from the edges of the sample. These waves propagate into the region of interest producing tensile stresses that are perpendicular to the direction of the impact. Therefore, the strain state inside the sample is not strictly uniaxial. Both radial and face-parallel cracks are expected to contribute to the wave velocity reduction. For San Marcos gabbro and Sesia eclogite, reduction in P-wave is

greater than that of S-wave velocity, indicating that the major contribution comes from the face-parallel cracks. No obvious pattern was observed for Coconino sandstone.

Although we can determine the elastic wave velocity from a given crack distribution, the converse is not true. It is impossible to determine the exact crack distribution in rocks just from elastic wave velocity measurements, since the distribution of cracks is not a unique function of the velocities [Nur, 1971]. Further experiments are under way to study the different contributions to velocity reductions of different oriented cracks.

2.4.2 Interpretation of V_p/V_s

Since shear wave velocity is less sensitive than the compressional wave velocity to the presence of cracks normal to the propagation direction of the wave [Nur, 1971; Anderson *et al.*, 1974], we can use V_p/V_s to illuminate the orientation of cracks for the three types of rocks. The average pre-shot V_p/V_s is ~ 1.9 for San Marcos gabbro (Figure 2.8a) and ~ 1.7 for Sesia eclogite (Figure 2.8b). The post-shot V_p/V_s for both types of rocks are less than the pre-shot value, indicating the cracks produced by the shock were mainly oriented parallel to the impact surfaces. The post-shot V_p/V_s for both types of rocks decrease with increasing computed tensile stress, which means higher crack density. There is no good reason for the random pattern of post-shot V_p/V_s for Coconino sandstone (Figure 2.8c, d). Further work should be conducted to study the anisotropy of sandstone.

2.4.3 Strain-rate effect

It has long been recognized in fracture mechanics that strength of material depends on the rate at which the loading is applied. Dynamic tensile strength of rocks at high strain rates produced by shock wave interactions can exceed the quasi-static tensile strength by an order of magnitude [Grady and Hollenbach, 1979]. Cohn and Ahrens [1981] came to the similar conclusion in their studies of analogues of lunar rocks. Similar behavior has been observed for ice-silicate mixtures [Lange and Ahrens, 1983]. Grady and Lipkin [1980] have generalized a wide range of data suggesting dependence of tensile fracture strength on strain rate. Grady [1998] gives the strain rate dependent criteria of tensile strength (σ_t) for ceramics:

$$\sigma_t = (6\rho^2 c^3 \dot{\varepsilon})^{1/3} \quad (2.7)$$

Where c is the compressional wave velocity, ρ is the density and $\dot{\varepsilon}$ is the strain rate, defined as:

$$\dot{\varepsilon} = \frac{\varepsilon}{\Delta t} \quad (2.8)$$

ε is strain, and Δt is the duration time. Lange and Ahrens [1983] give ε as a function of known material material parameters:

$$\varepsilon = \frac{\rho_i V_i}{\rho_i V_i + \rho_t V_t} \frac{U_p}{V_t} \quad (2.9)$$

Generally, the tensile strength is proportional to a power of the strain rate, with the power law exponent typically around 1/4 to 1/3, depending on the materials [Grady and Lipkin, 1980; Housen and Holsapple, 1990; Grady, 1998].

The porous Coconino sandstone is expected to behave differently from the ceramics. However, the assumption is still valid that the dynamic tensile strength is proportional to a power of the strain rate. Taken our experiment results of 20 MPa at 1.4 μs duration time and 17 MPa at 2.4 μs duration time, the power law exponent is calculated to be 1/3.3 for Coconino sandstone. The strain, ε , is assumed to be the same for the two duration time experiments. The power law exponent fits very well within the range of previous study, 1/4 to 1/3 [Grady and Lipkin, 1980].

Table 2.4: Tensile strengths (in MPa) of ice and rocks at different strain rates.

	Strain rate (10^6s^{-1})							σ_c^a
	10^{-6}	2×10^{-2}	1/2.4	1/1.4	1/1.3	1	1/0.5	
Coconino sandstone	-	-	17(1)	20(1)	-	-	-	-
Bedford limestone	-	-	-	-	35(2)	-	60(2)	40^b
Ice	1.6(3)	17(3)	-	-	-	-	-	40^b
San Marcos gabbro	-	-	-	-	-	150(1)	-	150^c

Sources: (1)This study; (2) Ahrens and Rubin [1993]; (3) Lange et al. [1984].

^aDynamic tensile strength at strain rate of 10^6s^{-1} .

^bExtrapolated from available data.

^cMeasured.

The tensile strengths of ice and different rocks at different strain rates are given in Table 2.4. Also included is σ_c , the tensile strength at a strain rate of 10^6s^{-1} , extrapolated from available data or measured directly. The dynamic tensile strengths of Coconino sandstone, normalized by σ_c , versus strain rate are plotted in Figure 2.9. Also included in Figure 2.9 are the dynamic tensile strength of ice and Bedford limestone data from previous work [Lange and Ahrens, 1983; Ahrens and Rubin, 1993]. Non-linear square fit for all these data by the relation of $\sigma/\sigma_c = a\dot{\varepsilon}^{\frac{1}{b}}$ gives $a = 0.03 \pm 0.02$, $b = 3.97 \pm 0.05$.

The tensile strength has a strong dependent on strain rate in the high strain rate region. Care must be taken when applying the experimental measurement of sandstone to field

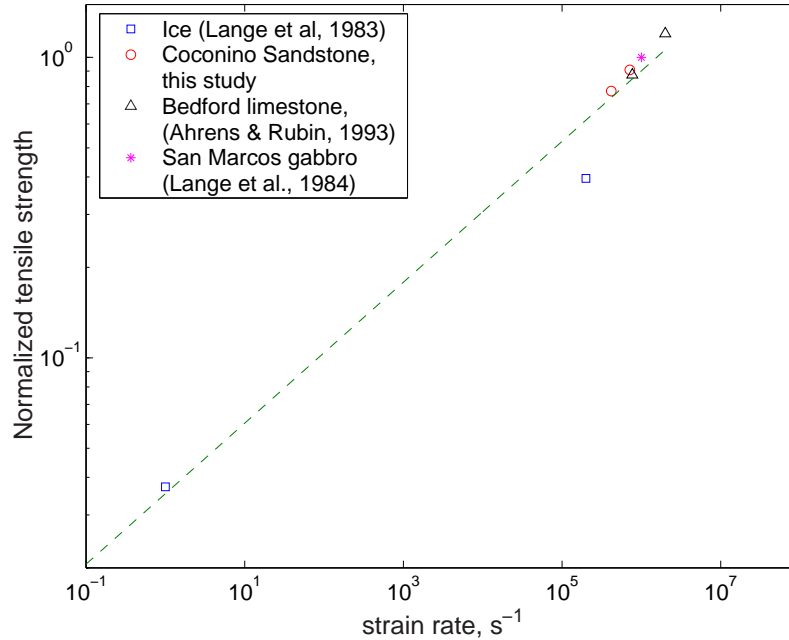


Figure 2.9: Normalized tensile strengths as a function of strain rate for ice and rocks. Dashed line is a non-linear square fit of $\sigma/\sigma_c = a\varepsilon^{1/b}$ to available data. Note log scale here. See text for detailed explanation.

impact crater, for which the strain rate is about three orders of magnitude lower, or, the duration time is about three orders of magnitude longer, than that in the experiments.

2.5 Conclusion

Four types of terrestrial rocks, San Marcos gabbro and granite, Coconino sandstone, and Sesia eclogite were subject to planar impacts to produce tensile failure under dynamic loading conditions. Two sets of experiments with different duration times were conducted for porous sandstone. Ultrasonic velocity measurements of pre-shot and post-shot samples were measured to determine the dynamic tensile strength and the fracture strength of each type of rock by detectable velocity reduction. Major results are:

1. The onset of cracking occurs at ~ 150 MPa for San Marcos gabbro, ~ 130 MPa for

San Marcos granite, ~ 20 MPa for Coconino sandstone at $1.4 \mu\text{s}$ duration, ~ 17 MPa at $2.4 \mu\text{s}$ duration, and 240 MPa for Sesia eclogite. Complete fracture occurs above 250 MPa for gabbro and granite, 40 MPa for sandstone, and ~ 480 MPa for eclogite.

2. Both reductions of P- and S-wave reduction for all the four types of rocks increase with the computed tensile stress, indicating the higher tensile pressure produced higher crack density. V_p/V_s of post-shot San Marcos gabbro and Sesia eclogite samples decrease with the computed tensile pressure. No obvious relation between post-shot V_p/V_s of Coconino sandstone and the computed tensile pressure is observed.
3. Higher reduction of P-wave than S-wave velocity in San Marcos gabbro, granite and Sesia eclogite indicates that spall (subparallel to the impact surface) cracks contribute more to the velocity reduction than radial cracks. Random pattern of reductions of P- and S-wave velocity for Coconino sandstone is possibly caused by its high porosity and variety between separate samples. V_p/V_s of post-shot San Marcos gabbro and Sesia eclogite samples are less than the pre-shot values.

Acknowledgments: We appreciate the technical support of E. Gelle, M. Long, and the advice of Professor G. Ravichandran. The paper benefited from the helpful comments of K. Housen and E. Pierazzo.

Chapter 3

Tomography Study of Shock-Induced Damage beneath Craters

3.1 Introduction

This study improved and extended the tomography method used in *Xia and Ahrens* [2001] to map the damage zones beneath impact craters using the non-destructive tomography method. First we will discuss the tomography experimental setup for mapping the velocity profile. A detailed description of the tomography method used for velocity profile inversion is given next. Using the tomography method, the P-wave structure of the center plane for the recovered San Marcos granite after impact by a lead bullet at velocity of 1200 m/s is inverted and compared with the cut-open cross-section result.

3.2 Experimental procedure

3.2.1 Cratering

Initially, 20x20x15 cm blocks were cut from San Marcos granite. The parallelism of two parallel surfaces is ± 0.5 mm, and one surface is polished to be the impact surface. All the surfaces are smooth enough to get good coupling between the transducers and target for ultrasonic measurement. The granite target is impacted by a lead bullet with diameter of 0.6 mm and mass of 3.2 g at impact velocity of ~ 1.2 km/s at normal impact angle. The impact velocity is chosen such that the damage produced in the target is moderate for the dimension of the target (i.e., neither too severe to fragment the whole target, nor too weak to produce measurable compressional velocity reduction using the tomography method).

3.2.2 Tomography technique

Figure 3.1 shows the experimental setup for the tomography measurement. To generate a strong hemispherical instead of beam-like ultrasonic wave which could penetrate the damaged low-velocity crater zone, mechanical source instead of transducer source is used. A 0.08 cm diameter stainless steel sphere, positioned on a weak tape, is launched by pre-compressed gas to produce the source wave (Figure 3.1b). The pressure of the pre-compressed gas is approximately 400 KPa for each shot. The release of the pre-compressed gas is controlled by a solenoid operated valve. The impact velocity of the ball onto the target surface is not measurable using the present technique, but the travel time of the ultrasonic wave should be dependent mostly on the media to be measured, and not on the

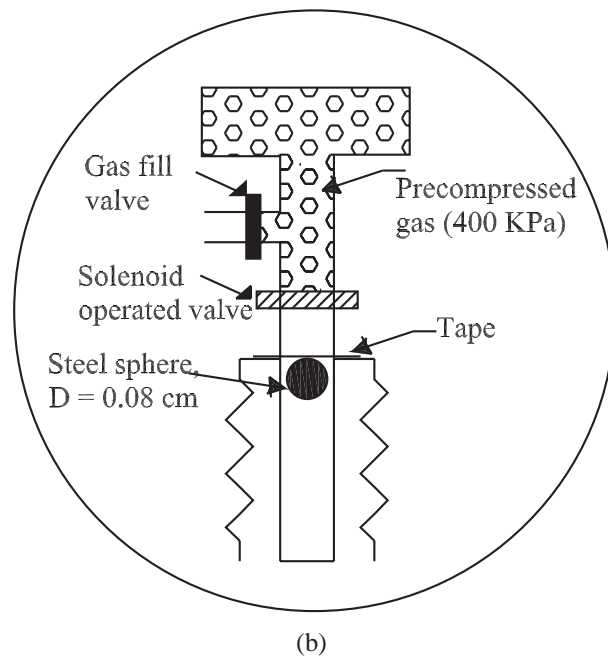
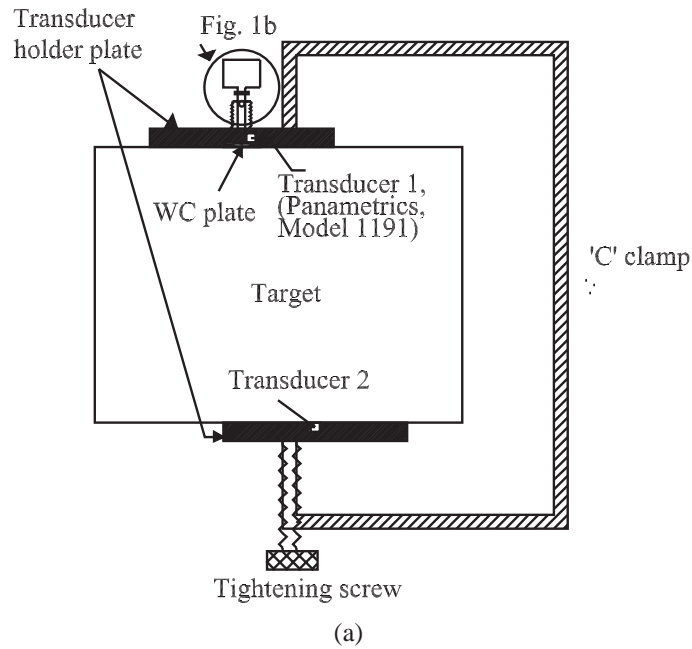


Figure 3.1: (a) Cross section of tomography measurement setup; (b) Enlarged side view of position of 0.08 cm diameter steel impactor sphere.

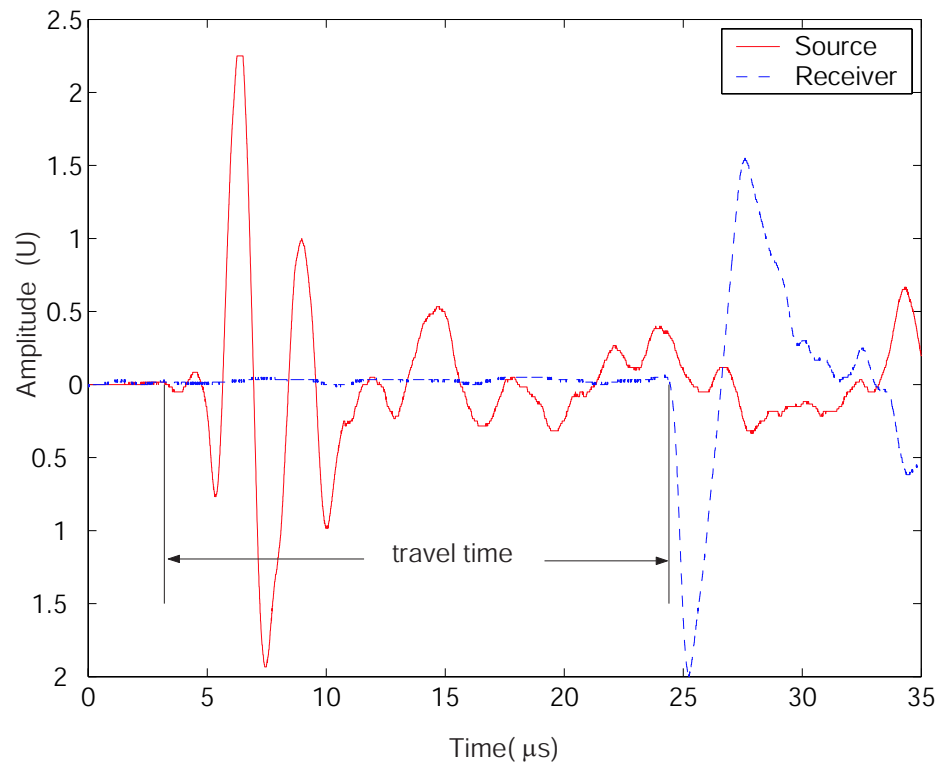


Figure 3.2: Typical ultrasonic source and receiver signal. Receiver signal is amplified 100x. Travel time is determined to be time delay between first arrivals of two signals.

impact velocity of the impactor ball. Tests show that the travel time measured in this way is quite repeatable. To prevent formation of micro-craters by the impact of the steel ball, A 0.05 cm thick tungsten carbide (WC) plate is placed on the target surface at the impact point (Figure 3.1a).

Two P-wave piezoelectric transducers (Model 1191, Panametrics, central frequency 5 MHz) are used to determine the travel time of each ray. The two transducers are positioned in the holder plates. To make good contact between the measured target surface and the transducers, the two holder plates are tightened by a tightening "C" clip (Figure 3.1a). One transducer is placed close to the impact point, with distance of 0.5 cm, to be the impact source. The error of travel time measurement caused by this is neglectable considering the dimension of the target block. A typical record is shown in Figure 3.2 and the travel time is determined by the time delay between the initial jumps of the two signals. Uncertainty in time measurement is $\pm 0.05 \mu s$.

The compressional wave velocity of the center plane (15x20 cm) of a San Marcos granite block is mapped using the tomography setup described above to check the heterogeneity of the sample. Figure 3.3 is diagram showing the sources and relative recording stations along the center plane of the pre-shot granite target assuming straight ray path for the survey. Grid used for tomography inversion is one centimeter. Cells are numbered from left to right, top to bottom. The index of the j^{th} cell of i^{th} row is therefore $20x(i-1)+j$. Index of a few cells are shown in Figure 3.3. Source and the second transducer are first placed on the two parallel surfaces (left and right, top and bottom) of the target. Then on the top side of the granite, four sources are deployed, each of which has detection stations/receivers on

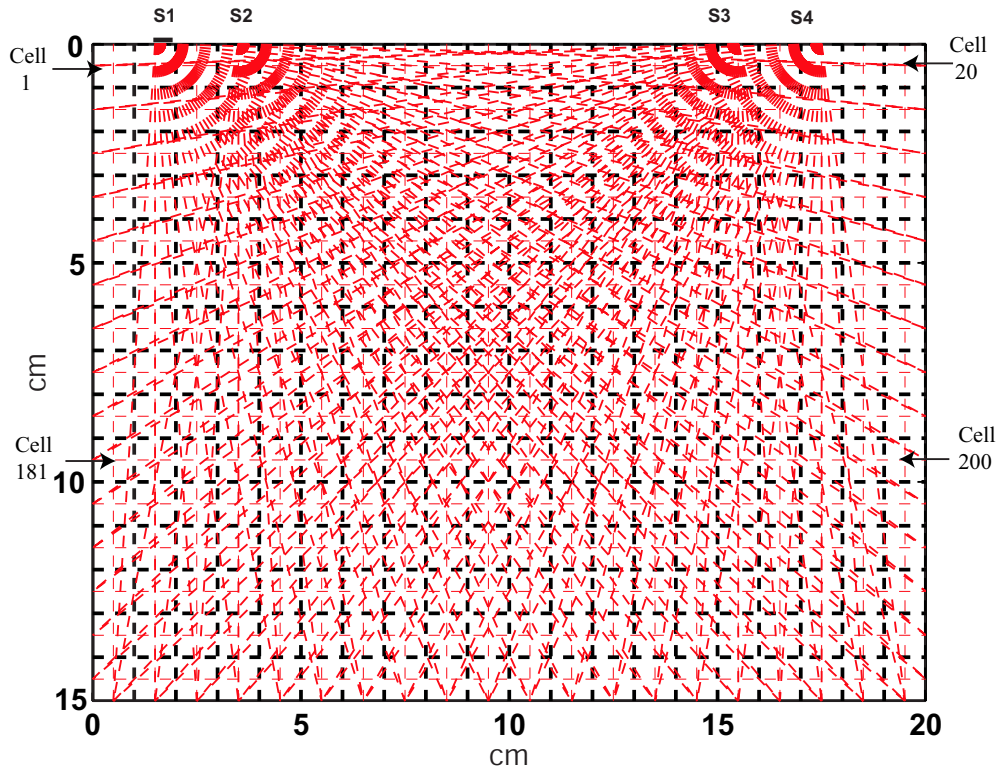


Figure 3.3: Tomographic straight ray diagram for pre-shot San Marcos granite. Thick dashed lines are cell boundaries and thin dashed lines tomographic rays. Index of cells are increased from left to right, top to bottom. For j^{th} cell in i^{th} row, index is $20 \times (i-1) + j$. Cell 1, 20, 180 and 200 are numbered. Sources placed at S1, S2, S3 and S4, and receiver stations on bottom and side surface across to fully cover target. Shot is numbered with index of source and receiver. For S1 and S2, index of receiver increases from 1 to 20 on bottom side, and 21 to 35 on side surface across. For example, shot 106 represents source S1 and receiver 6, which is sixth cell on bottom side. For S3 and S4, index of receiver starts reversely. 0.05 cm thick tungsten carbide plate is placed at impact point to prevent micro-crater formed in rock.

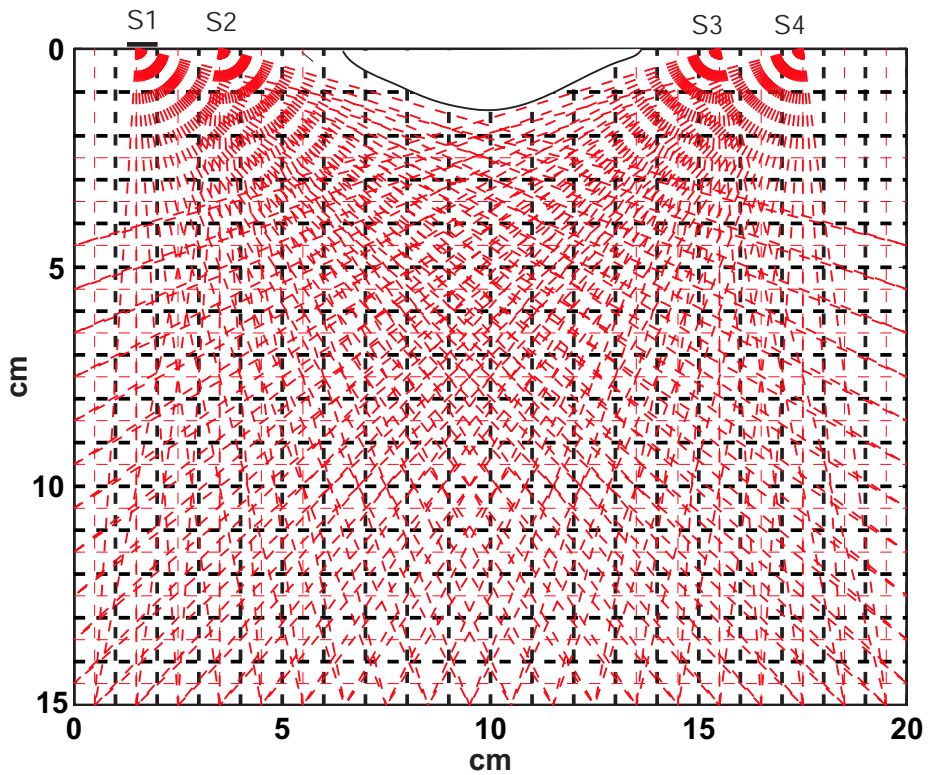


Figure 3.4: Tomographic straight ray diagram for post-shot San Marcos granite. Crater of Shot 117 shown. All other lines are same as in figure 3.3. Ray paths do not travel through crater. No axial assumption made here. Only half of rays shown here for clarity.

the bottom and the side surface across, to fully cover the center plane. The data obtained from the top sources measurement are mirrored based on the axial symmetry assumption.

The seismic survey distribution for the recovered granite target after impact is different from that of pre-shot in that the rays passing through the heavily damaged zone beneath the crater are not taken into account, since the amplitudes of these rays are attenuated greatly and no readable signal could be obtained (Figure 3.4). No assumption of axial symmetry is made for the shock-induced damage in the recovered granite target. Therefore, eight sources, instead of four, on the top surface of the rock block, are deployed to get a full coverage of the interested area. Overall, 264 (8x33) data points are obtained from these top surface sources measurements.

3.3 Results and discussion

3.3.1 Tomography inversion

Tomography means 'representation in cross-section' and is first used in medical diagnosis. Seismic tomography uses the same principles as that of x-rays, with the difference that the travel times of the signals, rather than the attenuation, are observed. Travel times from an earthquake source are inverted to obtain information about the seismic velocity structure of the earth. For our study, the compressional wave velocity of one central plane (15x20 cm in dimension) of the granite target is mapped using the tomography setup described above. The cell size is 1 cm, thus 300 cells (model parameters) are used for inversion. Assuming the plane is divided into N cells (N is 300 for this case), and there are M rays recorded from

the measurement, the travel time of i^{th} ray, t_i , is expressed as:

$$t_i = \sum_{j=1}^N u_j G_{ij}, i = 1 \text{ to } M \quad (3.1)$$

where u_j is the slowness, or reciprocal velocity, of j^{th} cell, and G_{ij} is the ray length segment of the i^{th} ray in the j^{th} cell. For the cell which is not passed by the i^{th} ray, G_{ij} equals zero. Knowing the positions of the source and receiver of each ray and assuming the ray travels in a straight way from the source to the receiver, G_{ij} could be calculated easily using the basic geometry. Equation 3.1 is to be solved to find the unknown slowness matrix, U , which is the reciprocal of the velocity matrix, V .

The source/receiver deploy allows some cells to be passed through by several rays, while some been missed entirely. For those cells passed through by more than one ray, the inversion is over-determined. It is completely under-determined for cells with no rays to pass. There may also be cells that cannot be individually resolved because every ray that passes through one cell also passes through a certain distance of some other cell. These cells are also under-determined. Therefore, the inversion for the compressional wave velocity of the center plane is a mixed-determined problem. The damped least square (DLS) method outlined in *Menke* [1989] for such problem is used to solve the slowness matrix, U ,

$$U = \left[G^T G + \varepsilon^2 I \right]^{-1} G^T D \quad (3.2)$$

where G is the ray length matrix, ε is the damping factor, chosen large enough that $G^T G + \varepsilon^2 I$ is non-singular. ε is 0.01 for our study. I is the identity matrix, and D is the measured

travel time data matrix.

The agreement between the estimated and the true model parameters is evaluated by the model resolution matrix, R , defined as:

$$R = \left[G^T G + \varepsilon^2 I \right]^{-1} G^T G \quad (3.3)$$

3.3.2 Test problems

Two test problems are carried out to validate the tomography method developed above. First, a 20x15 cm block with homogenous velocity structure, which is the simplest situation, is tested. Figure 3.5a shows the homogenous velocity structure for forward modelling. The velocity is 6.4 km/s. Synthetic travel times from sources to receivers deployed in Figure 3.3 are calculated using the high-resolution finite difference package of *Hole* [1992], originated from *Vidale* [1990], which allows calculation of the travel time field in three dimensions for a given velocity model. These synthetic travel time data are used as input into the tomography inversion, and Figure 3.5b shows the inverted velocity structure with the straight ray assumption. It is obvious that the cm-scale tomography method works very well for the structure without obvious velocity contrast.

The second test carried out is a 20x15 cm block with a low velocity zone of 5 km/s in the middle and 6.4 km/s for the rest (Figure 3.6a). The same tomography method is applied to get the inverted velocity structure, using the straight ray assumption.

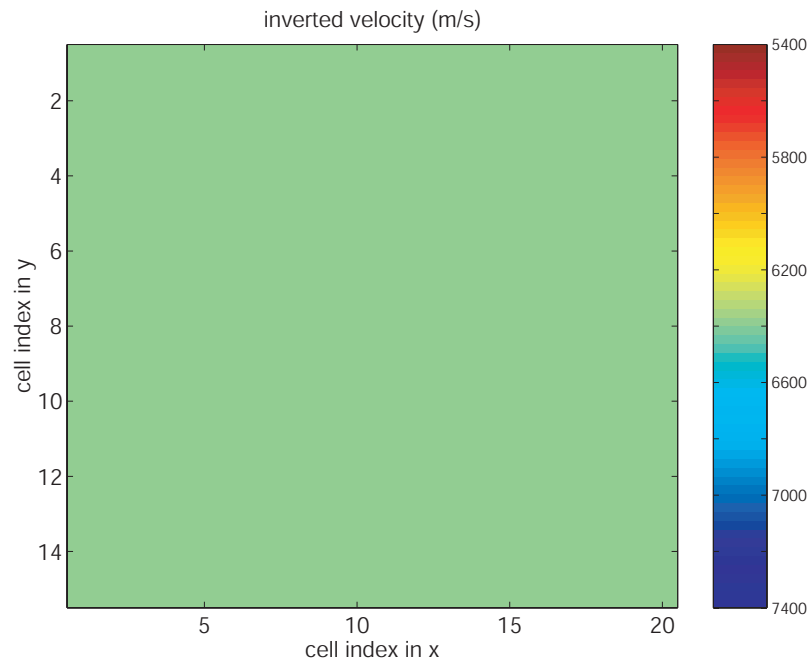
For relatively homogenous velocity structure, the straight ray path assumption is valid. However, if there are large velocity contrasts in the body to be studied, this assumption

might not be realistic and it is necessary to take into account the possibility of curve ray path. Next we will discuss how to determine the real curve ray path in a structure with velocity contrast.

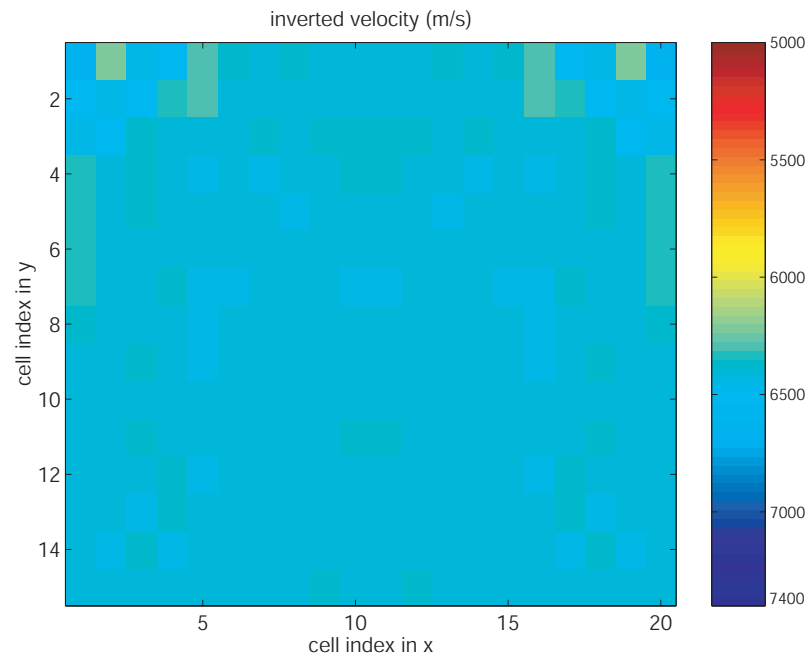
There are several possible ways for a seismic wave to travel from point A to point B within a large velocity contrast structure. Figure 3.9a shows two of these possible ways. The travel times for the two rays are t_1 and t_2 , with $t_1 > t_2$. P-wave first arrivals take a minimum travel time from the source to the receiver, the real path is ray 2 instead of ray 1 in Figure 3.9a. This is also true if the wave travels backward from point B to point A (Figure 3.9b). The signal will take the same ray path which requires the minimum travel time, t_2 . Therefore, for a wave travelling from point A to B and then propagating back, the actual ray path is the one with the minimum total travel time. Understanding this, it is straightforward now to find out the real ray path in the heterogenous block studied.

To find the real curve ray path from one source (S) to one receiver (R), the travel time from S to all the grid points is calculated using the 3-D finite differential package [Hole, 1992] and the velocity model obtained from straight ray assumption as the reference model. To improve the resolution of the forward calculation, a forward model cell size of 0.5 cm is used instead of 1 cm. Similarly, the travel time from R to all the grid points is also calculated. If we add the two travel time matrix together, the true curve ray path can be found by joining those points which have the minimum values of travel time within each column between the source and the receiver.

The other rays from all the sources to the receivers are found in the same way. The new curve ray length matrix G , where terms are the lengths of the i^{th} ray in the j^{th} cell,

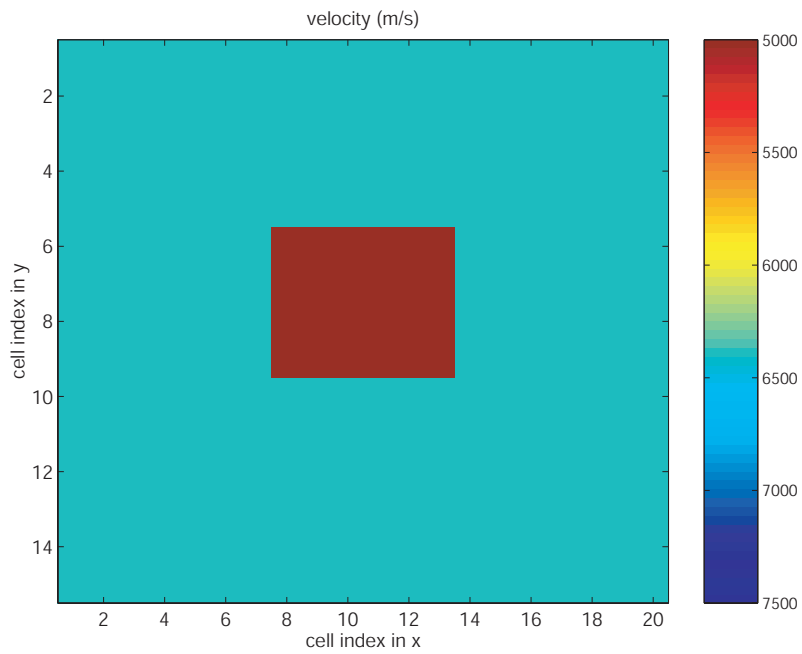


(a)

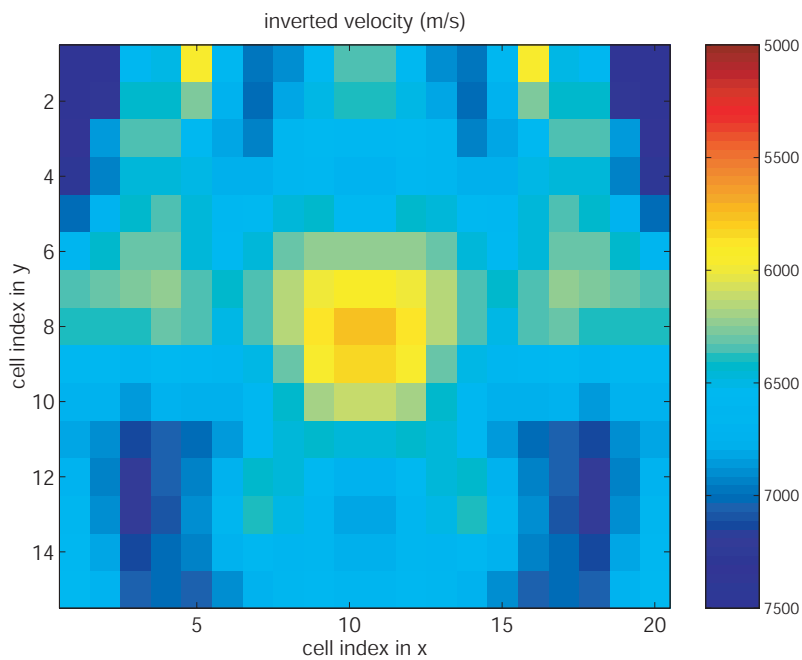


(b)

Figure 3.5: Test of the cm-scale tomography method developed above using a homogenous velocity structure. (a) Forward velocity model. Velocity of the 20x15 cm structure is 6.4 km/s; (b) Inverted velocity structure using the tomography method with straight ray assumption.



(a)



(b)

Figure 3.6: Test of the cm-scale tomography method developed above using a heterogeneous velocity structure. (a) Forward velocity model. Velocity of the 20x15 cm structure is 6.4 km/s and the low velocity zone in the center is 5.0 km/s; (b) Inverted velocity structure using the tomography method with curve ray assumption.

is obtained from the curve ray tracing procedure and substituted in Equation 3.2 to start the new iteration. Figure 3.6b shows the inverted velocity structure from the curve ray assumption.

3.3.3 Experimental results

Figure 3.7 shows the inverted compressional wave velocity profile of one center plane for the granite target before impact. The inverted pre-shot P wave velocity is 6.4 ± 0.3 km/s, close to the direct measurement. No obvious compressional velocity heterogeneity is observed from the inversion. Therefore, all the targets for study are assumed to be homogeneous in terms of the compressional velocity and no more measurements are carried out for the pre-shot target blocks.

The presence of cracks within a rock has long been recognized to decrease the elastic moduli [Birch, 1960]. The effective physical properties (effective elastic moduli here) of a cracked body depend on intrinsic elastic moduli, fluid bulk modulus K_f (air for dry situation), and crack density, ε , defined in Equation 2.3. Assuming the density of recovered rock target is constant, the elastic wave velocity would decrease with the reduced effective elastic moduli caused by presence of cracks.

The compressional wave velocity of the same center plane of the San Marcos granite after impact is mapped used the source/receiver geometry described in the previous session. The P-wave structure of the center plane for the recovered San Marcos granite assuming straight ray path is calculated and the inverted P-wave velocity profile to depth of 10 cm from the top is shown in Figure 3.8. The pattern of the shock-induced damage of the

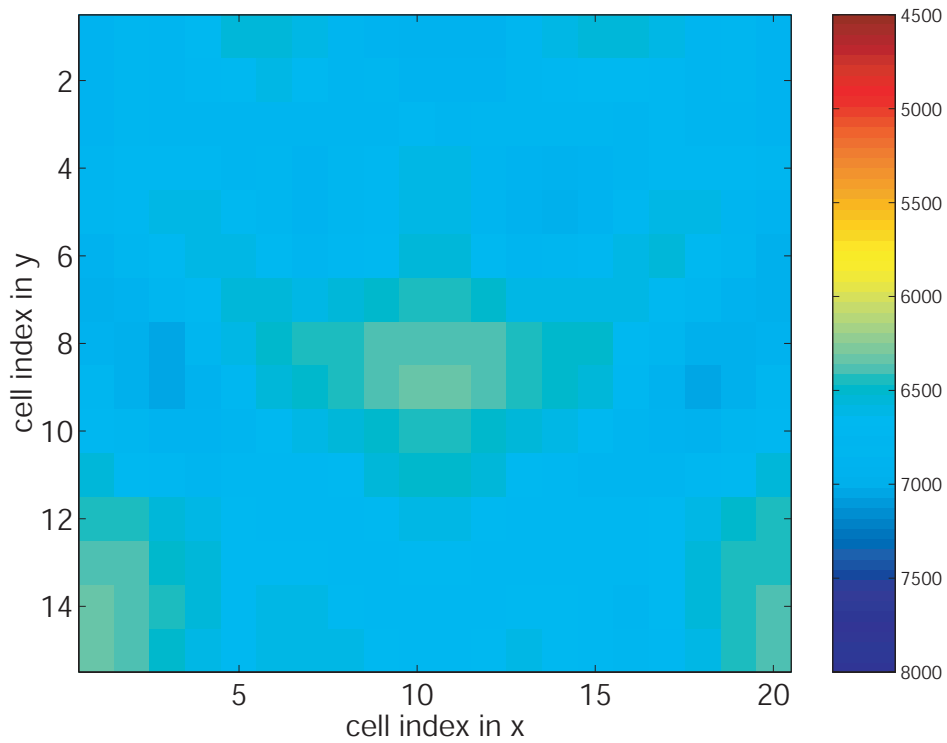


Figure 3.7: Inversion solution of compressional wave velocity structure of pre-shot San Marcos granite using straight ray deploy in Figure 3.3. A low pass filter was applied to initial inverted result to get this profile.

recovered San Marcos granite, expressed as the compressional wave low velocity zone here, is quite symmetric. This phenomenon confirms the axial symmetry assumption for vertical impact problem. The reduction of the compressional wave velocity reaches $\sim 40\%$ from the intrinsic value for the highly damaged region beneath and near the crater, 4 km/s approximately. And the velocity increases with depth until the unshocked intrinsic value is reached at depth of 7 ± 1 cm along the center line.

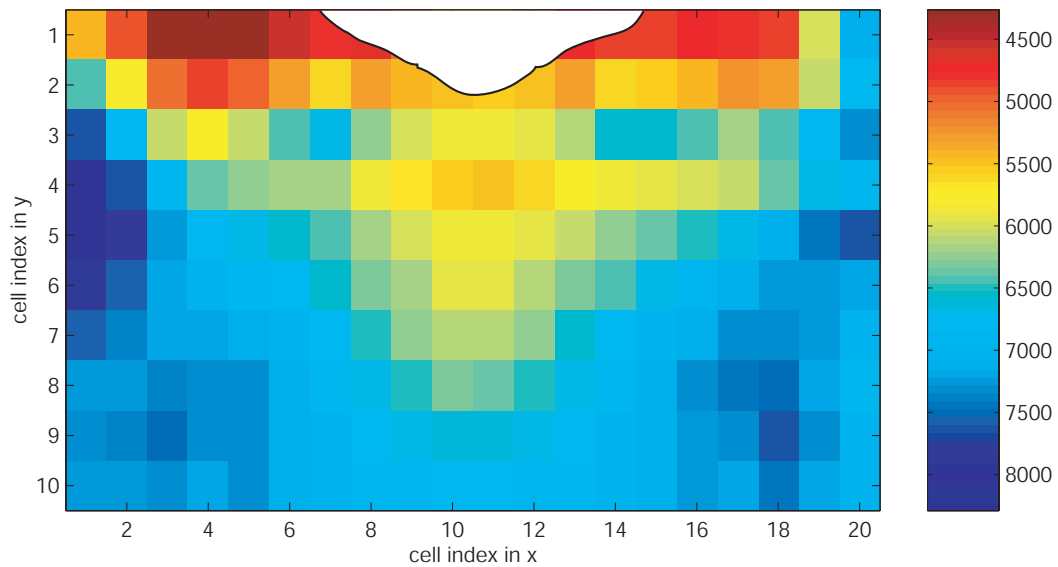


Figure 3.8: Compressional wave velocity structure of post-shot San Marcos granite of shot No. 117 from top surface to depth of 10 cm using straight ray deploy described in Figure 3.4. Same low pass filter as in Figure 3.7 was applied. Thick solid line defines crater. Low velocity zone extends to ~ 7 cm.

Figure 3.10a is the arrival travel time field from the source (S) to all the grid points in the refined forward model calculated using the 3-D finite differential package [Hole, 1992]. Similarly, Figure 3.10b is the arrival travel time field to all the grid points with source placed on the position of the receiver (R). The travel time from the source to itself is, of course, zero, and increases with the distance from the source point, as shown in these two figures. Figure 3.10c is the sum of the two travel time matrices from Figure 3.10a and 3.10b. The curve ray from the source to the receiver deflects from the straight ray path slightly (Figure 3.10c).

Figure 3.11 shows a few samples of the curve rays from the source to receivers at different positions using the velocity model inverted from straight ray path assumption. Figure 3.12a compares the travel time from experimental measurements, the calculated

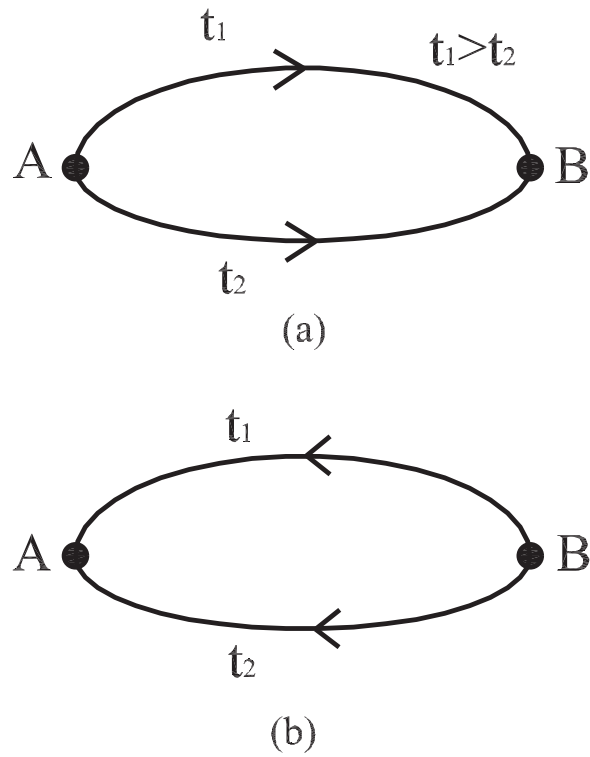
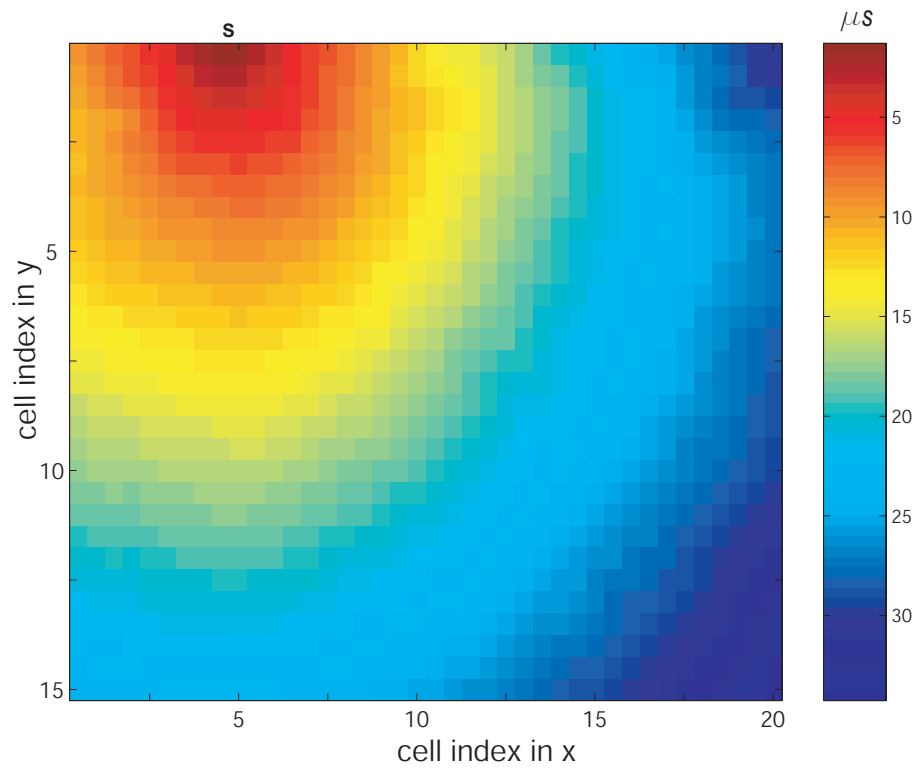
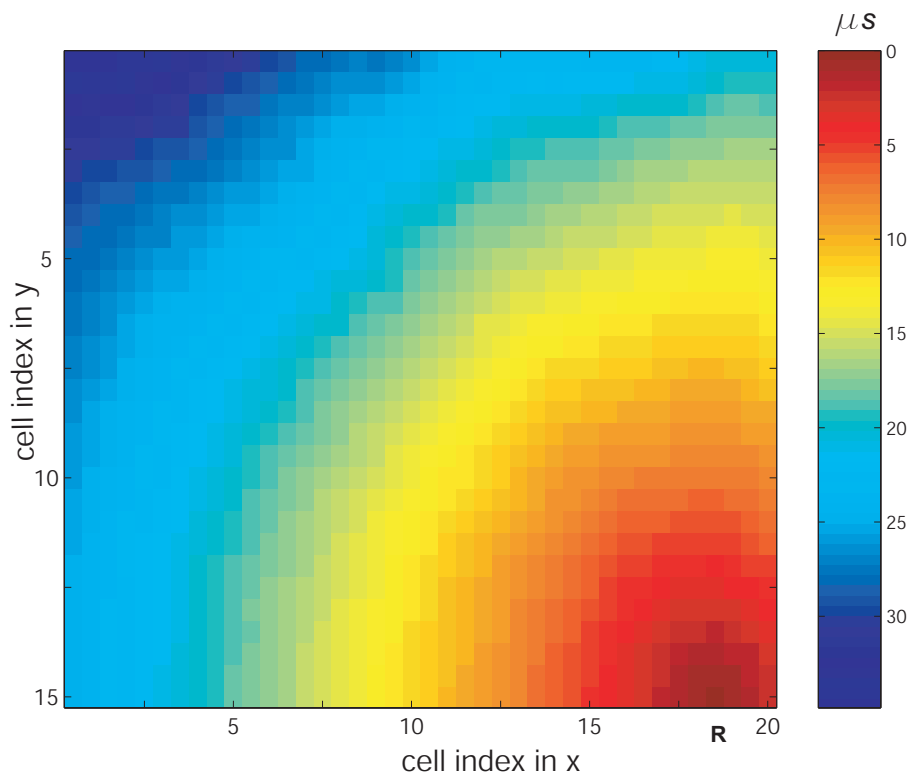


Figure 3.9: Diagram showing minimum travel time rule for a stress wave traveling between point A and point B. (a) Two possible rays with travel time t_1 and t_2 separately ($t_1 > t_2$) from A to B, actual ray path follows ray with travel time t_2 . (b) Same ray path is followed if stress wave travels from B to A in same material.



(a)



(b)

Figure 3.10: (to be continued)

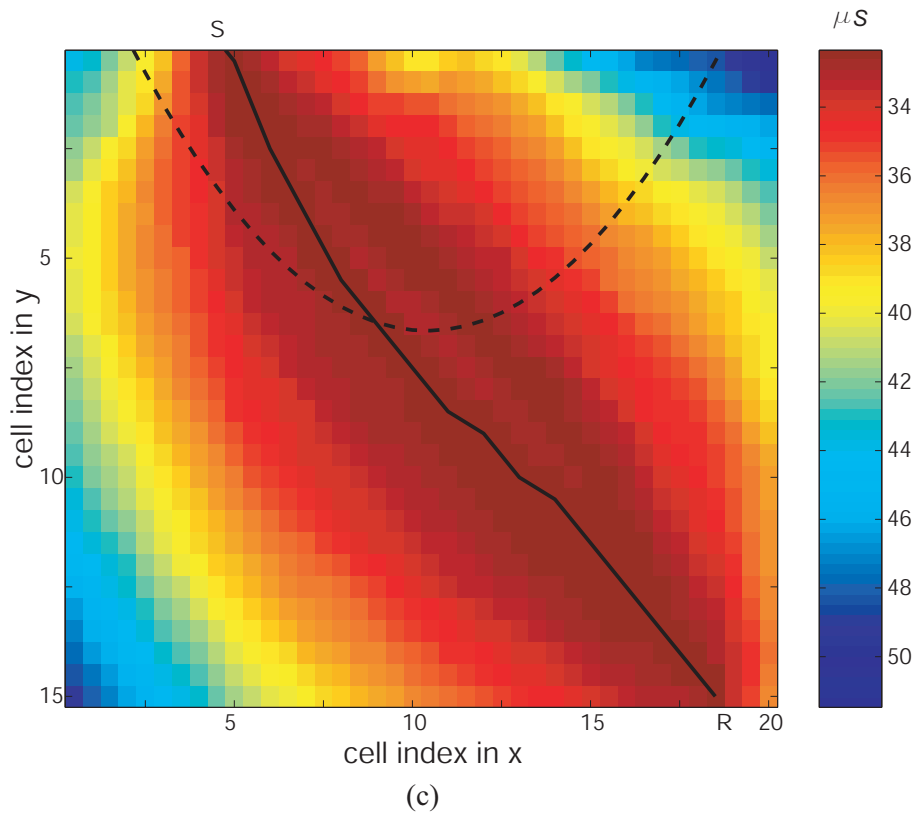


Figure 3.10: Diagram of procedure to obtain minimum time path from source (S) to receiver (R). (a) Travel time to each grid point from source, using finite difference package [Hole, 1992] and velocity model (Figure 3.8). Cell dimension used is 0.5 cm; (b) Travel time to each grid point from receiver; (c) Sum of travel times from (a) and (b). Equal to travel time for minimum time stress wave propagating from S to R, and reflected back. Minimum time path found by joining points with minimum values within S and R of travel time matrix (thick solid line). Dashed line defines approximate low velocity zone beneath crater.

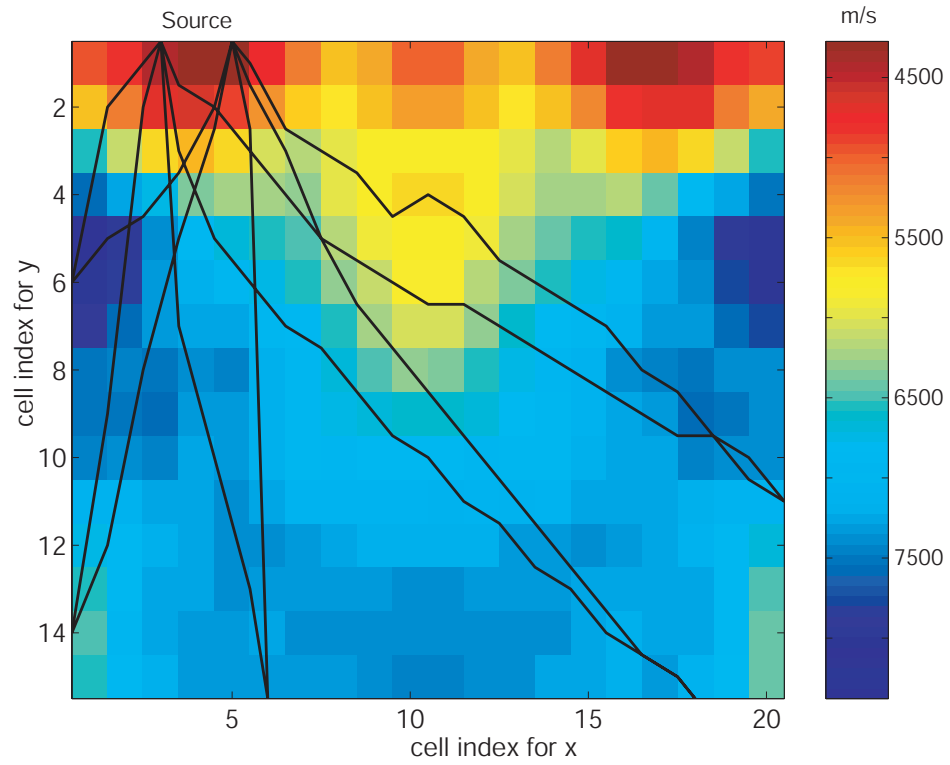


Figure 3.11: Diagram showing a few typical curve ray paths using method described in Figure 3.10 and shown velocity model.

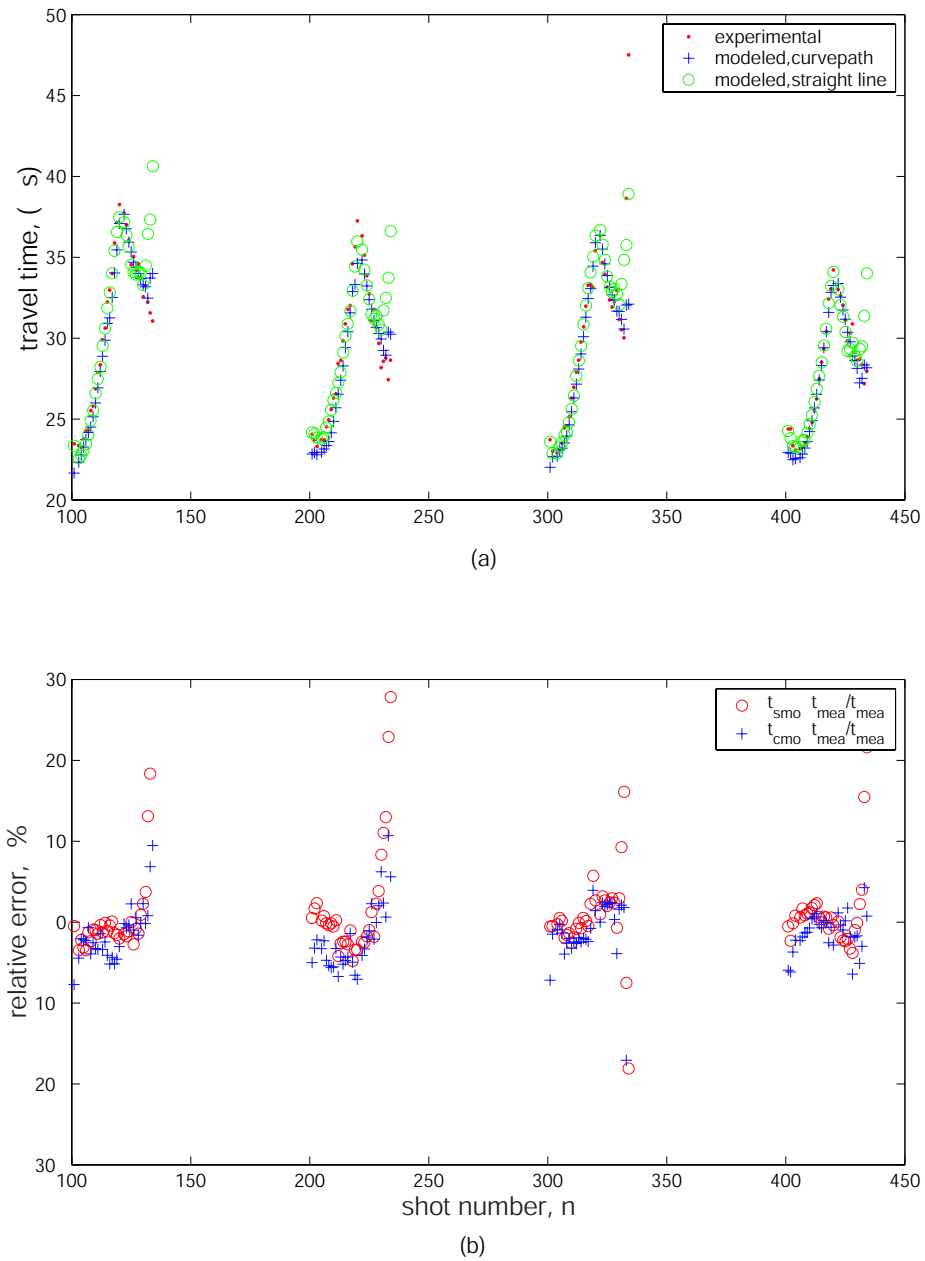
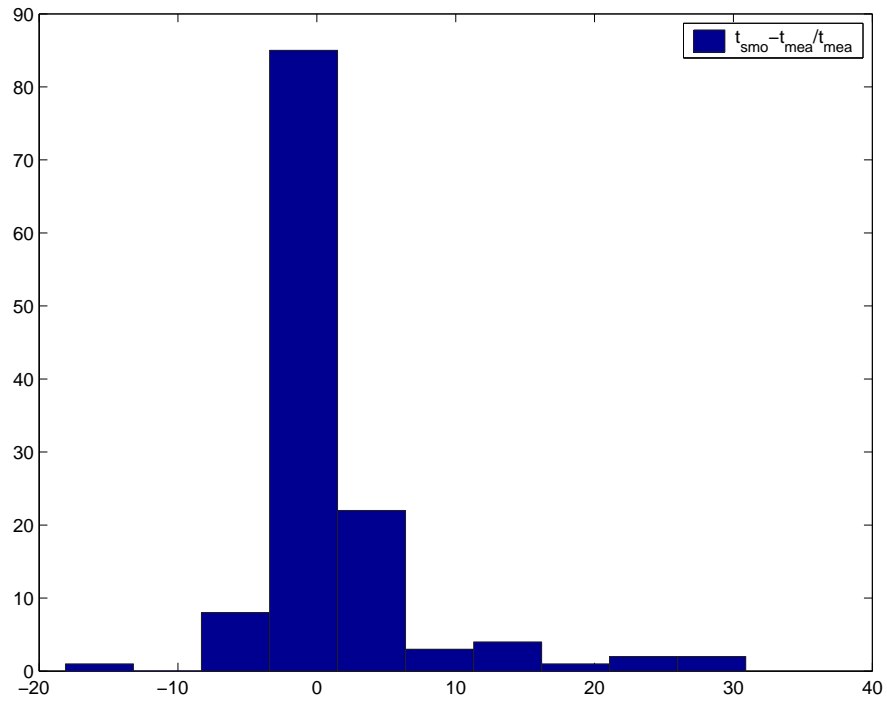
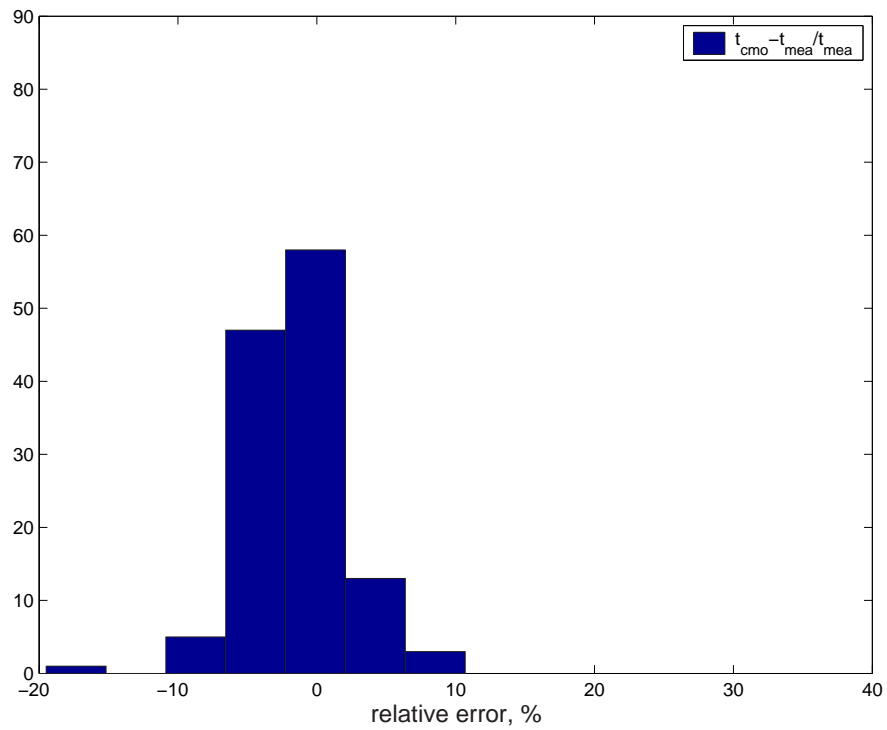


Figure 3.12: Comparison of straight ray and curve ray assumption for the second iteration. (a) Travel times from experimental measurements, and values calculated from velocity model with straight and curve ray assumption, respectively. (b) Relative offset of calculated value to measure value for both assumptions.



(a)



(b)

Figure 3.13: Histogram of relative error to measured value. (a) For straight ray assumption; (b) For curve ray assumption, second iteration.

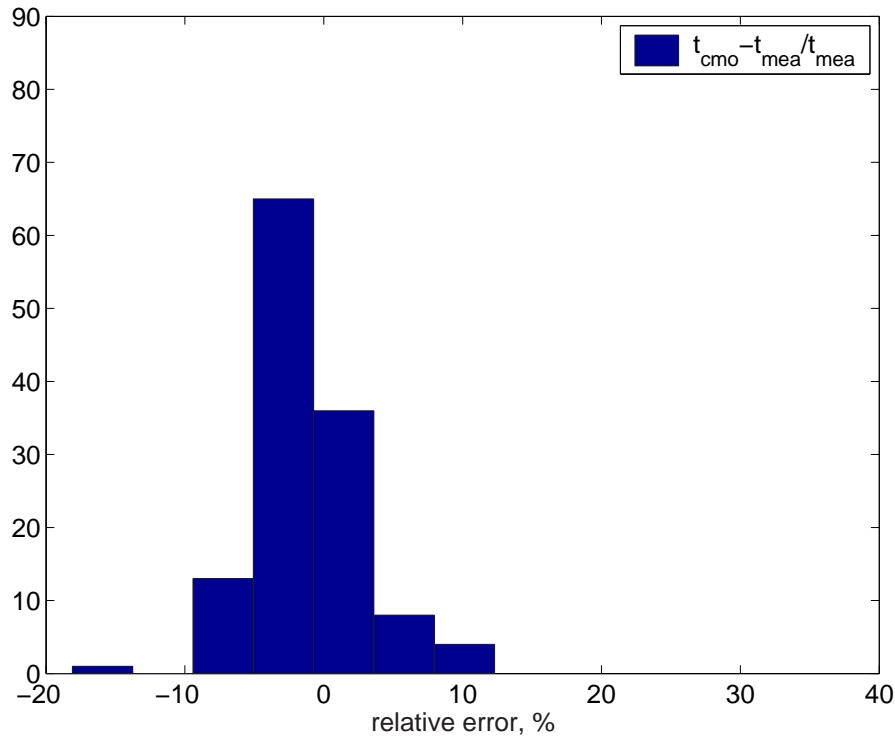
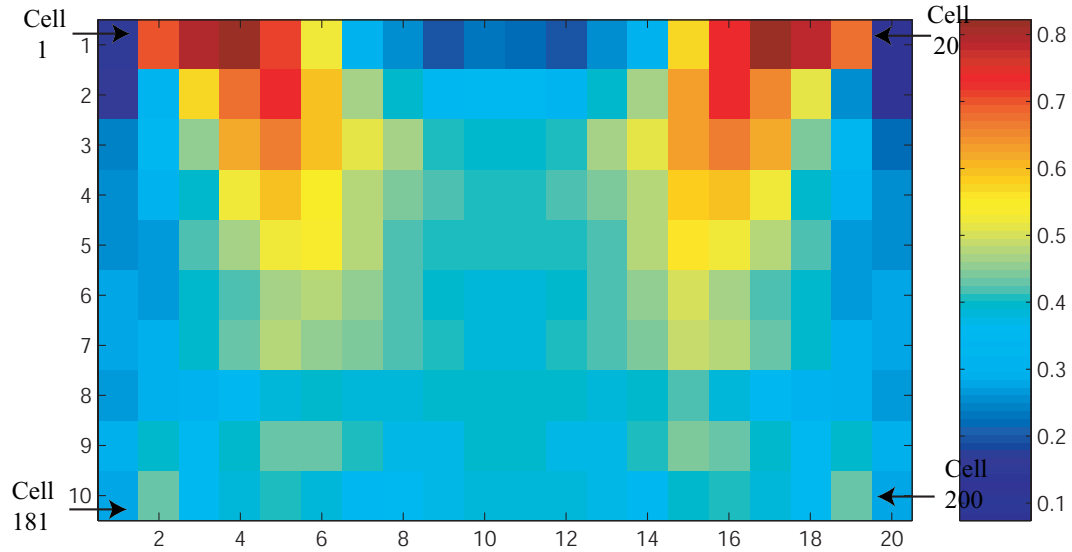


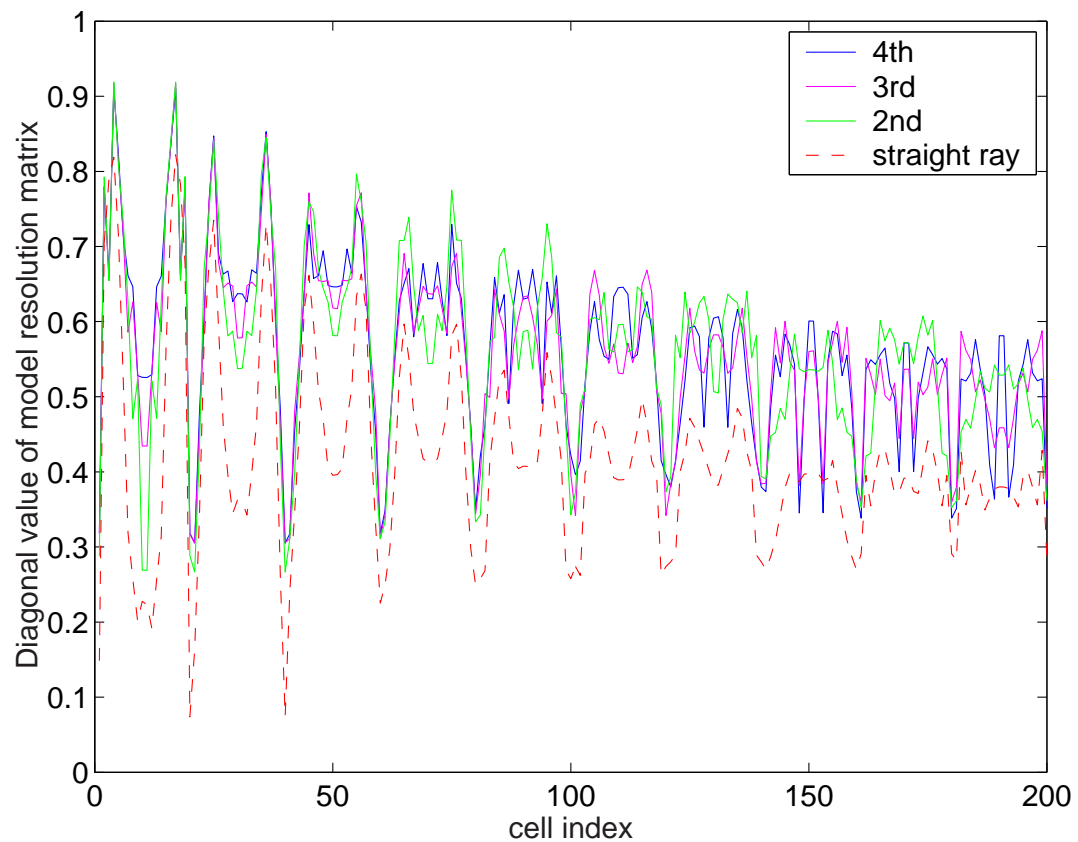
Figure 3.14: Histogram of relative error to measured value for curve ray assumption, fourth iteration.

value from straight ray assumption, as well as the value from curve ray assumption for the second iteration. For each source, the travel time of the three situations are very close except for the higher shot number, which corresponds to higher receiver index number. The calculated values with curve ray assumption agree with the experimental data better than the values with straight ray assumption do for these higher shot number. This is because receivers with higher index are those placed on the side surface across from the source (Figure 3.3). Straight ray assumption is not valid any more when rays to these receivers travel through the highly damaged region beneath the crater.

Figure 3.12b compares the relative error of the calculated values to the measured data. The error is reduced from 30% for straight ray assumption to 10% for curve ray assumption. This means the iteration with curve ray improves the inverted result greatly. This is more



(a)



(b)

Figure 3.15: (a) Matrix plot of diagonal values of model resolution matrix of 4_{th} iteration. Values for cells on the edge are very low (0.1); (b) Comparison of diagonal values of model resolution matrix for four iterations, cells 1 to 200 (See Figure 3.3 for cell index). Values for cells 1, 20, 21, 40, 41, and 60 are very low, since they are on edge of block.

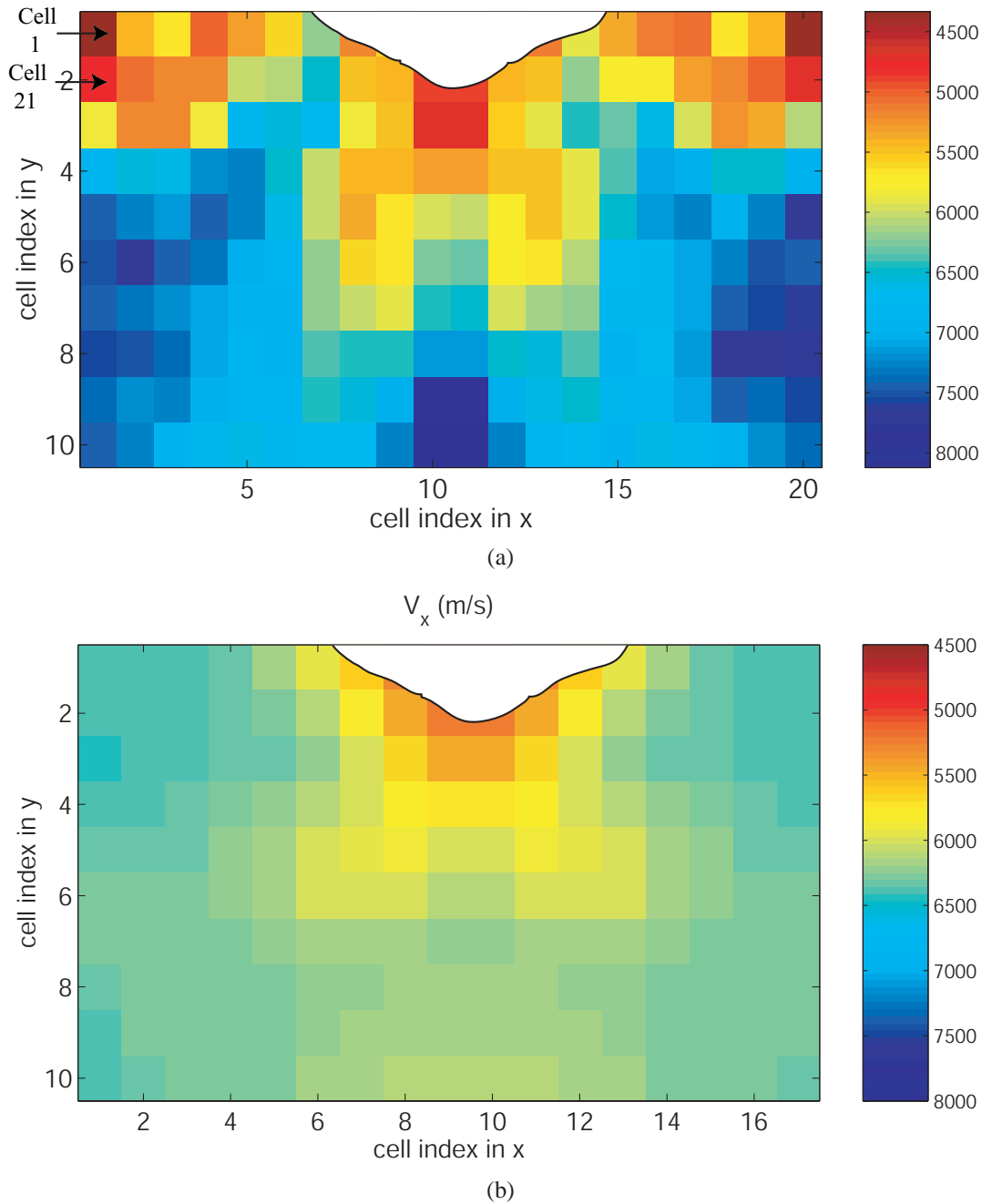


Figure 3.16: Compressional wave velocity structure of post-shot San Marcos granite of shot No. 117 from top surface to depth of 10 cm. (a) Inverted profile using curved ray paths assumption. Same low pass filter as in Figure 3.7 was applied to get this profile. Thick solid line defines crater dimension. Low velocity zone extends to ~ 7 cm. Cell index numbered in the same way as in Figure 3.3; (b) Velocity profile in X direction using dicing method (See Chapter 4 for detailed explanation.)

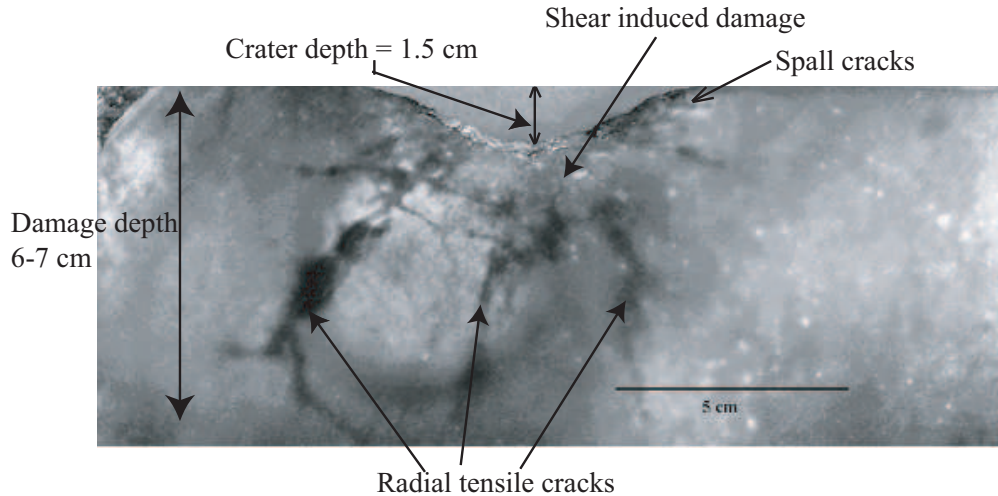


Figure 3.17: Cross section of shot 117, recovered granite impacted by 3.2 g lead bullet at 1200 m/s showing different types of cracks and damage depth. Cracks highlighted by dye coolant.

obvious from Figure 3.13, the histogram of the relative error for both straight and curve ray assumptions.

The procedure described above is continued and Figure 3.14 shows the histogram of relative error for the fourth iteration. The diagonal values of the model resolution matrix for each iteration are shown in Figure 3.15. These plots indicate that the fourth iteration has no obvious improvement over the previous one. Therefore, iteration is stopped at this point. Figure 3.16a shows the inverted compressional velocity profile from the fourth iteration. Configuration of cracks agrees better with the cross section of the recovered target (Figure 3.17) than the profile in Figure 3.8. The damage depth defined by the reduced compressional velocity is approximately 7 cm, which agrees very well with the cut open profile (Figure 3.17).

The inverted velocity profile from tomography method is also compared with that in x direction obtained from dicing method (Figure 3.16a, b; see Chapter 4 for detailed expla-

nation for the dicing method). Similarity of the pattern of low velocity zone beneath the impact crater on both profiles is observed, although the actual values of compressional wave velocity for cells are different. One reason for this disagreement is that the measurement from dicing method is carried out only in one direction, while the tomography inversion is an average value over different directions. Also this might be caused by the disadvantages of the two methods. From the test problem, we see that the tomography inversion is successful in extracting first-order heterogeneity structure, but is not very reliable in getting exact values for cells. Uncertainty exists too for the dicing method.

Figure 3.16 also shows low velocity zones in the uppermost corners (cells 1, 20, 21, 40) and the surface near the crater, which do not agree with the experimental results. One reason for the low velocity corners is probably the poor ray coverage of the uppermost cell relative to the cells with high ray coverage next to it (see Figure 3.4). The damping factor used is not high enough to minimize the solution error for this under-determined part. Values of model resolution matrix for cells near the edge are very low, only about 0.1 for these cells (Figure 3.15). The surface low velocity deficit near the crater might be caused by the limitation of the inversion method at the sources stations. We conclude that the low velocity value for the uppermost corners and the surface are caused by numerical error and should be ignored.

For this shot in our study, the initial pressure at contact, P_0 , is calculated to be 10.3 GPa, using the impedance match method [Ahrens, 1987]. The pressure in the target at distance r from the impact point, P_r , follows the relation described in Equation 1.1. The maximum depth of cracking of this shot is determined to be 7 cm from the tomographic inversion.

Taken the dynamic tensile strength of San Marcos granite as 0.13 MPa (Chapter 2), and using Equation 1.1, we found n to be 1.37, very close to the calculated value from Equation 1.2.

3.4 Concluding remarks

A centimeter scale tomography technique is developed in the laboratory in this study. This method is used to invert the shock-induced low velocity zones beneath crater in San Marcos granite impacted by a 3.2 g lead bullet at impact velocity of ~ 1.2 km/s. The main results in this study are given below:

1. The non-damage tomography method is proved to be a useful method for mapping the damage and cracking beneath impact craters in the strength regime. More experiments are needed to test the new tomography method.
2. Damage depth of this shot determined using the tomography method is $6 \sim 7$ cm. This agrees well with the analytical result of pressure calculation, as well as the examination of the cross section after the recovered target is cut open and that from the dicing method.

Acknowledgments: We appreciate the technical support of E. Gelle and M. Long. We benefit greatly from the discussion with Prof. R. Clayton and Dr. S. Ni.

Chapter 4

Effects of Shock-Induced Cracks on the Ultrasonic Velocity and Attenuation in Granite

4.1 Introduction

Damage parameter (D) and crack density (ϵ) are used to describe the intensity of fractures in the damaged body. Numerous theoretical models have been developed to relate the observed elastic velocity behavior to crack density of the cracked body. These models fall into two groups. One group of models assumes the volume concentration of inhomogeneities such as cracks, cavities or inclusions with other properties in a homogeneous matrix is small, and the interaction between these inhomogeneities can be ignored [e.g. *Anderson et al.*, 1974; *Hudson*, 1990; *Kachanov*, 1993; *Nur*, 1971]. Another group of models takes into account the interaction between the inhomogeneities when the volume concentration of inhomogeneities is large [e.g. *Berge et al.*, 1993; *O'Connell and Budiansky*, 1974].

Existence of cracks also affects the attenuation properties of the fractured body significantly. Attenuation mechanisms include friction, fluid flow and scattering, of which friction on thin cracks and grain boundaries is the dominant attenuation mechanism for

consolidated rocks [Johnston *et al.*, 1979]. At ultrasonic frequencies when the wavelength is at the same scale as heterogeneities in the rocks, scattering also plays an important role [Tompkins and Christensen, 2001].

Attenuation phenomenon has not yet received much attention among planetary cratering community because of the difficulty to carry out systematic attenuation measurements beneath impact craters in the field until recently. Liu and Ahrens [1997] did preliminary work on attenuation beneath impact craters in the laboratory. They studied shock-induced damage in a San Marcos gabbro block and related the measured attenuation with the crack density and damage in the rocks. But their work only measured the attenuation of the rocks in one direction, and did not take the orientation of the cracks and the propagation direction into account. In reality, the cracks produced by an expanding spherical shockwave within a target block include both concentric/spherical and tensile/radial cracks [Polanskey and Ahrens, 1990]. The combined effect of heterogeneity of cracks on the attenuation is of interest in this study.

In this work, the recovered San Marcos granite target after impact is cut into 1 cm cubes and compressional velocity as well as attenuation properties are measured for these cubes using ultrasonic transmission and pulse-echo methods, respectively, in three directions. Next section will discuss the experimental techniques, including the ultrasonic velocity and attenuation measurement methodology. Experimental results will be presented after, followed by analysis and discussion of the experimental data. The measured stress wave velocities will be used to calculate the damage parameter and crack density of the fractured rocks. The measured attenuation parameters are related with the crack information of the

rocks.

4.2 Experimental technique

The same recovered San Marcos granite in Chapter 3 is used here after the tomography measurement. A 1 cm thick center-plane slice was cut from the recovered target, then 1 cm aliquots are cut from the plane. We assume that no additional cracks are produced by the cutting procedures. The cube surfaces were polished until the thickness variations of any two parallel surfaces reached ± 0.005 mm. The residual water within the samples was largely removed by heating to 110° C for 24 hours within a vacuum furnace.

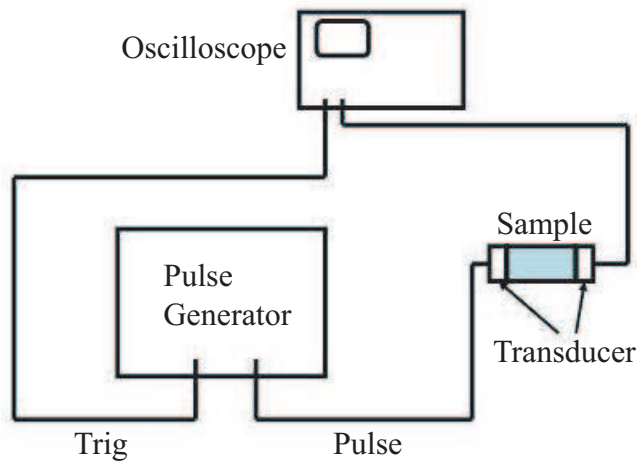


Figure 4.1: Pulse transmission ultrasonic system (modified from *Weidner* [1987]).

Pulse transmission method [*Weidner*, 1987] is used for the ultrasonic velocity measurement (Figure 4.1). The PZT P-wave transducers used are Model 1191, Panametrics, central frequency at 5 MHz. Signal is recorded with an oscilloscope (Gould 6500). Panametrics couplant D-12 is used for P-wave measurements and alcohol as the couplant remover. The

P-wave velocity of the sample is given as:

$$V_p = L/t_{sample} \quad (4.1a)$$

$$t_{sample} = t_m - t_{ini} \quad (4.1b)$$

where L is the length of the sample, t_m is the measured travel time, and t_{ini} is the initial travel time measured without sample between the two transducers. Uncertainty of the travel time measurement is $\pm 0.02 \mu\text{s}$. The calculated velocity has an error of 2 percent as estimated by the accuracy of the travel-time and length measurements.

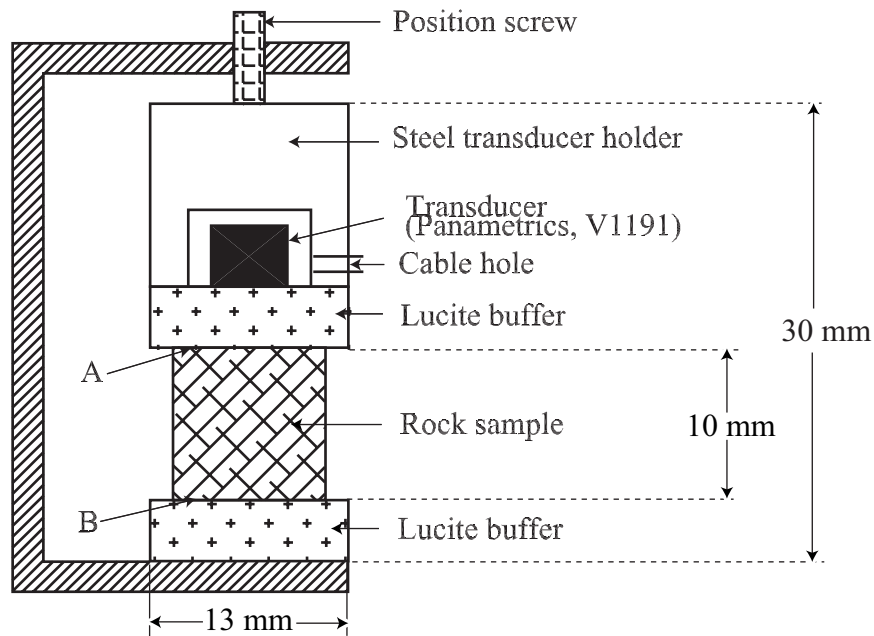


Figure 4.2: Sketch of attenuation measurement system (modified from *Winkler and Plona* [1982]).

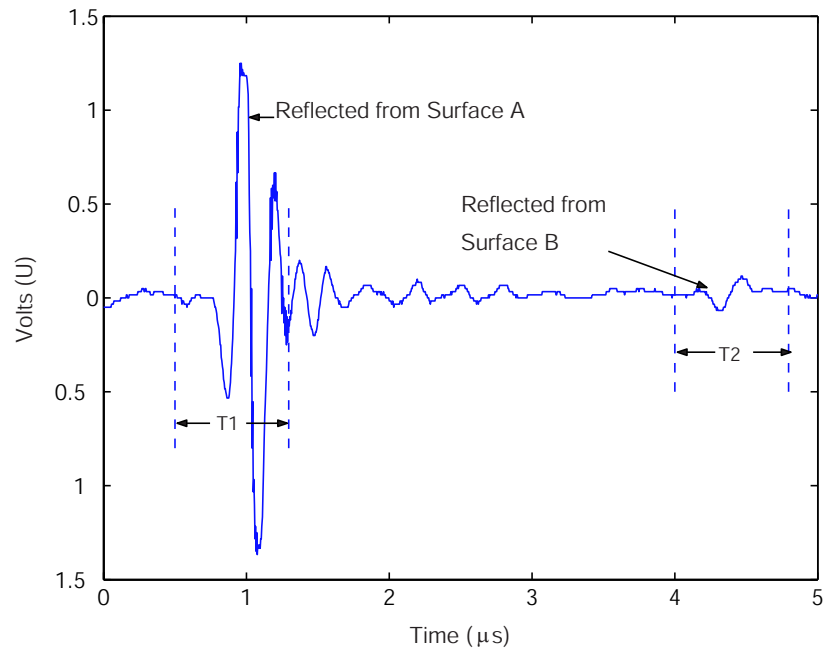
The pulse-echo technique described by *Winkler and Plona* [1982] is used to measure the attenuation coefficient. The transducer/sample assembly is shown schematically in Figure 4.8. The compressional wave transducer (Panametrics, Model V1191, central frequency 5

MHz) is placed inside a steel case so as to transmit the surrounding stress. A Panametrics 5052 UA pulser/receiver is used as the transducer's driver. Two Lucite buffers are used for coupling with the sample. The Lucite buffer plates are 1.3 cm in diameter, 0.6 cm in thickness for weak attenuation samples and 0.44 cm in thickness for stronger attenuation samples. The thickness of the buffer plates is chosen to avoid overlapping of the reflected waves from different surfaces. Panametrics D-12 couplant is put between all the contact surfaces. A constant uniaxial stress load is applied through the position screw to the system to make sure the good contact between the transducer/buffer and the buffer/sample surfaces. Stress waves reflected from surface A propagate in the first buffer plate only; waves reflected from surface B propagate through both the first buffer plate and the sample. The ultrasonic signals are recorded using a digital oscilloscope (Gould 6500). The signal was sampled at a period of 4 ns, and the amplitude resolution was 8 bits. Figure 4.3a and 4.3b are two typical signals showing the two reflected waves from surface A and B for the 0.6 cm and 0.44 cm thickness buffers respectively. For the thin buffer, the first multiple from surface A is observed before the reflected wave from surface B (Figure 4.3b). Also shown in Figure 4.3a and 4.3b are the time windows for fast Fourier transform (FFT), $\sim 1 \mu\text{s}$, or 250 data points for surface A reflection, and $\sim 0.7 \mu\text{s}$, or 170 data points, for surface B reflection. Figure 4.4 shows the typical calculated relative spectral amplitudes.

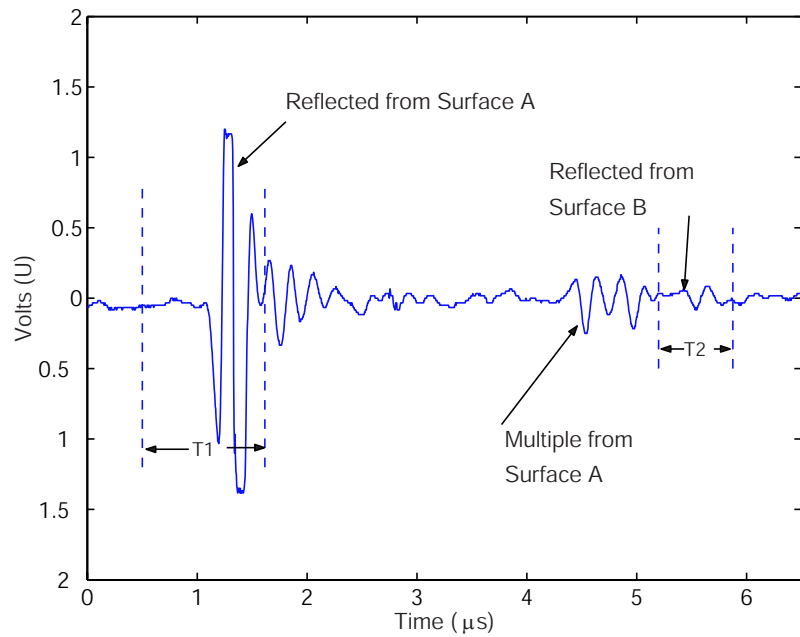
For a plane wave propagating in a medium, the amplitude of stress is given by:

$$A(x, t) = A_0 e^{-\alpha x} e^{i(kx - \omega t)} \quad (4.2)$$

where x is propagation distance, ω is angular frequency, k is wave number, and t is time.



(a)



(b)

Figure 4.3: Typical ultrasonic record for attenuation measurements and spectral amplitude of signals. (a) For 0.6 cm thick buffer. Reflected wave from surface A and B are marked separately. T1 and T2 are time windows used for FFT analysis; (b) for 0.44 cm thick buffer. Multiple reflection from surface A is arrived before the first reflected wave from surface B.

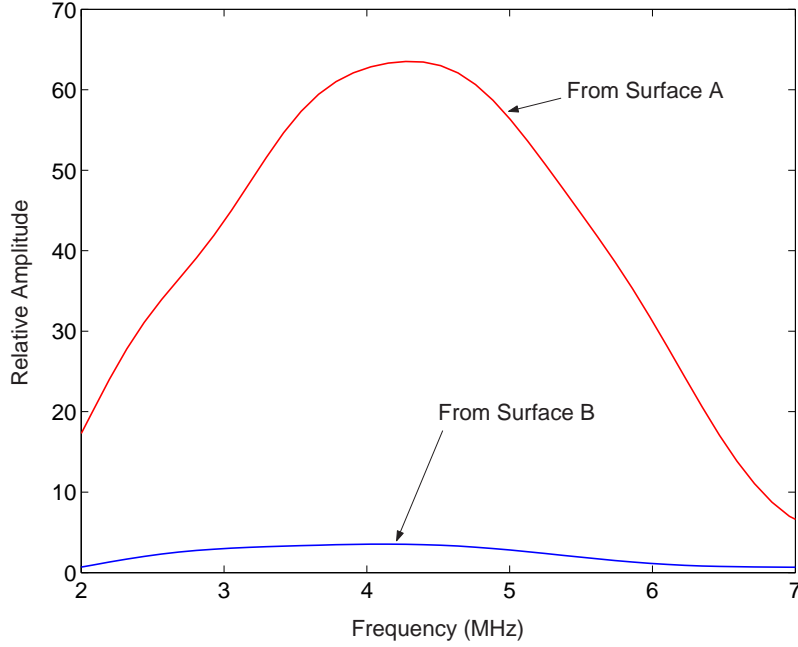


Figure 4.4: Calculated relative spectral amplitude of signals. Peak amplitude for surface A happens at frequency ~ 4.5 MHz.

The term of $A_0 e^{-\alpha x}$ represents the attenuation of the amplitude and α is the attenuation coefficient. A possible correction of attenuation due to wave spreading was not considered.

According to *Winkler and Plona* [1982], α is calculated in this way:

$$\alpha(f) = \frac{8.686}{2L} \ln \left[\frac{A(f)}{B(f)} (1 - R^2) \right] \quad (4.3)$$

where L is the sample length, $A(f)$ and $B(f)$ are the frequency-dependent amplitudes of the pulse reflected from surfaces A and B of the sample, respectively. R is the reflection coefficient for the interface between the coupling buffer and sample, defined as:

$$R = \frac{C_p \rho - C_{pc} \rho_c}{C_p \rho + C_{pc} \rho_c} \quad (4.4)$$

where C_p and ρ are the P wave velocity and the density of the samples, respectively. Sub-

script c means the values for the Lucite buffers. In this study, C_{pc} is 2.68 ± 0.02 km/s and ρ_c is 1.19 g/cm³.

4.3 Experimental results

4.3.1 Compressional wave velocity measurements

The ultrasonic compressional velocity measurements for the granite cubes were measured in orthogonal directions (Table 4.1, Figure 4.5). Unlike the results for San Marcos gabbro in *Ahrens and Rubin* [1993], local seismic anisotropy associated with the major vertical fractures parallel with the specimen edge, or referred as "side spallation fractures" in *Fujiwara* [1980], is not observed. This is because the impact velocity, ± 1.2 km/s in our study, is much less than that used in *Ahrens and Rubin* [1993] for the gabbro shot. The unshocked intrinsic ultrasonic velocity value far from the crater center section is 6.4 ± 0.2 km/s for all the three directions (Figure 4.5). Beneath the center of the crater, the intrinsic velocity value is reached at depth of 6 cm in the x direction; whereas for the z direction, which is the impact direction and contains the planar radial cracks beneath the crater, the intrinsic velocity is reached at ± 4 cm. This phenomenon is more obvious in Figure 4.6. At depth of 4.5 cm in the sample, P wave velocity in x direction is consistently lower than those in z direction within the region near the crater center line. The P wave velocity approaches unshocked values at ± 5.5 cm radial distance from the center line for all the three directions.

Figure 4.7 shows the velocity measurements in all the three directions versus radial dis-

Table 4.1: Compressional wave velocity beneath impact crater in San Marcos granite, shot 117.

(a) X direction									
	Radius from Crater Center Line (x), cm								
	0.5	1.5	2.5	3.5	4.5	5.5	6.5	7.5	8.5
Depth(z), 0.5 cm	4.9	5.2	5.4	5.87	6.29	6.34	6.37	6.45	6.36
Depth(z), 1.5 cm	5.2	5.5	5.84	6.22	6.17	6.34	6.44	6.39	6.41
Depth(z), 2.5 cm	5.57	5.83	6.24	6.29	6.52	6.33	6.22	6.53	6.37
Depth(z), 3.5 cm	5.69	5.83	5.99	6.43	6.29	6.27	6.26	6.55	6.36
Depth(z), 4.5 cm	5.9	5.86	6.0	5.93	5.98	6.17	6.29	6.4	6.32
Depth(z), 5.5 cm	6.37	6.13	6.15	6.21	6.09	6.28	6.34	6.32	6.2

(b) Y direction									
	Radius from Crater Center Line (x), cm								
	0.5	1.5	2.5	3.5	4.5	5.5	6.5	7.5	8.5
Depth(z), 0.5 cm	4.9	5.1	6.0	6.39	6.38	6.31	6.39	6.43	6.23
Depth(z), 1.5 cm	5.3	5.5	6.17	5.94	6.03	6.38	6.23	6.36	6.38
Depth(z), 2.5 cm	5.46	5.98	6.15	6.31	6.5	6.37	6.24	6.29	6.55
Depth(z), 3.5 cm	5.84	5.98	6.19	6.14	6.21	6.35	6.28	6.28	6.31
Depth(z), 4.5 cm	5.95	6.18	6.1	6.12	6.19	6.26	6.23	6.33	6.42
Depth(z), 5.5 cm	6.24	6.29	6.34	6.29	6.29	6.32	6.34	6.39	6.43

(c) Z direction									
	Radius from Crater Center Line (x), cm								
	0.5	1.5	2.5	3.5	4.5	5.5	6.5	7.5	8.5
Depth(z), 0.5 cm	4.8	5.2	5.4	6.16	6.16	6.25	6.2	6.44	6.27
Depth(z), 1.5 cm	5.2	5.5	5.85	6.06	6.2	6.31	6.34	6.26	6.39
Depth(z), 2.5 cm	5.58	6.11	5.94	6.02	6.59	6.36	6.49	6.28	6.39
Depth(z), 3.5 cm	5.75	5.96	5.85	6.08	6.31	6.43	6.26	6.18	6.36
Depth(z), 4.5 cm	6.06	6.08	6.14	6.11	6.15	6.19	6.17	6.25	6.43
Depth(z), 5.5 cm	6.08	6.1	6.05	6.07	6.16	6.17	6.31	6.31	6.42

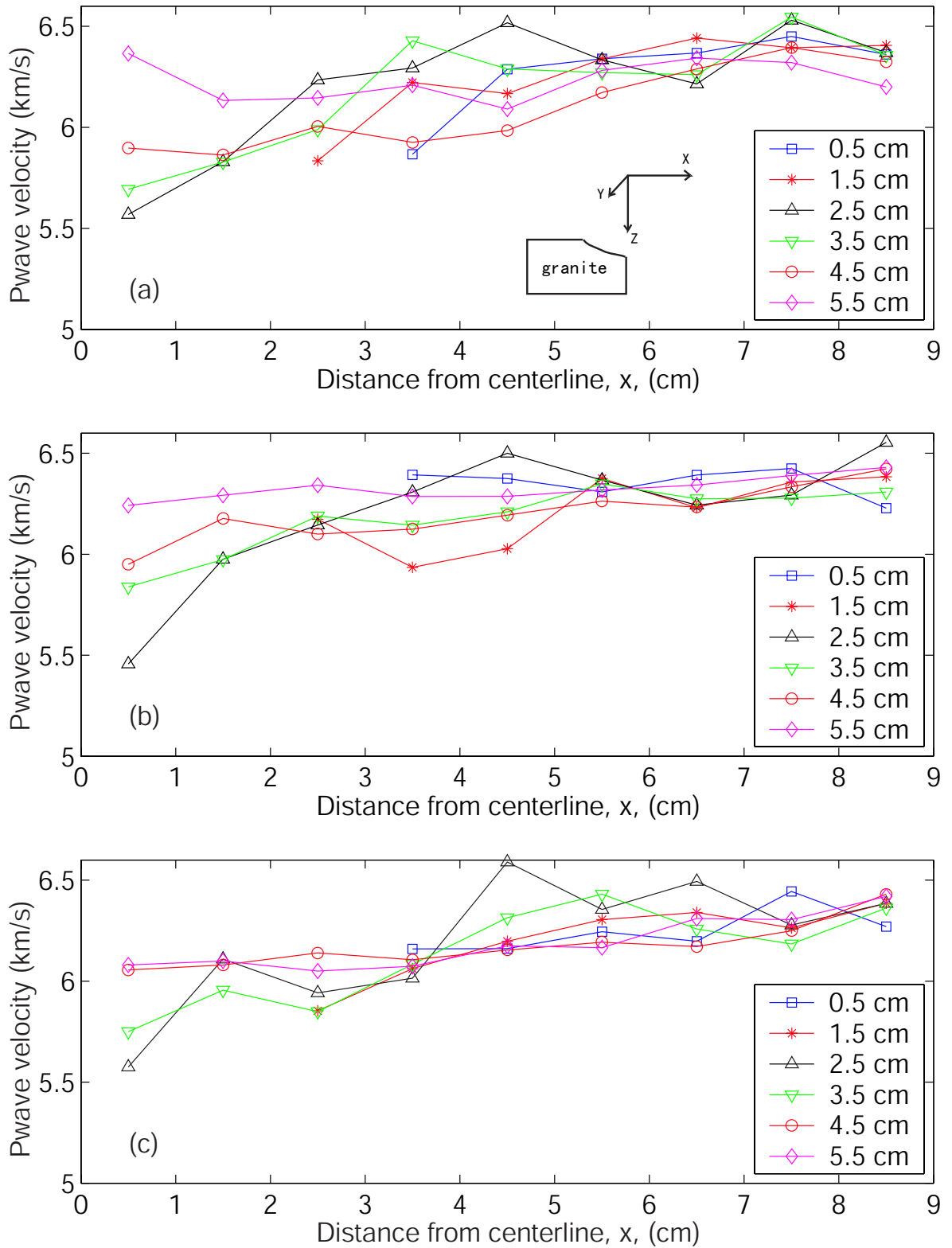


Figure 4.5: P wave velocities as a function of distance from z axis at indicated depths within sample. (a) x direction; (b) y direction; (c) z direction.

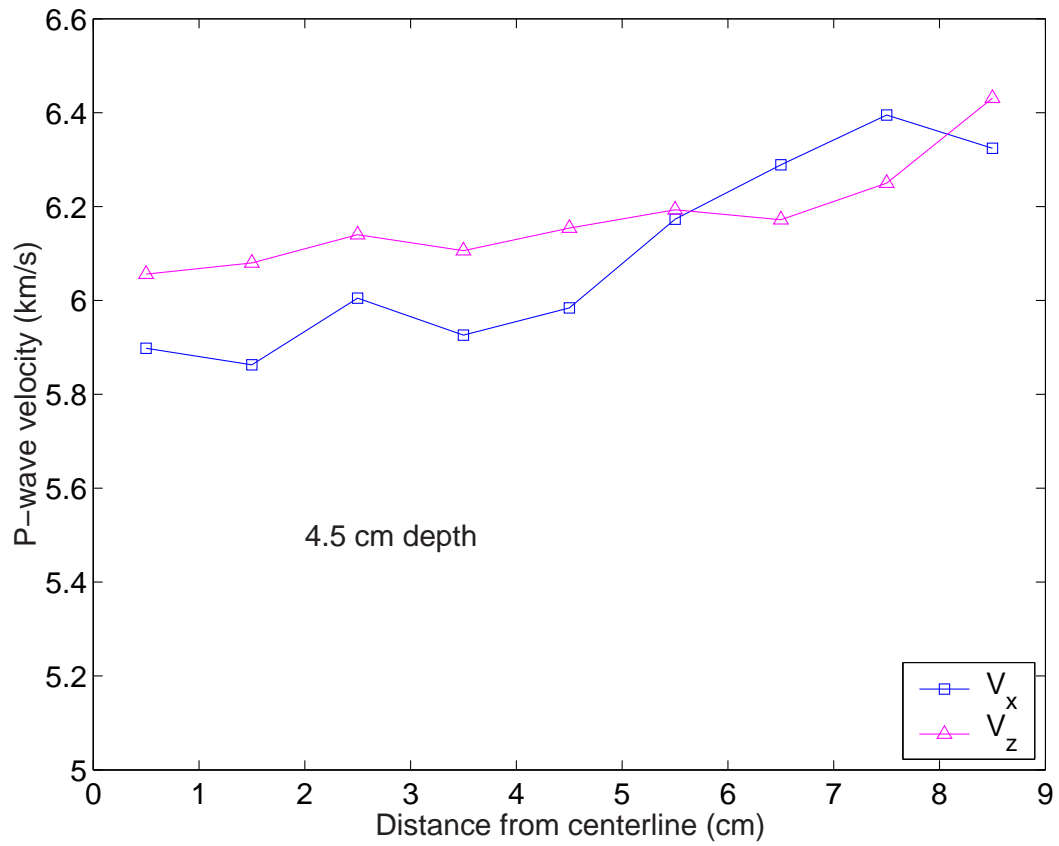


Figure 4.6: P wave velocities as a function of distance from z axis in x, y and z directions at 4.5 cm depth below surface.

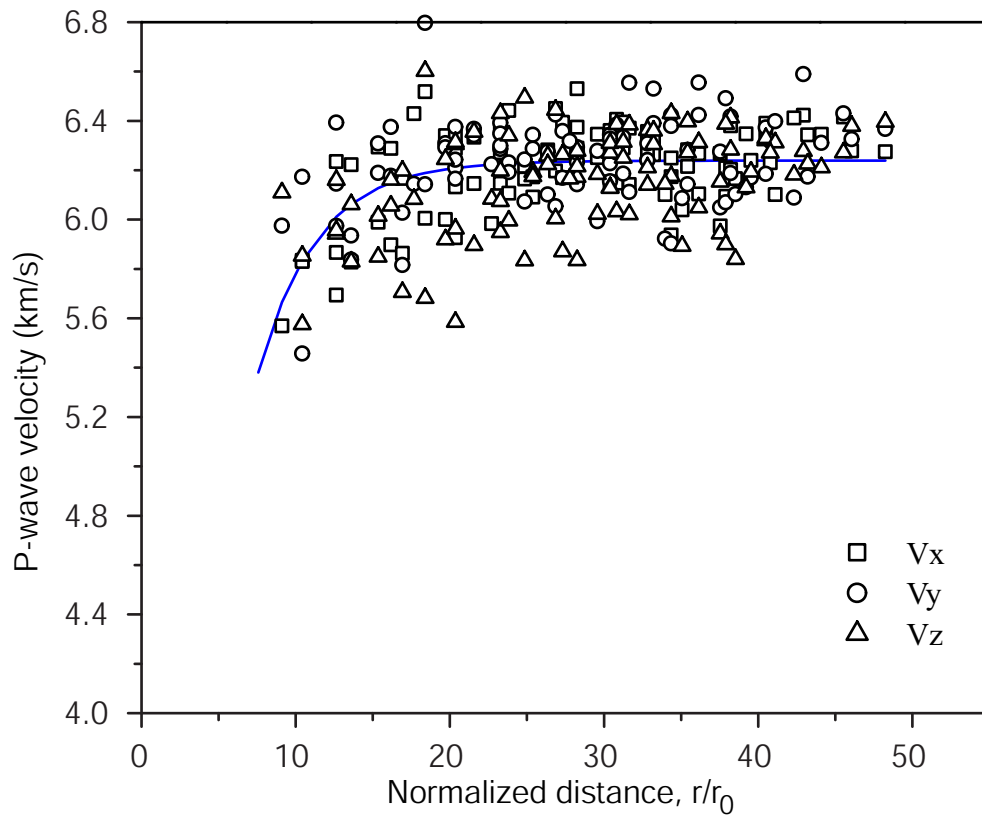


Figure 4.7: Plot of all velocity measurements in three directions as function of distance from crater center. Curve line is exponential decay fit of data. See Equation 4.5.

tance from the impact point, r ($r = \sqrt{x^2 + z^2}$). The relation between the P wave velocity and the radial distance, normalized by the radius of the projectile, 0.3 cm for this shot, is found to follow an exponential decay relation:

$$V_p = 6.24 (1 - e^{(-0.26 \pm 0.01)r/r_0}) \quad (4.5)$$

The ultrasonic P wave velocity increase to its unshocked value at r/r_0 equals 20, or, the radial distance ~ 6 cm. This is in good agreement with the observation of the limit of radial cracking that may be seen in the cross section after cutting the target open (Figure 3.17).

4.3.2 Attenuation measurements

Compressional wave attenuation coefficients are all calculated at frequency of 4.5 MHz, the central peak of reflected wave from surface A (Figure 4.4) using Equations 4.3-4.4. The accuracy of calculating α_p using this pulse-echo method is estimated to be ± 0.05 dB/cm [Wepfer and Christensen, 1990]. Figure 4.8 shows the relation between the attenuation coefficients versus the normalized radial distance from the impact point. The general trend for the three directions is that the attenuation coefficients decrease with the increasing radial distance from the impact point, following a power decay law:

$$\alpha_x = 15.17(r/r_0)^{-0.17 \pm 0.03} \quad (4.6a)$$

$$\alpha_y = 15.26(r/r_0)^{-0.17 \pm 0.03} \quad (4.6b)$$

$$\alpha_z = 12.02(r/r_0)^{-0.14 \pm 0.03} \quad (4.6c)$$

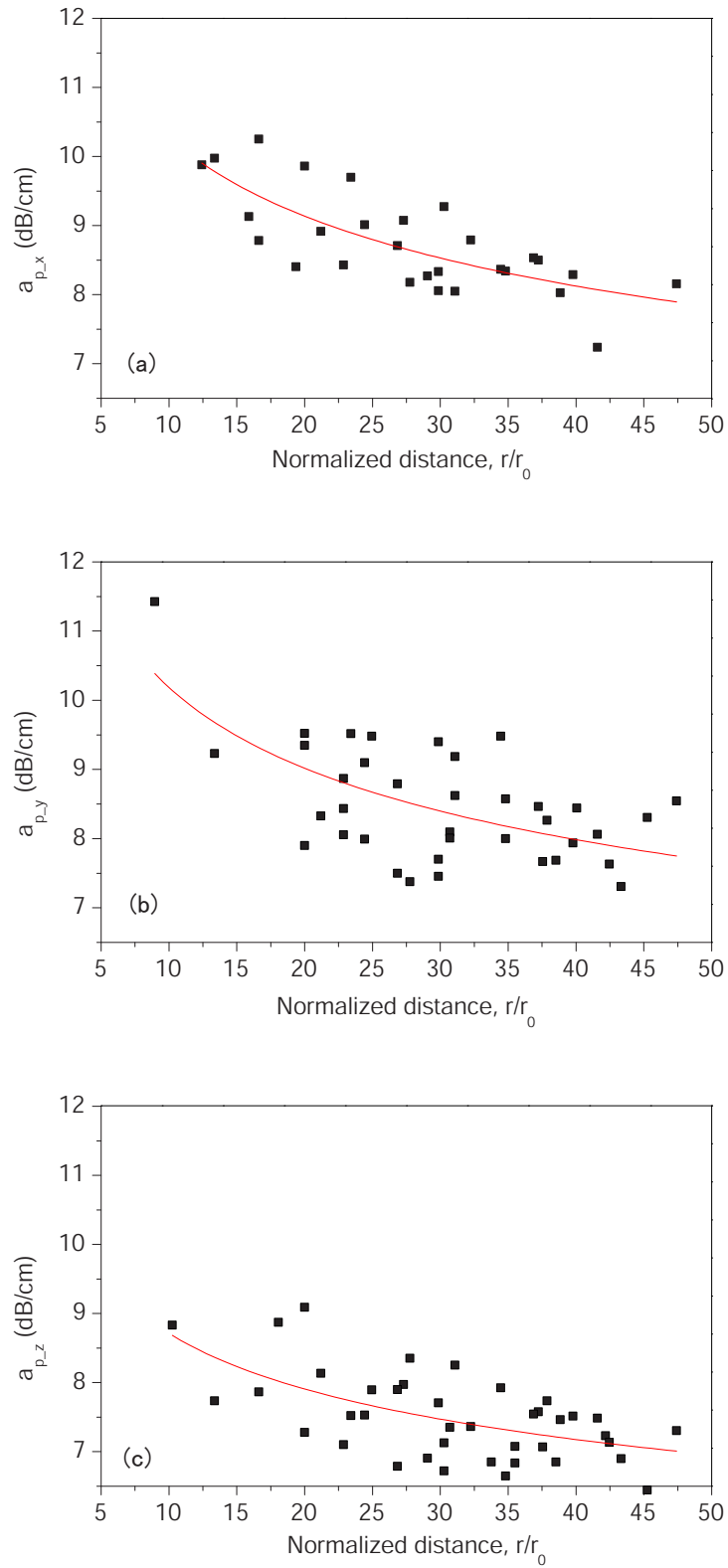


Figure 4.8: Attenuation coefficients as a function of normalized radial distance from impact point for three directions. Lines are power decay fit of data. (a) x; (b) y; (c) z.

The attenuation coefficients in x and y directions are similar but different from that in z direction. It is obvious from Equations 4.6 and Figure 4.8 that at the same distance from the impact point, attenuation parameters in z direction is smaller than those in x and y directions. Therefore, the amplitude of compressional wave in z direction attenuates less than those in the directions normal to the orientation of tensile cracks. This is because tensile cracks extend mostly in z direction, and the effect of cracks on the amplitude of ultrasonic wave is larger in directions normal to the orientation of cracks, which are x and y directions, than that in the direction along crack orientation.

4.4 Analysis and discussion

For hypervelocity impact into brittle materials, both concentric/spherical and radial/tensile cracks are produced (Figure 5 in *Polanskey and Ahrens* [1990]). The radial cracks propagate further than the concentric cracks, since radial cracks are produced when the tensile stress in the elastic regime is greater than the tensile strength of the material, which is usually smaller, by a factor of ten, than the compressive strength. Compressional wave velocity is reduced substantially by cracks oriented with planes normal to the wave propagation direction [*Anderson et al.*, 1974; *O'Connell and Budiansky*, 1974]. In Figure 4.9, the plane of cracks extends in the z direction. Velocity of compressional wave propagating in the x direction is reduced more than that propagating in the z direction. Therefore, the reduction of the measured compressional wave velocity in the x direction by the tensile cracks is expected to be higher than that in the other two directions, which agrees with our observed results (Figure 4.5, 4.6). The fracture of a cracked media can be described by two rather

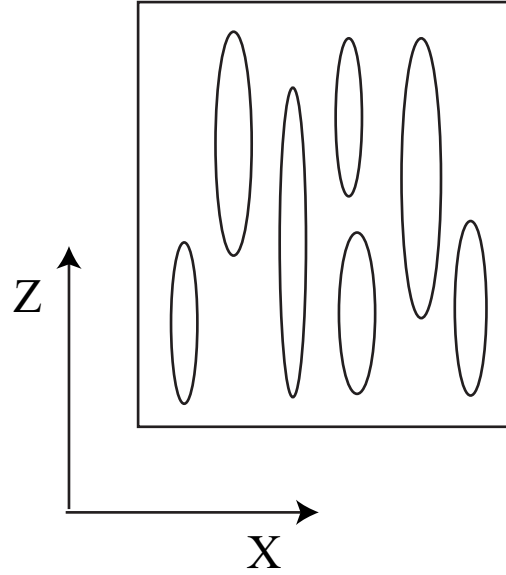


Figure 4.9: Schematic diagram showing effect of aligned cracks on elastic waves propagating at different directions. Compressional wave velocity in x direction is reduced more than that in z direction.

different but ultimately related parameters: (1) Damage parameter, D , used by *Grady and Kipp* [1987] and *Ahrens and Rubin* [1993]; is defined as:

$$D = 1 - \left(\frac{V}{V_0} \right)^2 \quad (4.7)$$

V and V_0 are the effective and intrinsic velocity of the fractured body respectively. (2) Crack density, ε (Equation 2.3).

The two parameters are closely related. In the work of *Ashby and Sammis* [1990] to relate fracture to material strength reduction, damage in a body with inclined cracks of length $2a$ is:

$$D = \frac{4}{3} \pi (\alpha a)^3 N_v \quad (4.8)$$

where α is a geometric constant, and N_v is the number of cracks per unit volume. It is

obvious that this is the same concept as the crack density comparing equations 2.3 and 4.8. In this study, definition of damage parameter in equation 4.7 is used, since it is directly related to our velocity measurements.

From the measured compressional wave velocity of the samples, D_p is calculated from Equation 4.7. Figure 4.10 shows the damage parameter versus the normalized radial distance from the impact point for the three orthogonal directions. The data are fitted by a power decay law function:

$$D_x = 0.95 (r/r_0)^{-0.53 \pm 0.08} \quad (4.9a)$$

$$D_y = 0.99 (r/r_0)^{-0.54 \pm 0.06} \quad (4.9b)$$

$$D_z = 1.04 (r/r_0)^{-0.5 \pm 0.08} \quad (4.9c)$$

Although the measured data are quite scattered, the general trend is that the damage parameters in all the three directions decay with distance from the impact point. Anisotropy is not very obvious from the damage parameter calculation.

The effective elastic moduli of a rock M (replace M with the Young's modulus E , bulk modulus K , and shear modulus μ) is a function of the intrinsic elastic moduli, the matrix and fluid properties, the crack density (ε), the geometry of cracks and the interactions between them [e.g. *O'Connell and Budiansky, 1974*].

The model of *O'Connell and Budiansky [1974]* takes into account the interaction between cracks. It is well known that the solution based on this type of model often does not correspond to experimental data for materials with big contrast in component properties [*Levin and Markvo, 2005*]. According to their equations, the shear modulus becomes zero

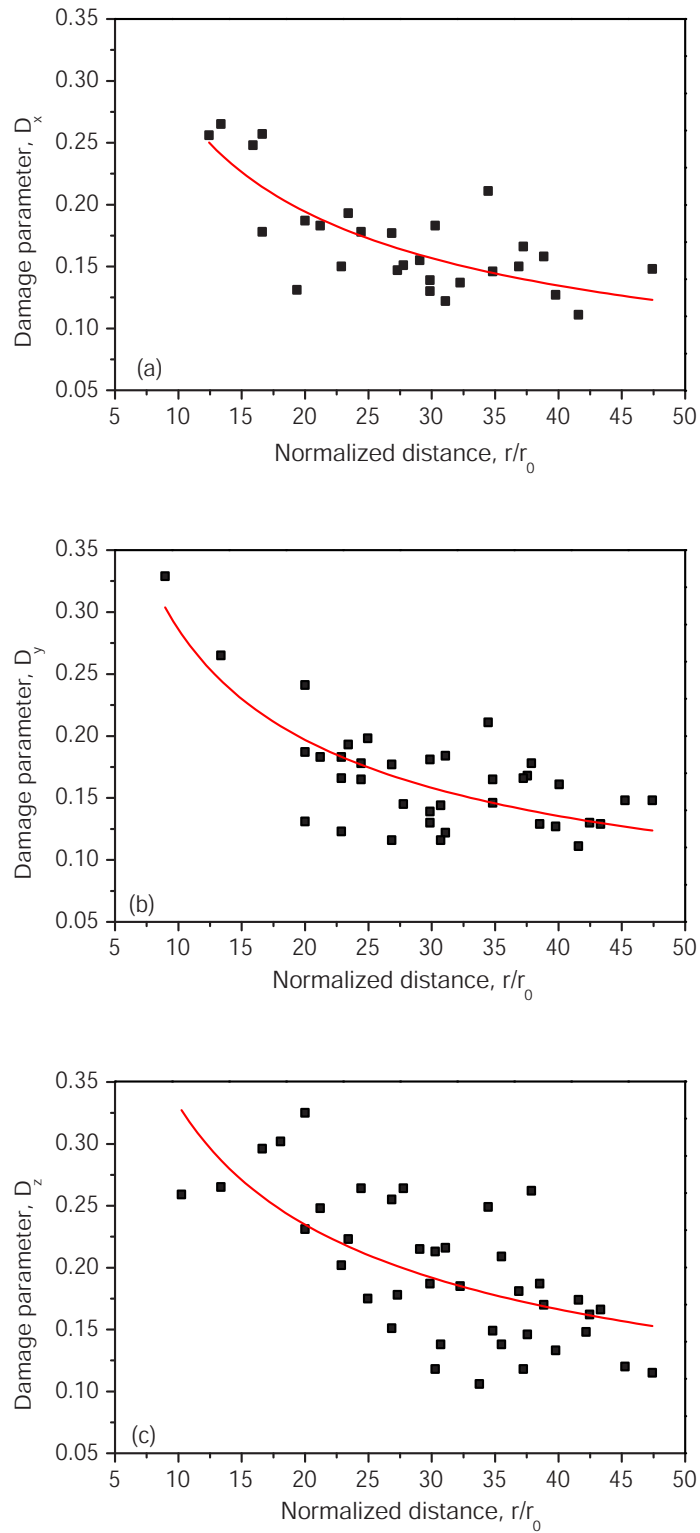


Figure 4.10: Damage parameters as a function of normalized radial distance from impact point for three directions. Lines are power decay fit of data.

when the crack density is higher than a certain value. Another widely used group of models does not take into account the interaction between cracks [e.g. *Anderson et al.*, 1974; *Kachanov*, 1993]. This assumption is possibly reasonable when the volume concentration of inhomogeneities is very small. But for most situations, this group of models which do not account for crack interactions would overestimates crack density from velocity measurements, since it needs more cracks to get same effects when crack interaction does play a role. For natural rocks, the model of *O'Connell and Budiansky* [1974] is preferable although it has its own drawback. Therefore, this model is used in our work to calculate crack density from the measured compressional wave velocities. Figure 4.11 shows the calculated crack density by using the model of *O'Connell and Budiansky* [1974] versus the normalized radial distance from the impact point for the three orthogonal directions. Similarly, the crack density decreases exponentially with the distance for all the three directions:

$$\varepsilon_x = 0.5 (r/r_0)^{-0.58 \pm 0.09} \quad (4.10a)$$

$$\varepsilon_y = 0.5 (r/r_0)^{-0.6 \pm 0.07} \quad (4.10b)$$

$$\varepsilon_z = 0.5 (r/r_0)^{-0.54 \pm 0.08} \quad (4.10c)$$

Uncertainty of the fitting results is high since the data are very scattered. Anisotropy cannot be concluded from these crack density results.

Now we have the information of both damage parameter and the attenuation coefficient for the samples, it would be interesting to see the correlation between the two parameters. Figure 4.12 shows the dependence of attenuation coefficients on the damage parameters for

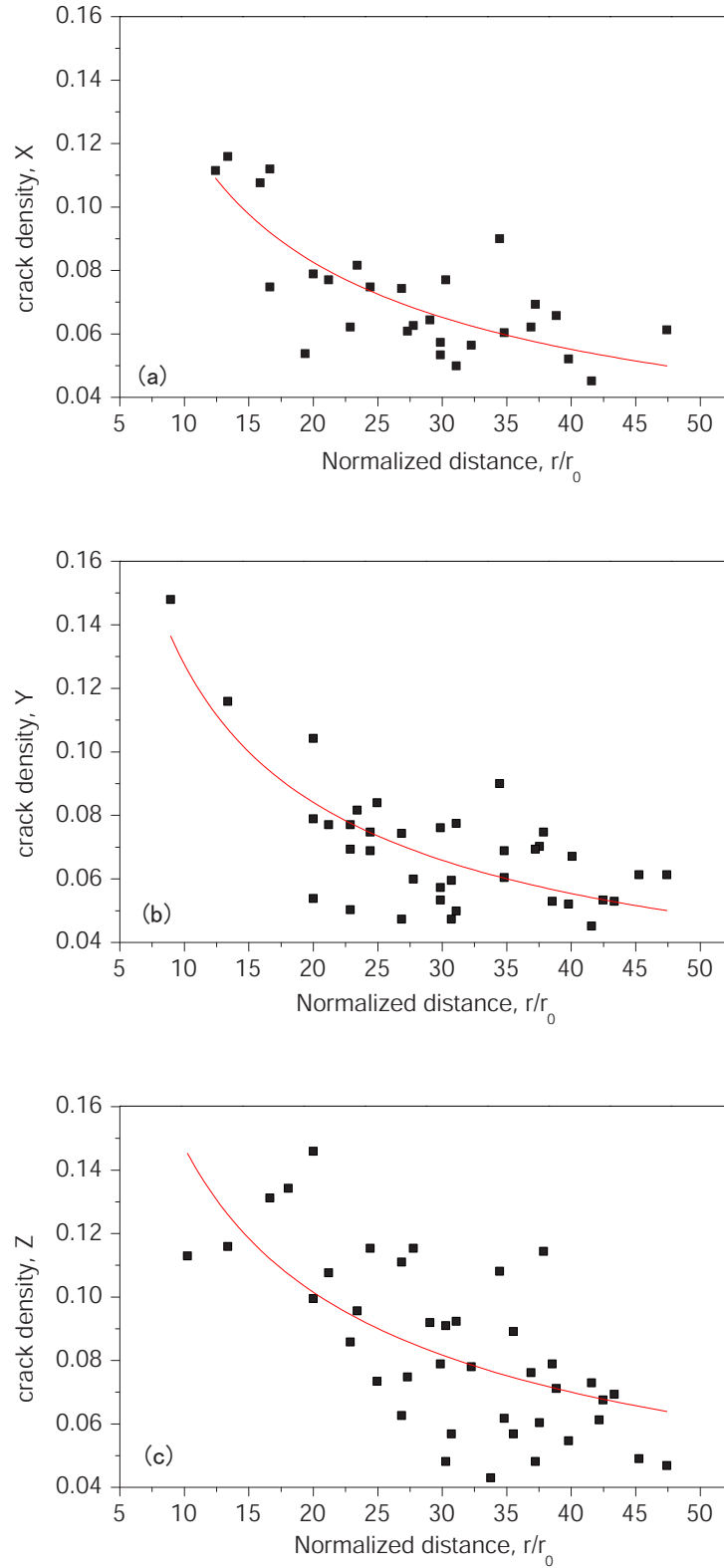


Figure 4.11: Crack densities inverted from measured P-wave velocity by using model of *O'Connell and Budiansky* [1974] as function of normalized radial distance from impact point for three directions. Lines are power decay fit of data. (a) x; (b) y; (c) z.

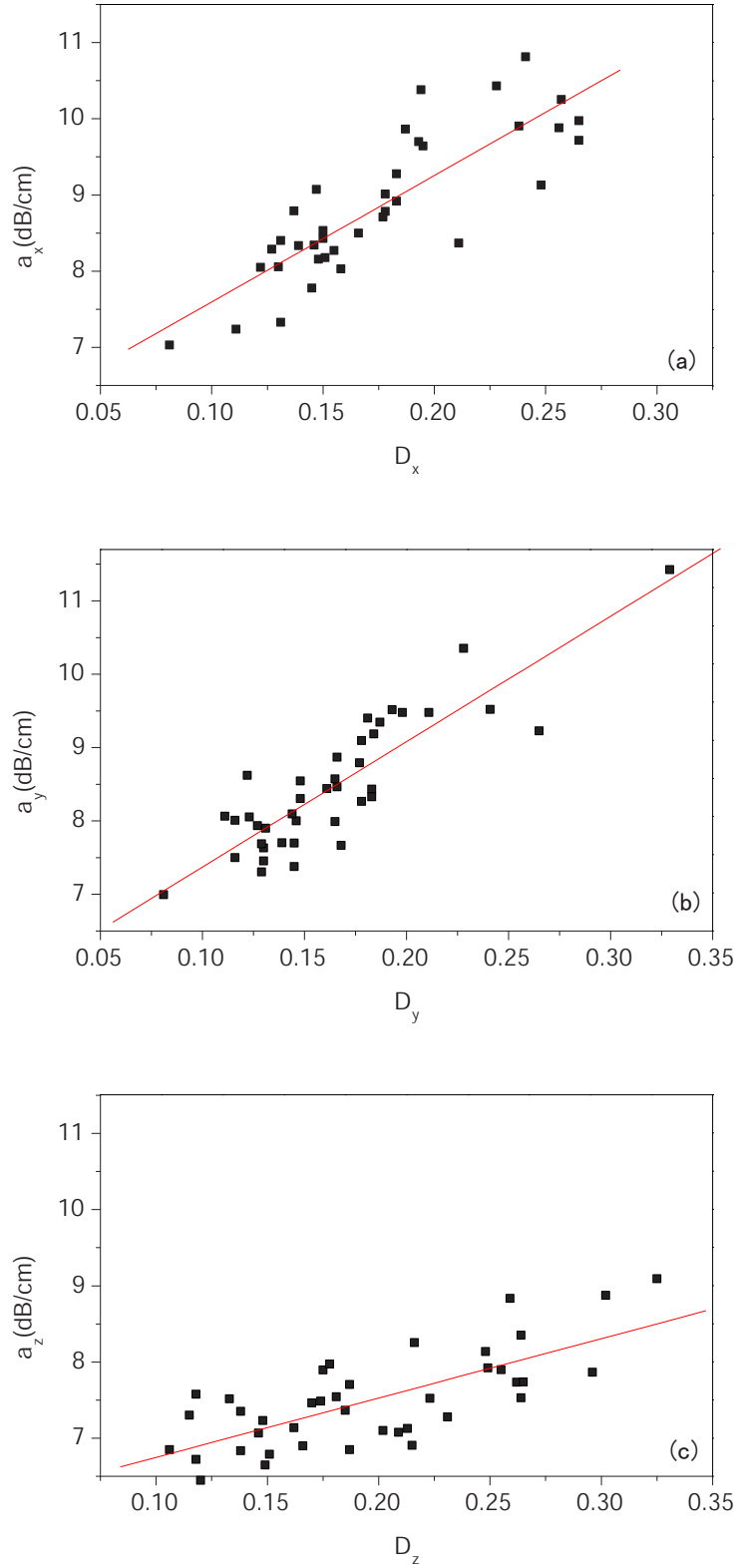


Figure 4.12: Attenuation coefficients versus damage parameter for three directions. (a) x; (b) y; (c) z. Lines are linear fit of data.

the cubes measured in the three directions. The attenuation coefficients increase with the damage parameters consistently for the three situations. The data are fitted with:

$$\alpha_x = 5.94 + (16.59 \pm 1.8) D_x \quad (4.11a)$$

$$\alpha_y = 5.66 + (17.09 \pm 1.6) D_y \quad (4.11b)$$

$$\alpha_z = 5.97 + (7.79 \pm 1.2) D_z \quad (4.11c)$$

unit of α is decibels per centimeter. The intercepts of these equations represent the intrinsic values of the attenuation coefficients of the samples when there is no shock-induced damage happened (D equals zero). The values for the three directions are very close (5.66 to 5.97). However, the slope of the equation for z direction is only about half of the values of x and y directions. This means that for the same damage parameter obtained from measured P wave velocity, the attenuation coefficient in z direction is smaller than the values in x and y directions. The tensile cracks propagating in the impact direction has a larger effect on the attenuation coefficients in directions perpendicular with it. Therefore, the attenuation coefficient is a more useful parameter than the wave velocity in describing the anisotropic orientation of cracks.

Combined with velocity measurement, attenuation coefficient, α_p , can provide microstructure information of cracked media. *Liu and Ahrens* [1997] gave an empirical relation of crack length (a), crack density (ε) and attenuation coefficient for San Marcos gabbro:

$$a = \frac{h\varepsilon}{\alpha_p} \quad (4.12)$$

where h is an undetermined material constant. More work should be carried out in the future to get further information about the microstructure of the media studied.

4.5 Concluding remarks

1 cm cubes are cut from a San Marcos granite target block recovered from an impact cratering experiment. Both compressional wave velocity and attenuation measurements are conducted on these cubes in three orthogonal directions. Damage parameter is calculated from the measured P wave velocity. The theory of *O'Connell and Budiansky* [1974] is used to calculate the crack density of the cracked media from the measured velocity. The main conclusions obtained from this study are listed as follows:

1. Anisotropy is observed from the ultrasonic velocity and attenuation measurement, but not very obvious from the calculated damage parameter and crack density.
2. The measured P wave velocity and the normalized radial distance from the impact point follow an exponential decay relation, shown in equation 4.5.
3. The change of rock properties (D, ε, α) beyond shock pressure regime 1 with the normalized radial distance from the impact point can be expressed by:

$$(D, \varepsilon, \alpha) = \alpha (r/r_0)^b \quad (4.13)$$

where a and b are fitted constants.

4. Attenuation coefficient is a more useful parameter than elastic velocity in studying

the anisotropic orientation of cracks. From Equation 4.11, slope of the linear relation of attenuation coefficient versus damage parameter in x and y directions is about twice of the value in z direction.

Acknowledgments: We appreciate the technical support of E. Gelle, M. Long. We thank Professor G. Ravichandran for the use of ultrasonic attenuation apparatus. We also thank Shiming Zhuang, Tracy Kidd, and Daoyuan Sun for their thoughtful suggestions and discussion.

Chapter 5

Scaling Law

5.1 Introduction

The formation of an impact crater is a combined effect of the size and material of impactor, the impact velocity, the target material property, and other variables such as local gravity. Cm scale experimental study as well as large scale numerical simulations have been carried out over several decades to study the dependence of impact consequence, such as crater ejecta and crater morphology, on the impact conditions [e.g. *Holsapple and Schmidt, 1982; Housen et al., 1983; Kadono and Fujiwara, 2005; O'Keefe and Ahrens, 1981*]. The outcome of one impact event can be predicted from the result of others based on the scaled relations.

The simplest and most common variables used for scaling are size and velocity parameters, but other variables such as gravitational field or material strength can also be included. *Holsapple [1993]* combined a detailed dimensional analysis of scaling for impact processes. For example, the crater dimension such as volume and depth resulted from a hypervelocity impact can be expressed as function of impactor size and velocity, target strength, and gravity [*Holsapple, 1993*]. Various scaling rules exist in the literature for

crater volume and depth, since these variables are easiest to measure for a hypervelocity impact and thus most commonly used in the impact cratering community.

Shock-induced damage and cracking beneath impact craters are less affected by the late stage modification to craters and therefore possible indicator of impact conditions. The damage and cracking have long been recognized on Earth and the Moon [e.g. *Ackermann et al.*, 1975; *Simmons et al.*, 1973]. Preliminary work has been carried out to study damage and cracking beneath craters in the laboratory recently [e.g. *Ahrens and Rubin*, 1993; *Xia and Ahrens*, 2001]. It has been suggested that the cracking information for impact crater is a very useful constraint for the impact history [*Ai and Ahrens*, 2004].

Surprisingly, damage and cracking beneath an impact crater has not yet been studied systematically. The purpose of this work is to explore this important yet not well understood aspect of craters experimentally and to construct a scaling law for damage depth. Section 5.2 gives the theoretical dimensional analysis. The experimental data are presented and discussed in section 5.3. Section 5.4 is the summary and future work.

5.2 Dimensional analysis

Dimensional analysis for impact cratering is traditionally conducted in "strength" and "gravity regime" [*Holsapple*, 1993]. Surprisingly, no clear definition of strength has been given in the available references. It is appropriate to start our dimensional discussion with clarifying some relevant terminologies. According to *Singh* [1989], strength of rock is the ability to resist loads without yielding or fracturing. Ultimate strength of a rock is the maximum value of stress attained before fracture. Tensile strength is the ultimate strength in

tension, while compressive strength is the ultimate strength in compression. The "strength" term, Y , to be used in the next part, refers to the uniaxial compressive strength, which is obtained through uniaxial stress loading test.

Consider the most common and simplest situation: a target material with mass density ρ_t and compressive strength Y impacted by a projectile with radius a and mass density ρ_p at impact velocity V . The surface gravity is g . A single measure of the crater (C), is a function of these variables:

$$C = f(a, \rho_p, V; \rho_t, Y; g) \quad (5.1)$$

Left side of the equation can be replaced by crater volume, crater depth and radius, ejecta, etc. According to the dimensional analysis of *Holsapple* [1993], Equation 5.1 can be simplified using four dimensionless combinations:

$$\bar{C} = f\left(\frac{ga}{U^2}, \frac{Y}{\rho_t U^2}, \frac{\rho_t}{\rho_p}\right) \quad (5.2)$$

\bar{C} is normalized measure of the crater. For example, $\rho_t V/m$ for crater volume, h/a for crater depth, etc. The first term on the right side, traditionally referred as π_2 , represents the effect of gravity level on the crater. The second term represents the effect of material strength, and is denoted as π_3 . The third term is the ratio of mass densities of target and projectile. When the projectile is kilometer-sized, the effect of gravity is large compared with the strength of target, the strength term is ignored ("gravity regime"). Equation 5.2 is simplified into:

$$\bar{C} = f\left(\frac{ga}{U^2}, \frac{\rho_t}{\rho_p}\right) \quad (5.3)$$

On the other hand, when the projectile is only centimeter or meter-sized, the strength of target is more important ("strength regime"). Equation 5.2 becomes:

$$\bar{C} = f\left(\frac{Y}{\rho_t U^2}, \frac{\rho_t}{\rho_p}\right) \quad (5.4)$$

For our experiments carried out at cm scale, strength of the target material is large compared to the lithostatic pressure. Therefore, π_2 is ignored in this work, and Equation 5.4 is used for the next discussion.

Historical scaling approaches to impact cratering showed that the relation between the crater dimension and the strength or gravity term follows a power law [e.g. *Holsapple, 1993; Schmidt and Housen, 1987*]. The density ratio also has effect on the crater morphology. It has been reported that the crater depth is proportional to ρ_p/ρ_t [e.g. *Love et al., 1993*]. In *Schmidt and Housen [1987]*, the normalized crater volume in the strength regime is expressed as:

$$\frac{\rho_t V}{m} = \left(\frac{\rho_t}{\rho_p}\right)^{1-3v} \left(\frac{Y}{\rho_t U^2}\right)^{\frac{-3\mu}{2}} \quad (5.5)$$

where μ and v are scaling exponents to be determined. Again, the left side of Equation 5.5 can be replaced by other measurements of the impact crater, such as crater depth, ejecta velocity, etc.

Damage and fracture feature of impact craters are studied in this work. Here the damage depth D_d is defined as the deepest distance cracks propagate beneath the impact crater, as shown in Figure 3.17). If damage depth of impact crater also follows a power law relation with the strength scaled size (π_3), like other crater measurements such as volume, then the

damage information could be a very useful constraint for impact history. And this is the focus of the next section.

5.3 Experimental data and discussion

Two types of rocks, San Marcos granite and Bedford limestone, are chosen since they are representative of crustal rocks. The compressive strength of the two types of rocks are ~ 300 MPa and ~ 120 MPa respectively. These values are taken from *Singh* [1989], of which the strength of granite is the average value of the data available for granites in their work. Impacts at different combinations of projectile material, size and impact velocity are carried out. Table 5.1 summarizes the impact conditions and the damage depth as well as the final crater dimensions including crater volume, diameter and crater depth for a series of experiments carried out in this study. Shots of 8409001 to 0909 are taken from *Polanskey and Ahrens* [1990], but the damage depths for these recovered targets are measured in this study. The impact velocities vary from as low as 0.276 km/s to 6.49 km/s. The diameter of projectile starts from 0.318 cm for the higher velocity impacts, to 1.27 cm for the lower velocity impacts.

Table 5.1: Summary of experimental parameters

Shot No. ^a	Projectile ^b						Target ^c	Damage	Crater ^d		
	Material	$\rho(\text{g}/\text{cm}^3)$	a(cm)	$m_1(\text{g})$	$m_2(\text{g})$	U(m/s)			Material	$D_d(\text{cm})$	D(cm)
116	Al2024	2.785	0.3	0.75	0.75	1200	SMG	1.5	1.6	0.5	0.3
117	Pb	11.35	0.3	3.2	3.2	1183	SMG	7	7.5	1.5	–
118	Pb	11.35	0.3	3.2	3.2	1162	BL	>15	11	2.5	57.7
120	Pb	11.35	0.3	2.92	2.92	1032	SMG	4	5	1.2	11
124	Cu	8.93	0.3	2.22	2.22	1104	SMG	4	5.8	0.9	8.5
125	Cu	8.93	0.3	2.26	2.26	1165	BL	2.5	6.5	1.5	25.6
1177	Al2024	2.785	0.48	1.26	12.12	1187	SMG	11	3.6	0.7	3.4
1178	Al2024	2.785	0.48	1.26	12.12	1440	SMG	9.5	5.4	1	–
1188	Cu	8.93	0.635	16.25	21.58	276	SMG	0.5	1.5	0.1	0.1
1189	Cu	8.93	0.635	16.25	21.52	620	SMG	5	4.5	0.62	4.2

Table 5.1: (continued)

Shot No. ^a	Projectile ^b				Target ^c	Damage	Crater ^d				
	Material	$\rho(\text{g}/\text{cm}^3)$	a(cm)	m ₁ (g)			m ₂ (g)	U(m/s)	D(cm)	h(cm)	V(cm ³)
1191	Al2024	2.785	0.635	6.61	10.31	1395	SMG	12	9.2	1.3	22.5
1194	Cu	8.93	0.635	16.45	21.71	690	SMG	9	5.5	0.8	7.3
1195	Cu	8.93	0.48	8.35	14.31	958	SMG	12	7.2	1.2	16.7
1196	Al2024	2.785	0.635	6.64	10.34	720	SMG	1	3	0.3	1.0
1197	Cu	8.93	0.635	16.35	21.7	540	BL	14	9	1.3	41.8
1199	Cu	8.93	0.48	8.35	14.29	600	BL	6.5	8.5	1.5	26.8
1200	Al2024	2.785	0.48	2.6	8.53	990	SMG	1	3.5	0.5	2.2
1201	Al2024	2.785	0.635	5.02	10.29	660	BL	6	5.1	1	12.8
1202	Al2024	2.785	0.48	2.59	8.53	986	BL	13	7.4	1.2	36.5
1203	Cu	8.93	0.48	8.35	14.28	750	SMG	>10	-	-	-
1204	Cu	8.93	0.48	8.36	14.27	560	SMG	3	2.7	0.4	1.1

Table 5.1: (continued)

Shot No. ^a	Projectile ^b				Target ^c	Damage	Crater ^d				
	Material	$\rho(\text{g}/\text{cm}^3)$	a(cm)	m ₁ (g)			m ₂ (g)	U(m/s)	D(cm)	h(cm)	V(cm ³)
1205	Pb	11.35	0.48	10.15	16.06	1090	SMG	>15	-	-	-
1206	Pb	11.35	0.48	10.2	16.13	600	SMG	1	3.5	0.5	1.9
1207	Pb	11.35	0.635	19.65	24.91	590	SMG	5.5	4	0.6	3.8
1208	Pb	11.35	0.635	19.65	24.9	800	SMG	12	7	1.1	28.3
1209	Pb	11.35	0.48	10.2	16.12	590	BL	13	8	1.5	36.7
840901	Al	2.785	0.159	0.0443	0.0443	6490	SMGa	2	6.5	1	9
840902	Fe	7.74	0.159	0.1292	0.1292	4600	SMGa	4	9.8	1.5	30
840904	Fe	7.74	0.159	0.1297	0.1297	5440	SMGa	4.5	10.5	1.65	36
840905	Fe	7.74	0.159	0.1297	0.1297	4600	SMGa	3.2	8	1.45	19
840906	Fe	7.74	0.159	0.1297	0.1297	4760	SMGa	3.5	9.2	1.4	23
840907	basalt	2.75	0.238	0.1557	0.1557	2260	SMGa	1.5	3.5	0.7	2.3

Table 5.1: (continued)

Shot No. ^a	Projectile ^b				Target ^c	Damage	Crater ^d				
	Material	$\rho(\text{g/cm}^3)$	a(cm)	m ₁ (g)			m ₂ (g)	U(m/s)	D(cm)	h(cm)	V(cm ³)
840909	steel	7.85	0.318	1.0571	1.0571	1690	SMGa	5	8.3	1.4	25.5

^a116-125: This study, rifle shot; 1177-1209: This study, 20 mm propellant gun; 840901-0909: *Polanskey and Ahrens* [1990]

^b m_1 : mass of projectile only; m_2 : mass of projectile and sabot.

^cSMG: San Marcos granite; BL: Bedford limestone; SMGa: San Marcos gabbro.

^dD: diameter; h: crater depth; V: crater volume.

Two values of mass for projectiles, m_1 and m_2 , are listed in Table 5.1. m_1 is the mass of projectile only, while m_2 is the mass of both projectile and sabot. For shots 1177-1209, the two values are different. These shots are carried out on the 20 mm propellant gun to obtain different sizes of projectile. The spherical projectiles embedded in a lexan sabot are accelerated to desired velocities before impacting the rock targets. Therefore, the apparent projectile radius, a_{pa} , is defined as:

$$a_{pa} = \left(\frac{m_2}{\frac{4}{3}\pi\rho_p} \right)^{1/3} \quad (5.6)$$

where ρ_p is density of the projectile. It is appropriate to use this value, instead of the true projectile radius, a , for the rest of the analysis. For other shots, since no sabot is used, m_1 and m_2 have the same value.

Damage depth is measured directly from the cross section after the recovered target is cut open, determined as the visible distance that the longest tensile crack propagated. This method is proved to be in agreement with the non-destructive tomography method (See Chapter 3). Figure 5.1 and 5.2 illustrate typical damage pattern for San Marcos granite and Bedford limestone respectively, as well as the determined damage depths for the two cases. Both concentric and tensile cracks are observed, as discussed in *Polanskey and Ahrens* [1990]. However, no vertical fractures are observed. This is because the impact velocity is lower than that used in *Polanskey and Ahrens* [1990]. Also shown are the top views of craters of the two shots.

As mentioned in Section 5.2, when the target strength, Y , is large compared to the effect of gravity ("strength regime"), π_2 is ignored in the analysis and only π_3 is used in Equation

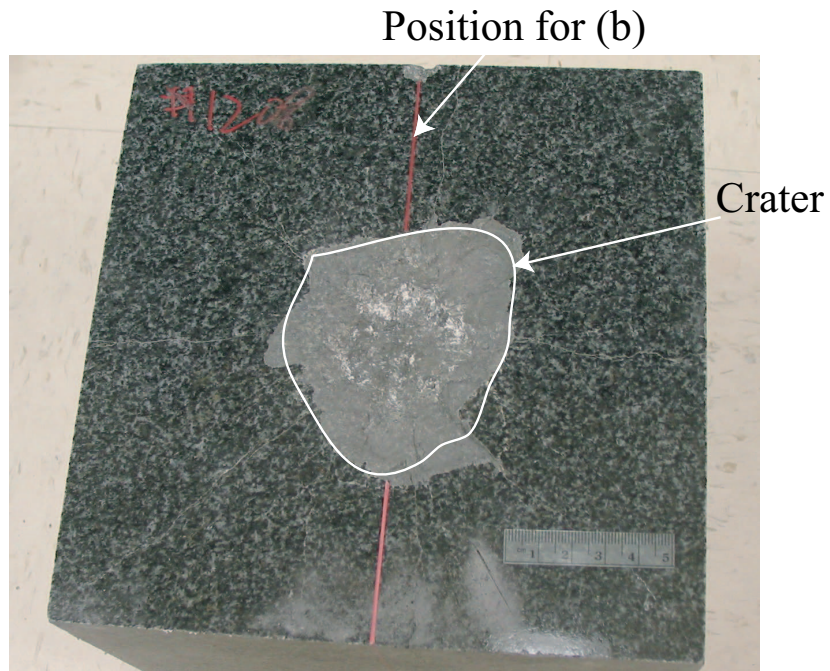
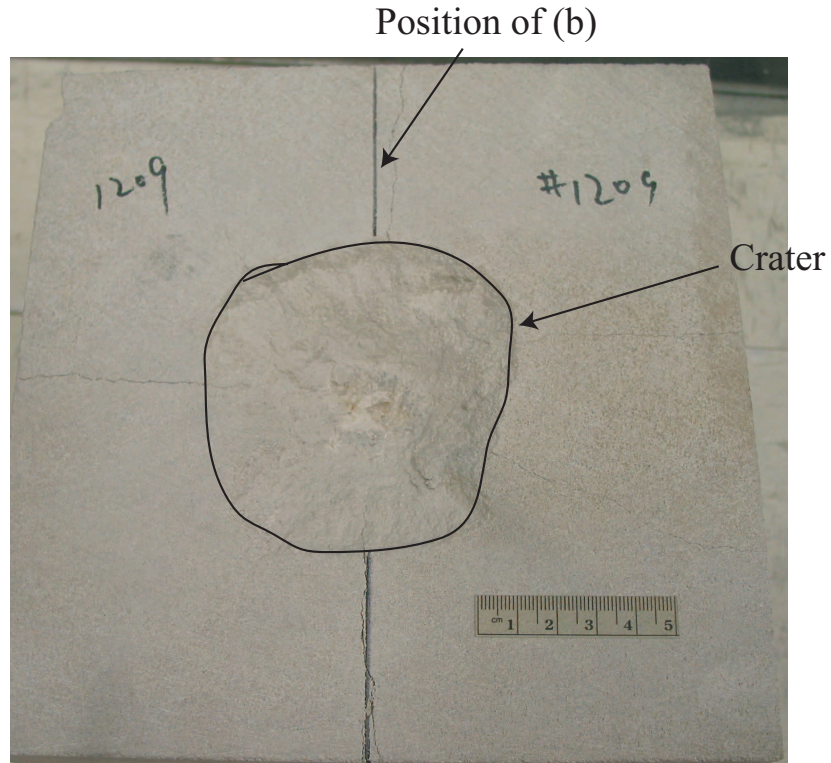
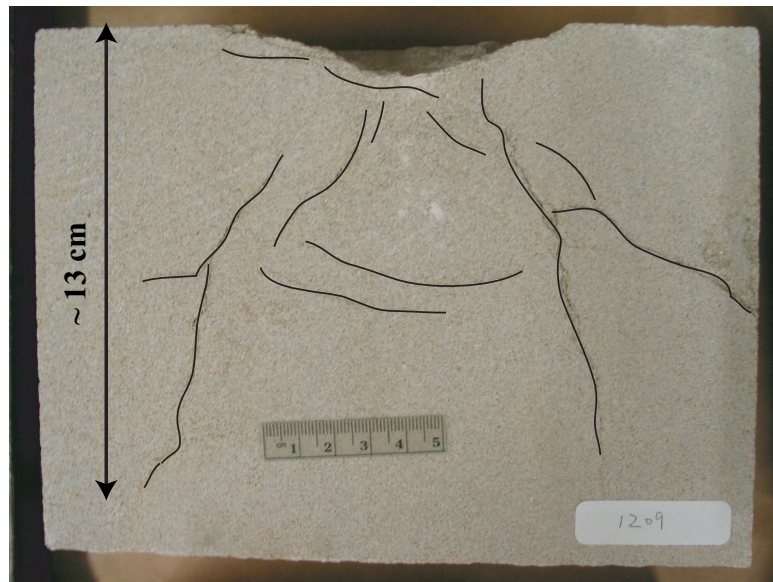


Figure 5.1: Shot 1208, granite impacted by ~ 25 g lead ball (with sabot) at 800 m/s. Scale is 5 cm. (a) Top view showing impact crater. Also shown is cross section position for (b); (b) Cross section of target after being cut open. Tensile cracks extend to ~ 12 cm for this case.



(a)



(b)

Figure 5.2: Shot 1209, limestone impacted by ~ 16 g (with sabot) lead ball at 590 m/s. Scale is 5 cm. (a) Top view; (b) Cross section showing tensile cracks extend to ~ 13 cm for this case.

5.2. This is true for our experiments carried out at cm scale. The effect of gravity, term π_2 is ignored throughout the analysis in this work.

Based on the dimensional analysis in the previous section, the damage depth of craters listed in Table 5.1 normalized by the apparent projectile radius, a_{pa} , over the projectile-to-target density ratio, is plotted versus the strength parameter, π_3 , as shown in Figure 5.3. The strength size extends from 10^{-3} to 10^1 , and the normalized damage depth over density ratio extends from 10^0 to 10^4 . As expected, the damage depth generally follow a power-law trend. The slope of the fitted line is -1.27, which corresponds to the value of μ as 0.8, according to Equation 5.5. For comparison, both energy and momentum scaling are also plotted in the figure. Slope of energy scaling is -1, corresponding to $\mu=2/3$, while slope of momentum is -0.5, corresponding to $\mu=1/3$. Fitting result of our data follows the energy scaling. This result is very interesting and intriguing, since this indicates that the damage beneath craters is a function of of impact conditions and the damage information could be used as a very useful constraint for impact history. However, no damage depth data of cm scale experiments are available from literature.

The normalized crater volume over density ratio is also plotted versus the strength parameter, π_3 (Figure 5.4). The normalized crater volume extends from 10^{-3} to 10^3 . Also included are data from *Payne* [1965] for impacts into metals. It is observed that the data from this study and those from *Polanskey and Ahrens* [1990] follow the same trend, but not the data from *Payne* [1965] for metals. Data from this study and those from *Polanskey and Ahrens* [1990] are fitted by a power-law function. The slope of the fitted line is -1.79, which implies that $\mu=1.2$ according to Equation 5.5. This inconsistency might be caused

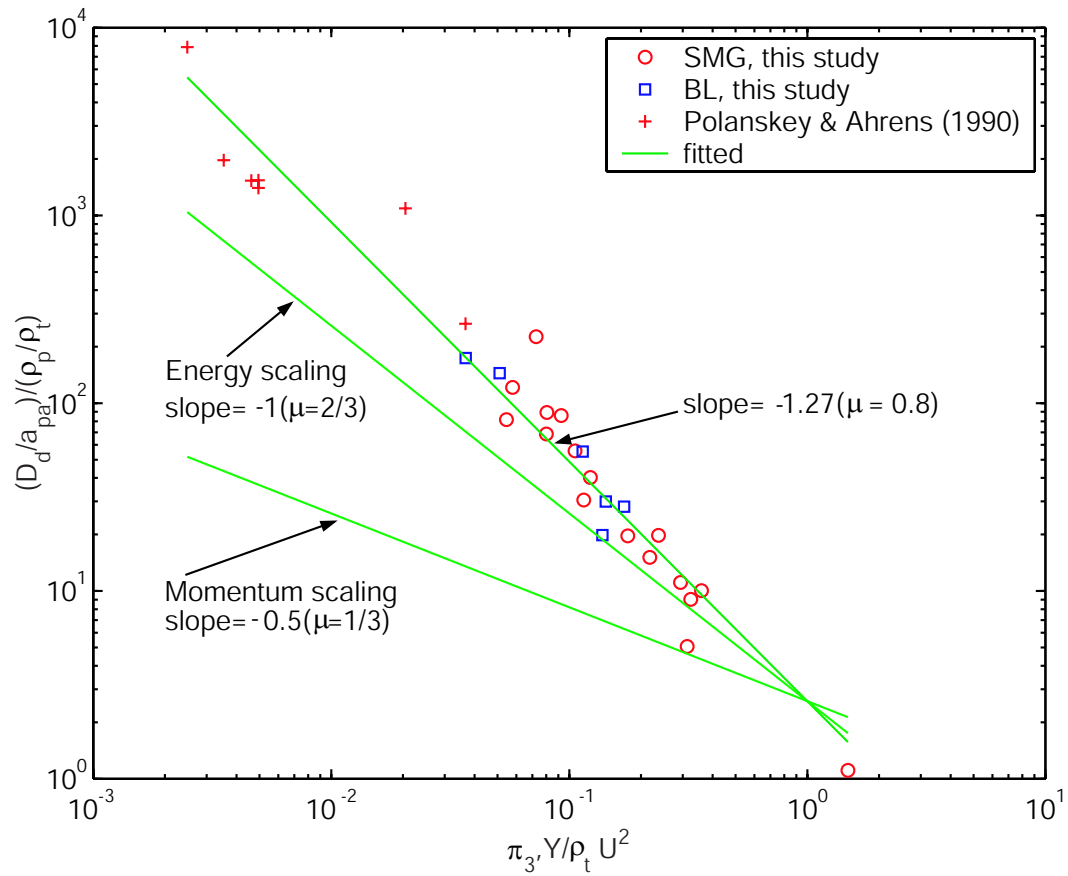


Figure 5.3: Normalized crater damage depth by apparent projectile radius, D_d/a_{pa} , over projectile-density ratio, ρ_p/ρ_t , as power-law function of strength parameter, $\pi_3 = Y/\rho_t U^2$. Slope of fitted line is -1.27. Note log-log scale of the plot.

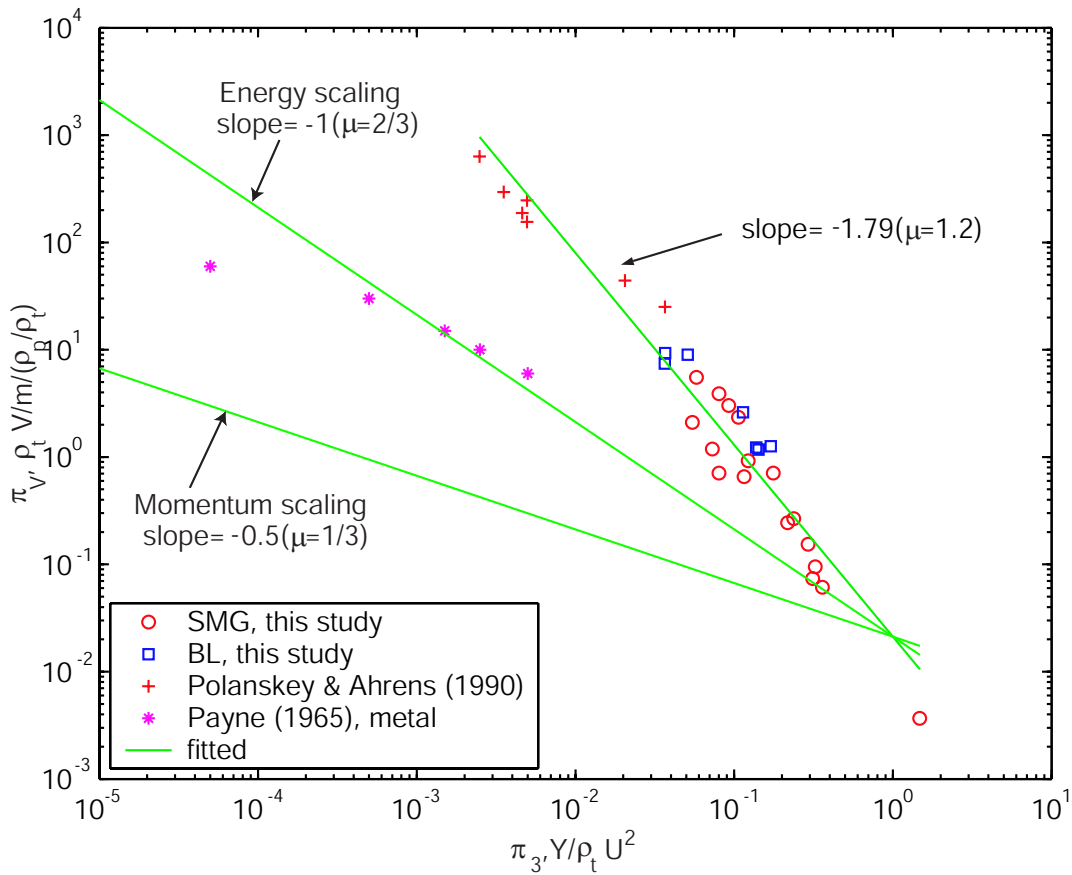


Figure 5.4: Normalized crater volume by apparent projectile volume, $\rho_t V/m$ as a function of strength parameter, π_3 . Definition of parameters are same as in Figure 5.3. Data for impacts into metal taken from *Payne* [1965] are also plotted for comparison. Slope of fitted line is -1.79 .

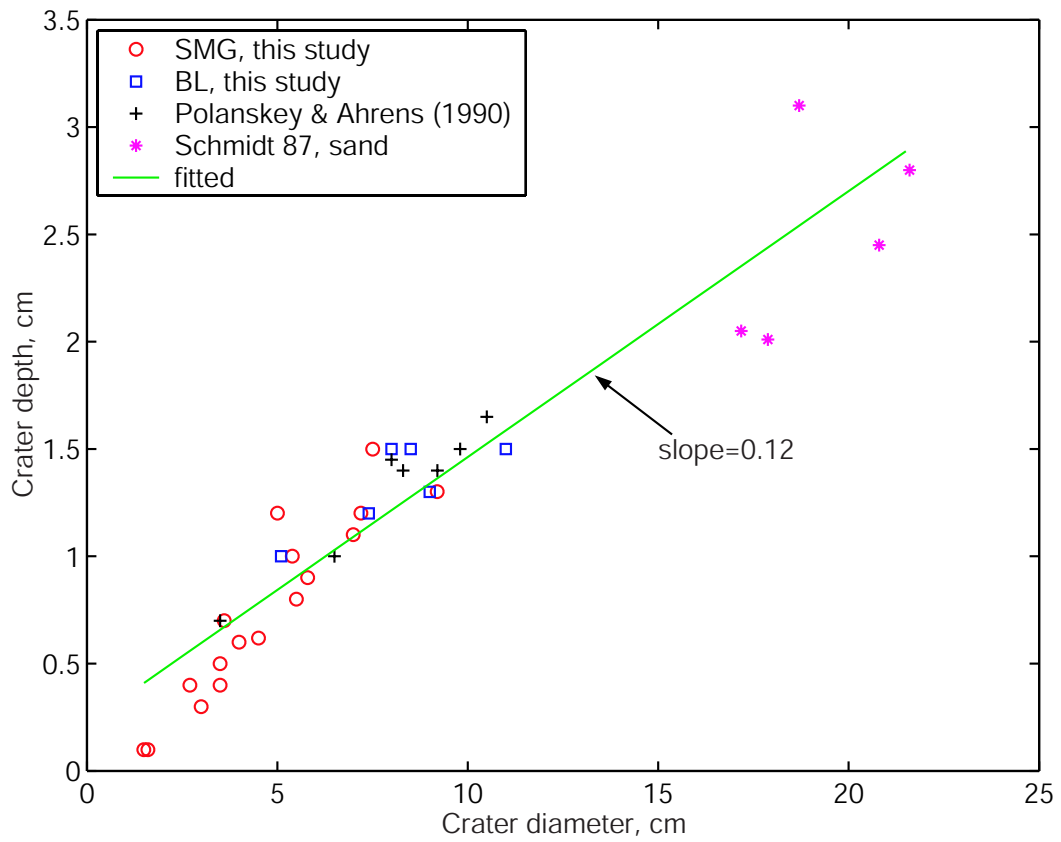


Figure 5.5: Plot of crater depth as a function of crater diameter. Linear relation is observed, and slope is 0.12.

by confusion of definition of "strength" in literature. Strength is a strain rate dependent material constant, as discussed in Chapter 2. Strength for materials under hypervelocity impact is higher than that of relatively lower velocity impact. Again, both energy and momentum scaling are shown in this figure for comparison. Our result shows the combining effect of strain rate on strength and energy scaling.

The crater depth as a function of crater diameter is plotted in Figure 5.5. For comparison, data from *Schmidt and Housen* [1987] are included. A very clear linear relation is observed for all the data, and the slope is 0.12.

5.4 Summary

Two types of rocks, San Marcos granite and Bedford limestone, were impacted by projectiles with various sizes and types at different velocities. Damage depth, D_d for these hypervelocity impact craters was discussed in this work. It was found that the damage depth is a function of the impact velocity and the physical properties of target/projectile combination. In general, the damage depth normalized by the apparent projectile radius, a_{pa} , follows a power-law function with the strength scaled size, which can be expressed as:

$$\frac{D_d}{a_{pa}} \propto \left(\frac{\rho_p}{\rho_t} \right)^A \left(\frac{Y}{\rho_t U^2} \right)^B \quad (5.7)$$

where A and B are constants. In this study, A equals 1 and B equals -1.27. This indicates that the damage depth would be an important measure for impact craters, yet not being studied systematically before. If combined with other measures such as crater volume and

depth, it is possible that the damage depth can provide useful constrains for impact history.

This work is the preliminary step in studying damage depth for impact craters. There are still a lot of issues to be explored. Data on damage information of impact craters, both from laboratory experiments and from craters in the field, are relatively scarce. More laboratory data are needed under controlled conditions. First, more types of targets such as sand, sandstone, ice, etc, should be tested to represent the terrestrial and extraterrestrial surfaces. Second, impact at different angles should be carried out systematically. Third, effect of gravity is ignored in this work. However, this important effect should be included in the future. Experiments at different gravity scale should be carried out. Fourth, numerical calculation of large scale impacts should be used as a complimentary tool to simulate impacts at different impact conditions, including the effect of gravity.

Although our work is only the first step in exploring the damage beneath impact crater, the result is very intriguing. Information of shock-induced damage and cracking below impact craters is an important constraint for impact history. It sheds light on the possibility of using damage information of craters as a constraint for impact history. Combined with other known parameters such as crater dimension, projectile and target properties, damage and cracking could provide useful yet unrecognized information on the impact history. Our work will provide a direction for deploying seismic investigation of low-velocity zone beneath impact craters in the field.

Chapter 6

Shock-Induced Damage beneath Oblique Impact Craters

6.1 Introduction

Natural impact events always happen at impact angles less than vertical [*Gilbert*, 1893; *Shoemaker*, 1962]. However, a large amount of work in the impact cratering field, both theoretical and experimental, is performed under normal impact condition to allow the simplification of the problem to two dimensions because of axial symmetry, since vertical impacts are regarded as a good representation of oblique impacts based on the fact that oblique hypervelocity impacts with impact angle higher than 30° (90° means vertical impact) produce circular craters similar to that observed in vertical hypervelocity impacts, according to the comprehensive study of *Gault* [1978].

Oblique impact craters, Chicxulub and Manson for example [*Schultz and Anderson*, 1996; *Schultz and D'Hondt*, 1996], are often identified by the ejecta pattern, the geophysical features of the crater, and/or the elongated crater shape for craters impacted at extremely low angles. However, late stage collapse of the crater and geological process such as erosion and sedimentation would modify and mask some of these features.

The increase of computation capability of computers during the last decade makes it possible to carry out three dimensional numerical simulations of hypervelocity oblique impacts. *Pierazzo and Melosh* [2000] did calculation for hypervelocity oblique impacts at different impact angles and concluded that even though the position of the shock front as it propagates through the target appears symmetric around the impact point for oblique impacts, the peak shock pressure experienced by the rock target is asymmetric (Figure 6.1). *Dahl and Schultz* [2001] also observed stress wave asymmetries in oblique hypervelocity impact experiments. Unfortunately, stress wave cannot be measured directly for a natural impact crater in the field. But this intriguing result leads us to look into the shock-induced damage and cracking, which is directly related to the peak shock pressure, beneath craters by oblique impacts.

From the discussion of previous chapters, shock-induced damage beneath impact crater is a potential constraint for impact history. However, the shock-induced damage beneath oblique impact craters has not been paid attention to by far. This study presents results of laboratory oblique impacts designed to measure the shock-induced damage beneath impact craters. Again, San Marcos granite and Bedford limestone, are chosen as target materials [e.g. *Ai and Ahrens*, 2004; *Ahrens and Rubin*, 1993], because they provide convenient representative material for low-porosity crystalline rock and high-porosity sedimentary rock. The low velocity zone beneath the craters caused by shock-induced damage in the recovered targets is mapped.

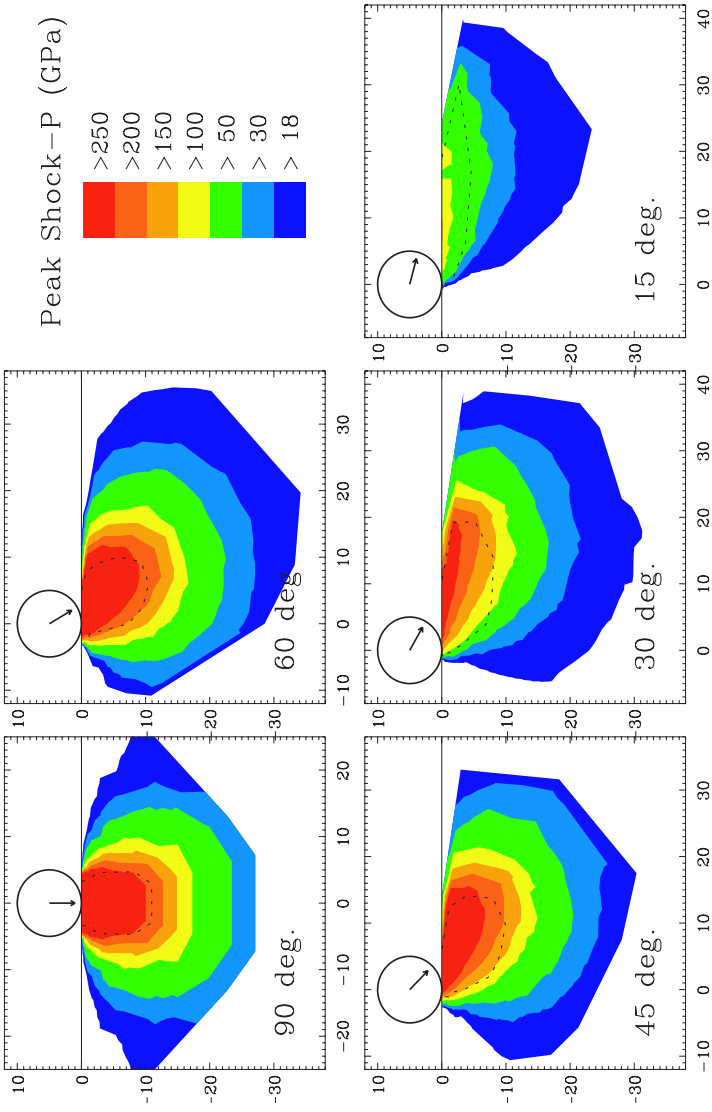


Figure 6.1: Peak shock pressure contours in the plane of impact for a series of 3D hydrocode simulations at various impact angles. The projectile, 10 km in diameter, is shown for scale. *Vectors* illustrate the direction of impact. From *Pierazzo and Melosh [2000]*, Figure 3.

6.2 Experiments

Initially, 20x20x15 cm blocks were cut from San Marcos granite and Bedford limestone. Cratering experimental setup is the same as that described in Chapter 3, except that the impact angle is at 45° . The projectile used for both shots is a lead bullet, with radius of 0.3 cm and mass of 3.2 g. Impact velocity into granite is 1.2 km/s, and 1.16 km/s for limestone. The impact velocity is chosen not to fragment the target, while to still produce measurable compressional wave velocity reduction caused by the shock-induced damage in the recovered target.

The compressional wave velocities beneath the oblique impact craters are mapped on two central planes, one is plane A, the plane containing the projectile trajectory; the other is plane B, the plane normal to plane A (Figure 6.2a). The tomography method described in Chapter 3 is used for mapping the velocity structure in San Marcos granite. For Bedford limestone, dicing method described in Chapter 4 is used to measure the velocity directly.

6.3 Results and discussion

6.3.1 Experimental results

Figure 6.3 shows the inverted compressional wave velocity structures of Plane A and B to depth of 4 cm, for the recovered San Marcos granite block. The lowest P-wave velocity in the highly damaged region beneath and near the crater reaches ~ 5 km/s (Figure 6.3), and the reduction is $\sim 20\%$ from the intrinsic velocity of 6.3 ± 0.1 km/s, determined at 5 MHz. The depth of the low velocity zones for this recovered granite target extends to 2-3 cm on

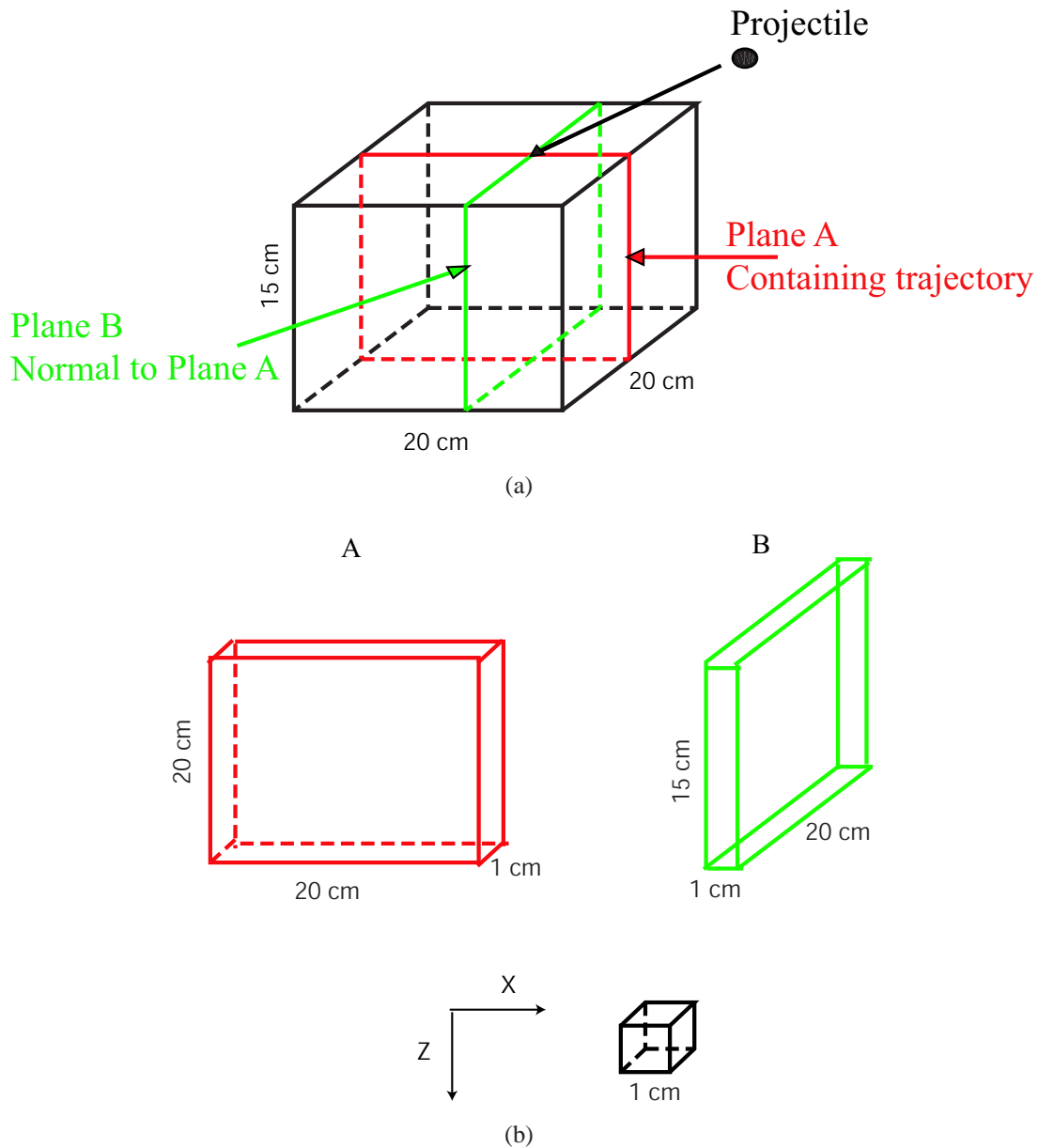


Figure 6.2: (a) Oblique impact geometry of 20x20x15 cm block. Tomography measurement carried out on two central planes. Plane A containing projectile trajectory, plane B is normal to plane A; (b) Diagram showing orientation for dicing method for limestone. 1 cm center plane cut from the recovered target, then 1-cm cube cut from the center plane for velocity measurement in two orthogonal directions, X and Z, which are the horizontal and vertical impact direction respectively.

both profiles for Plane A and B. Asymmetry is observed, although not very obvious, for the inverted compressional wave structure of Plane A, the plane containing the projectile trajectory (Figure 6.3a). Peak damage extends along the downrange direction from the impact point. Asymmetry is not observed for Plane B, the plane normal to Plane A (Figure 6.3b).

In the field, craters larger than 1 km in diameter would inevitably experience uplift as well as late stage modification such as erosion [*Melosh*, 1989]. Although the morphology or the crater could be modified by such processes greatly, geophysical features such as gravity anomaly and low seismic velocity structure beneath impact craters would be preserved and are possible to be used as constraints for impact history. To simulate the erosion of upper surface of the crater, a top layer of one centimeter thickness is cut off and the P-wave velocity profiles of the two center planes of the remaining granite block are mapped again using the tomography method. The inverted results for the two planes from the top surfaces to 3 cm depth (the same position of 4 cm depth as before cut) are shown in Figure 6.4. Similarly, asymmetry of the low velocity zone is observed in Plane A, the plane containing the projectile trajectory, and higher reduction of the velocity is observed along the downrange (Figure 6.4a). The damage pattern in Plane B, the plane normal to Plane B is relatively symmetric (Figure 6.4b).

Compressional velocity measurements of Plane A and Plane B for the recovered Bedford limestone using the dicing method are listed in Table 6.1 and 6.2 and shown in Figure 6.5 and 6.6. The measurement is carried out in two orthogonal directions, x , defined as the horizontal direction which is parallel to the impact surface, and z , which is perpendicular

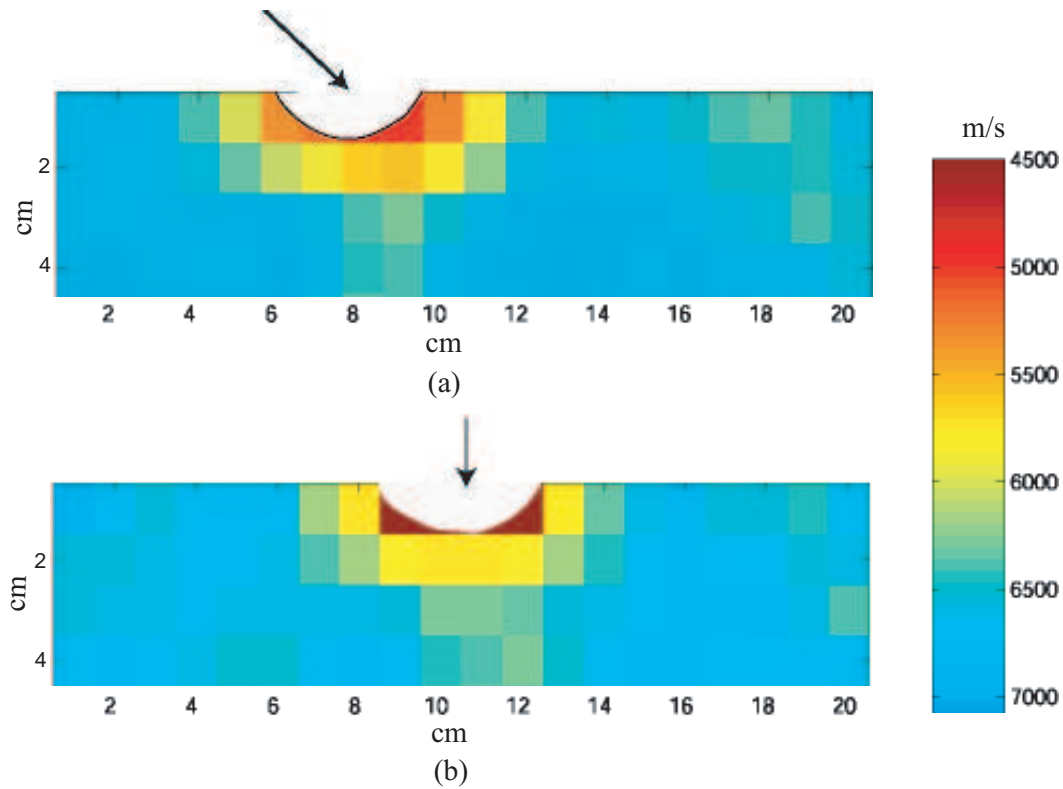


Figure 6.3: Inverted compressional wave profiles of two planes defined in Figure 6.2 for oblique impact crater (impact angle 45°) in San Marcos granite, shot 121, using tomography method. Thick lines define crater dimension. (a) Plane A. *Vector* illustrates direction of impact; (b) Plane B. Impact direction is 45° to the paper. *Vector* is horizontal projection of the direction of impact.

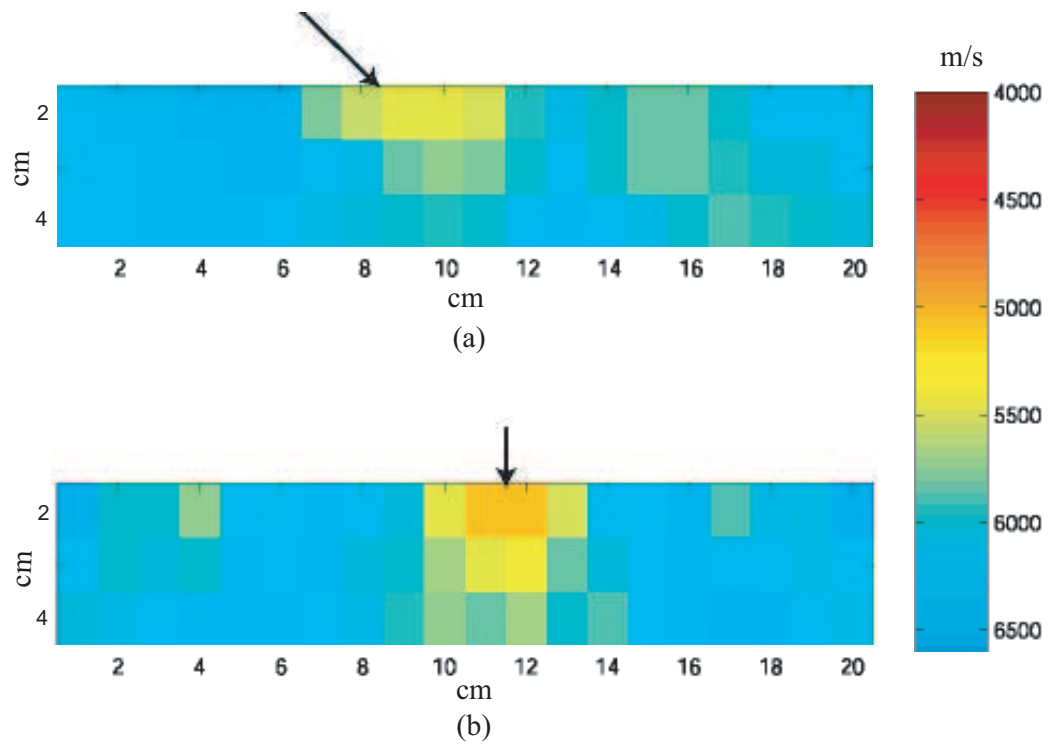


Figure 6.4: Inverted compressional wave profiles of same central planes as in Figure 6.3, except that 1 cm top surface layer is cut off. See Figure 6.3 for explanation of *Vectors*. (a) Plane A; (b) Plane B.

with the impact surface (See Figure 6.2b for detailed explanation of the orientation). For those cubes beneath and near the impact crater region, the low velocity can be as low as 2.7 km/s, with the reduction of $\sim 40\%$, from 4.6 ± 0.2 km/s, the intrinsic compressional velocity of Bedford limestone [Ahrens and Rubin, 1993]. The damage depth identified from these inverted results extends to 3~4 cm for this oblique impact shot into Bedford limestone. Both directions, x and z, of Plane A, the plane containing the projectile trajectory, show asymmetric pattern; and higher velocity reduction is observed in the downrange (Figure 6.5). In contrast, the inverted result for Plane B, which is the plane normal to Plane A, shows a more symmetric pattern (Figure 6.6).

Table 6.1: Compressional wave velocity beneath oblique impact crater in Bedford limestone, shot 122, plane A, along projectile trajectory.

(a) X direction																
Radius from Crater Center Line, cm																
	-7.5	-6.5	-5.5	-4.5	-3.5	-2.5	-1.5	-0.5	0.5	1.5	2.5	3.5	4.5	5.5	6.5	7.5
Depth(z), 0.5 cm	4.63	4.66	-	-	-	-	-	-	-	-	-	-	-	4.71	4.68	-
Depth(z), 1.5 cm	4.95	4.69	4.66	-	-	-	-	-	-	-	-	4.58	4.64	4.63	4.63	4.7
Depth(z), 2.5 cm	4.84	4.74	4.7	4.52	4.43	3.3	3.03	3.06	3.49	4.2	4.5	4.44	4.52	4.53	4.54	4.72
Depth(z), 3.5 cm	4.75	4.73	4.71	4.6	4.5	4.1	3.2	4.0	4.13	4.21	4.46	4.52	4.51	4.82	4.8	4.8
Depth(z), 4.5 cm	4.83	4.74	4.54	4.41	4.63	4.45	3.84	4.4	4.41	4.49	4.3	4.57	4.6	4.54	4.73	-
Depth(z), 5.5 cm	4.68	4.79	4.79	4.66	4.55	4.74	4.36	4.18	4.53	4.66	4.5	4.57	4.6	4.75	4.72	4.78

(b) Z direction																
Radius from Crater Center Line, cm																
	-7.5	-6.5	-5.5	-4.5	-3.5	-2.5	-1.5	-0.5	0.5	1.5	2.5	3.5	4.5	5.5	6.5	7.5
Depth(z), 0.5 cm	4.71	4.62	4.85	-	-	-	-	-	-	-	-	-	-	4.72	4.76	-
Depth(z), 1.5 cm	-	4.65	4.61	4.40	4.57	-	-	-	-	-	-	-	-	4.60	4.86	4.74
Depth(z), 2.5 cm	4.36	4.59	4.31	4.27	4.34	4.43	3.9	3.23	2.62	2.44	3.24	3.7	4.39	4.56	4.75	4.7
Depth(z), 3.5 cm	4.71	4.6	4.46	4.31	4.07	4.34	3.90	4.14	3.15	3.71	3.94	4.2	4.36	4.57	4.72	4.71
Depth(z), 4.5 cm	-	4.68	4.63	4.46	4.4	4.22	3.71	3.89	4.15	4.03	4.47	4.65	4.17	4.3	4.7	4.59
Depth(z), 5.5 cm	4.7	4.51	4.39	4.49	4.5	4.09	4.47	4.35	4.45	3.95	4.5	4.54	4.5	4.35	4.37	4.51

Table 6.2: Compressional wave velocity beneath oblique impact crater in Bedford limestone, shot 122, plane B, Normal to projectile trajectory.

(a) X direction														
Radius from Crater Center Line, cm														
	-6.5	-5.5	-4.5	-3.5	-2.5	-1.5	-0.5	0.5	1.5	2.5	3.5	4.5	5.5	6.5
Depth(z), 0.5 cm	-	-	-	-	-	-	-	-	-	-	-	4.71	4.74	4.87
Depth(z), 1.5 cm	5.06	4.89	4.78	-	-	-	-	-	-	4.26	4.35	4.44	4.91	4.74
Depth(z), 2.5 cm	5.09	4.85	4.84	4.66	4.24	3.46	3.3	4.43	4.25	4.54	4.59	4.76	4.68	4.86
Depth(z), 3.5 cm	4.79	4.74	4.72	4.7	4.67	4.27	4.1	4.3	4.58	4.47	4.71	4.75	4.83	4.65
Depth(z), 4.5 cm	4.77	4.51	4.55	4.75	4.79	4.6	4.45	4.63	4.59	4.43	4.56	4.42	4.42	4.75
Depth(z), 5.5 cm	4.72	4.55	4.49	4.65	4.72	4.65	4.74	4.55	4.73	4.73	4.58	4.57	4.67	4.61

(b) Z direction														
Radius from Crater Center Line, cm														
	-6.5	-5.5	-4.5	-3.5	-2.5	-1.5	-0.5	0.5	1.5	2.5	3.5	4.5	5.5	6.5
Depth(z), 0.5 cm	-	-	-	-	-	-	-	-	-	-	-	4.6	4.72	4.78
Depth(z), 1.5 cm	4.91	4.87	4.7	-	-	-	-	-	-	-	4.52	4.66	4.65	5.02
Depth(z), 2.5 cm	5.02	4.9	4.7	4.4	4.03	3.22	3.24	3.7	4.03	4.42	4.66	4.78	4.69	5.0
Depth(z), 3.5 cm	4.93	4.86	4.8	4.82	4.64	3.84	3.94	4.5	4.53	4.4	4.57	4.79	4.74	4.89
Depth(z), 4.5 cm	4.76	4.83	4.29	4.6	4.89	4.49	4.47	4.65	4.47	4.62	4.4	4.6	4.69	4.73
Depth(z), 5.5 cm	4.89	4.76	4.58	4.58	4.81	4.4	4.5	4.54	4.66	4.74	4.69	4.84	4.67	4.61

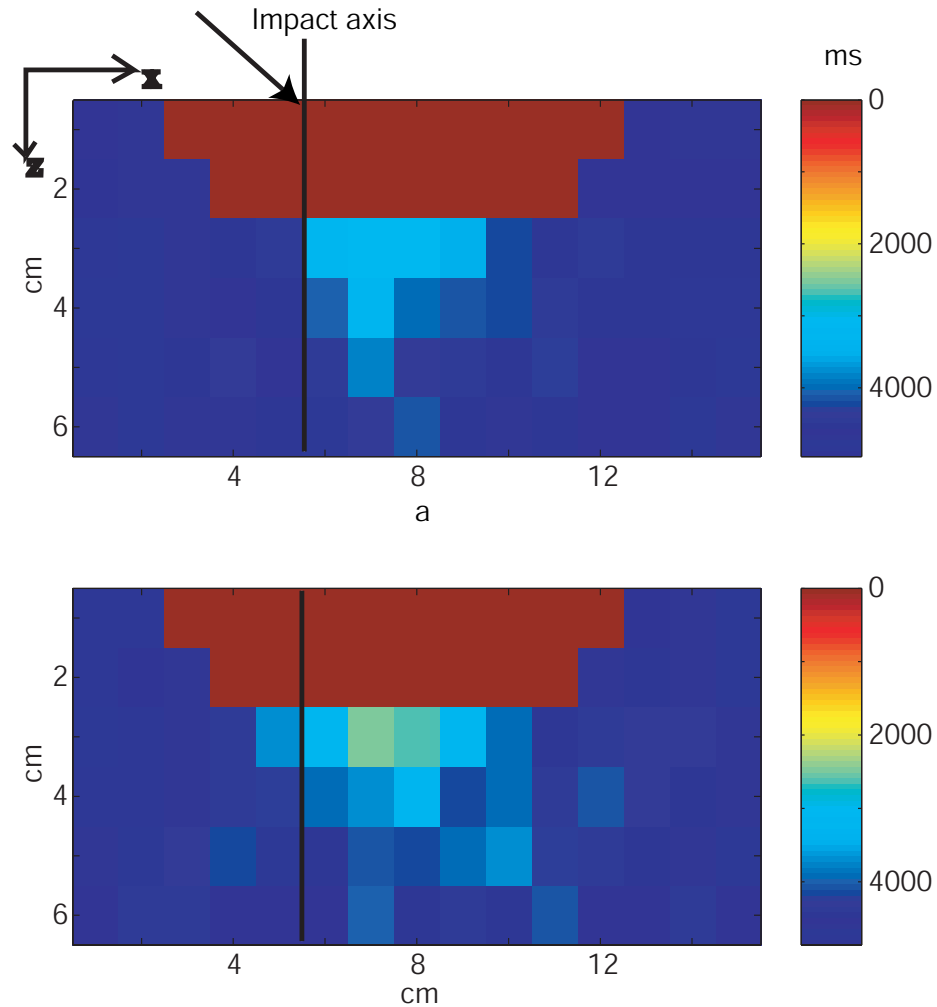


Figure 6.5: Compressional wave profiles of plane A for oblique impact crater (impact angle 45°) in Bedford limestone, shot 122, using dicing method. Two directions, x and z, are horizontal, parallel to impact surface, and vertical impact directions separately. Black solid line is impact axis. See Figure 6.2b for explanation. Zero velocity represents unmeasurable. (a) x direction; (b) z direction.

6.3.2 Discussion

The peak pressure for oblique impact craters is strongly dependent on the vertical component of impact velocity, $V \sin \theta$. According to the direct measurement in the laboratory by *Dahl and Schultz* [2001], the peak pressure for oblique impacts follows a modified scaling

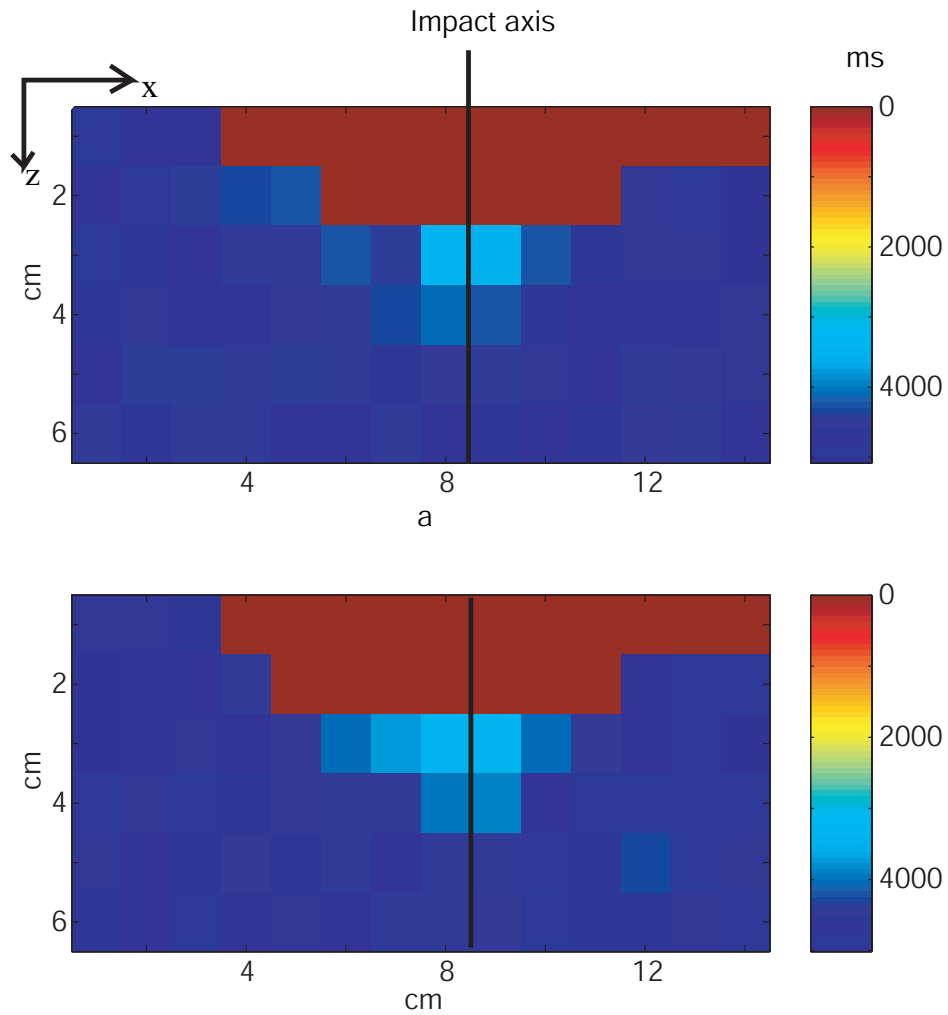


Figure 6.6: Compressional wave profiles of plane B for shot 122 using dicing method. All notes same as in Figure 6.5. (a) x direction; (b) z direction. Asymmetry is not observed.

law:

$$\frac{P_r}{\rho_0 c_0^2} \sim \left[\left(\frac{c_0}{V \sin \theta} \right)^\mu \left(\frac{r}{r_0} \right) \right]^{-\frac{2}{\mu}} \quad (6.1)$$

where ρ_0 is uncompressed target density, c_0 is the bulk sound speed of the target material, and μ is material exponent dependent on target properties. They also found that the asymmetric pattern of peak stress occurs when the impact angle is as high as 45° ; peak stresses downrange are nearly twice those of uprange at the same distance, even in the far field from the impact point (Figure 7 in *Dahl and Schultz* [2001]). Their measurements confirm the numerical simulation of peak stresses beneath oblique impact craters by *Pierazzo and Melosh* [2000]. Asymmetric pattern of peak stress is observed even for 60° impact, and the peak shock pressure is along the projectile trajectory (Figure 3 in *Pierazzo and Melosh* [2000]). This asymmetric pattern of stress wave is a consequence of energy coupling between projectile and target during an oblique impact.

As stated previously, shock-induced damage and cracking are directly related to the peak pressure beneath impact craters. When P_r equals to the dynamic tensile strength of the target, P_c , tensile cracks would be produced. The stress wave asymmetry for oblique impacts, confirmed by both experimental measurement and numerical simulation, is expressed as asymmetric damage pattern in the recovered targets, as observed in this study for both granite and limestone.

The peak stresses downrange for oblique impacts decay roughly as $P \sim X^{-2}$ [*Dahl and Schultz*, 2001]. This means the exponent, μ , in Equation 6.1 is one for this situation. We can use the scaling relation in Equation 6.1 to get damage depth for oblique impacts from a vertical impact while keeping other conditions all the same. For a vertical impact into

San Marcos granite by the same projectile and impact velocity, the tensile cracks extend to a depth of $6 \sim 7$ cm, when the peak stress reaches ~ 0.13 GPa, the dynamic tensile strength of San Marcos granite. Using the scaling law in Equation 6.1, we calculate the tensile crack propagating distance from the impact point for oblique impact at 45° into San Marcos granite to be $4.3 \sim 5$ cm, or $3 \sim 3.5$ cm in depth. This result is in good agreement of our tomography inversion (Figure 6.4).

Knowing the dynamic tensile strengths for different materials, tensile crack propagating distance in different types of rocks can also be inferred from Equation 6.1 for similar impact conditions. Rearrange Equation 6.1 into:

$$P \sim \rho_0 V^2 \sin^2 \theta \left(\frac{r}{r_0} \right)^{-2} \quad (6.2)$$

Taking the dynamic tensile strength of Bedford limestone as 0.06 GPa [Ahrens and Rubin, 1993], the damage depth for the oblique impact at 45° into limestone by the same projectile at velocity of 1.16 km/s is scaled to be $4.3 \sim 5.1$ cm, using Equation 6.2 and damage depth information into granite at velocity of 1.2 km/s ($3 \sim 3.5$ cm). Again, this prediction agrees well with the direct measurement of the compressional wave velocity for the cubes (Figures 6.5, 6.6).

It should be noted that measurements in this study are carried out in the strength regime, when the effect of gravity is ignored. For kilometer size impact craters in the field, the result in this paper may not be applied directly, since gravity would play an important role then. Furthermore, late stage modification such as erosion and collapse, and center uplift for complex craters would make situations in the field more complicated. Hence, simulation

taking into account the gravity effect in larger scale is necessary and would be carried out in the future. However, the results from our experimental measurements are still very intriguing; it suggests that the shock-induced damage and cracking beneath craters might be a unique, while not being paid attention to and/or well understood constraint for projectile trajectory. This provides an important direction of future research for the impact cratering community.

6.4 Conclusion

The asymmetric patterns of the peak shock stresses suggested either by the direct laboratory measurement [*Dahl and Schultz, 2001*], or the numerical simulation [*Pierazzo and Melosh, 2000*], are represented as the shock-induced damage asymmetry. Two oblique impacts, with impact angle at 45° , are carried out in this study. Targets chosen are San Marcos granite and Bedford limestone respectively.

Cm-scale tomography technique is used for mapping the compressional wave velocity reduction in the recovered granite. For Bedford limestone, 1-cm cubes are cut from the recovered target and measured directly for the compressional wave velocities. Asymmetry of the low velocity zone is observed on the central plane containing the projectile trajectory, and the peak damage extends along the downrange direction from the impact point. Asymmetry is not observed for the plane across the projectile trajectory. The damage depth for granite is ~ 3 cm and ~ 4.5 cm for limestone.

Information of shock-induced damage and cracking below impact craters is an important constraint for impact history. Combined with other known parameters such as crater

dimension, projectile and target properties, damage and cracking could provide useful yet unrecognized constraint on the impact history.

Chapter 7

Numerical Modelling of Shock-Induced Damage for Granite under Dynamic Loading

7.1 Introduction

Although experimental parameters such as impact velocity, projectile and target materials, impactor orientation, can be varied over a wide range in the laboratory, the full range of parameters of interest, especially for the large, gravity controlled craters in the solar system, cannot be reached experimentally. Furthermore, the response of rock to effect of gravity on strength during the formation of large craters affects the transition from the strength controlled to gravity controlled regime.

Numerical modeling of impact cratering requires detailed constitutive models for rocks. The behavior of rocks under various conditions of stress can be complicated. Strength of rocks is usually a function of pressure, temperature, strain, strain rate, sample size, and damage [Lockner, 1995]. Various models have been used for cratering calculation, including the hydrodynamic, elastic, Von Mises (constant shear strength), the Mohr-Coulomb model (increasing shear strength with hydrostatic pressure), the Johnson-Cook model, etc.

However, a complete and appropriate description of the constitutive model that takes into account post-failure deformation and damage response of rocks is still not available. Although treatment of rocks by *O'Keefe et al.* [2001] and *Collins et al.* [2004] does include the influence of pressure, strain, and damage to strength, the elastic moduli derived have not been compared, in details, with post-impact elastic models. Moreover, the final damage field calculated from the numerical simulation was not compared with craters. We expect that when detailed comparisons of calculations to experiments are conducted, additional constraints on rock constitutive parameters are expected to be obtainable.

We apply JH-2 model, which was originally developed by *Johnson and Holmquist* [1999] for ceramics, to geological crustal rocks for the first time. In the next session we will overview AUTODYN, the package used for simulation in this work [AUT, 2003]. Then a brief description of the JH-2 strength model coupled with the cracking softening model is given. We explain in detail how to determine proper JH-2 model parameters for granite from experimental data in the literature. Finally we present the results of our simulation for the damage that occurs beneath and surrounding impact craters in crustal rocks. We compare them with experimental data. The experiments are a continuation of previous efforts oriented toward quantification of shock-induced seismic velocity deficits by *Xia and Ahrens* [2001] and *Ai and Ahrens* [2004].

7.2 Related work

7.2.1 An overview of AUTODYN

AUTODYN is a finite difference/element hydrocode designed for non-linear dynamics problems. It has been under continuous development since 1985 by Century Dynamics Inc. The software uses classical continuum mechanics to describe the dynamic motion of materials through finite difference/element approximation to the conservation of mass, momentum and energy, and constitutive equations relating stress, strain, strain rate and appropriate failure criteria [AUT, 2003]. This software employs eight numerical solvers, based on Lagrangian and Eulerian algorithm, as well as a very wide range of material models coupled with extensive range of failure models. AUTODYN is widely used to simulate the effect on military and civil structures to dynamic loading. It is also proved to be a powerful tool for replicating planetary impact events [*Baldwin et al.*, 2005].

Lagrangian codes use grid points attached to the material to define unambiguously the material interfaces and the shock front. For large material deformations, the grid deforms severely and is subjected to tangling problems. This hinders application of the Lagrangian codes to hypervelocity impact calculation. In contrast, Eulerian codes do not have this tangling problem, since they use spatially fixed grids. But Eulerian codes have difficulty in following accurately boundaries between materials, and the stress history and development of cracks. Furthermore, Eulerian codes require more computational resources than do Lagrangian codes for similar problems. Both methods are not that well suited to conduct simulation of deformation and damage in materials.

The Smoothed Particle Hydrodynamics (SPH) method is a meshfree Lagrangian type solver which defines geometry as well as the hydrodynamic quantities as particles moving with the flow and interacting with each other [Monaghan, 1992; Benz and Asphaug, 1995]. Since there is no fixed connectivity in SPH, it provides a highly useful alternative to, and is a great improvement over traditional grid-based finite-difference methods, especially for describing shear and tensile crack propagation. SPH methods were developed three decades ago [Lucy, 1977]. Since then, many improvements have been made and it has been extended to solve a wide variety of hypervelocity impact problems that include the effect of material strength [e.g. Benz and Asphaug, 1995; Bate and Burkert, 1997].

7.2.2 Description of brittle material model

7.2.2.1 JH-2 model

The JH-2 model is proposed by *Johnson and Holmquist* [1999] to describe the brittle response of ceramics. The model is summarized in Figure 7.1. Shock compression, hydrodynamic response of the material before fracture is represented by a polynomial equation of state:

$$P = K_1\mu + K_2\mu^2 + K_3\mu^3 \quad (7.1)$$

where P is pressure, K_1 , K_2 , and K_3 are constants (K_1 is the bulk modulus), and $\mu = \rho/\rho_0 - 1$ for current density ρ and initial density ρ_0 . Strength of material, both intact and fractured, is dependent on pressure, strain rate, and damage. The intact strength σ_i^* , which

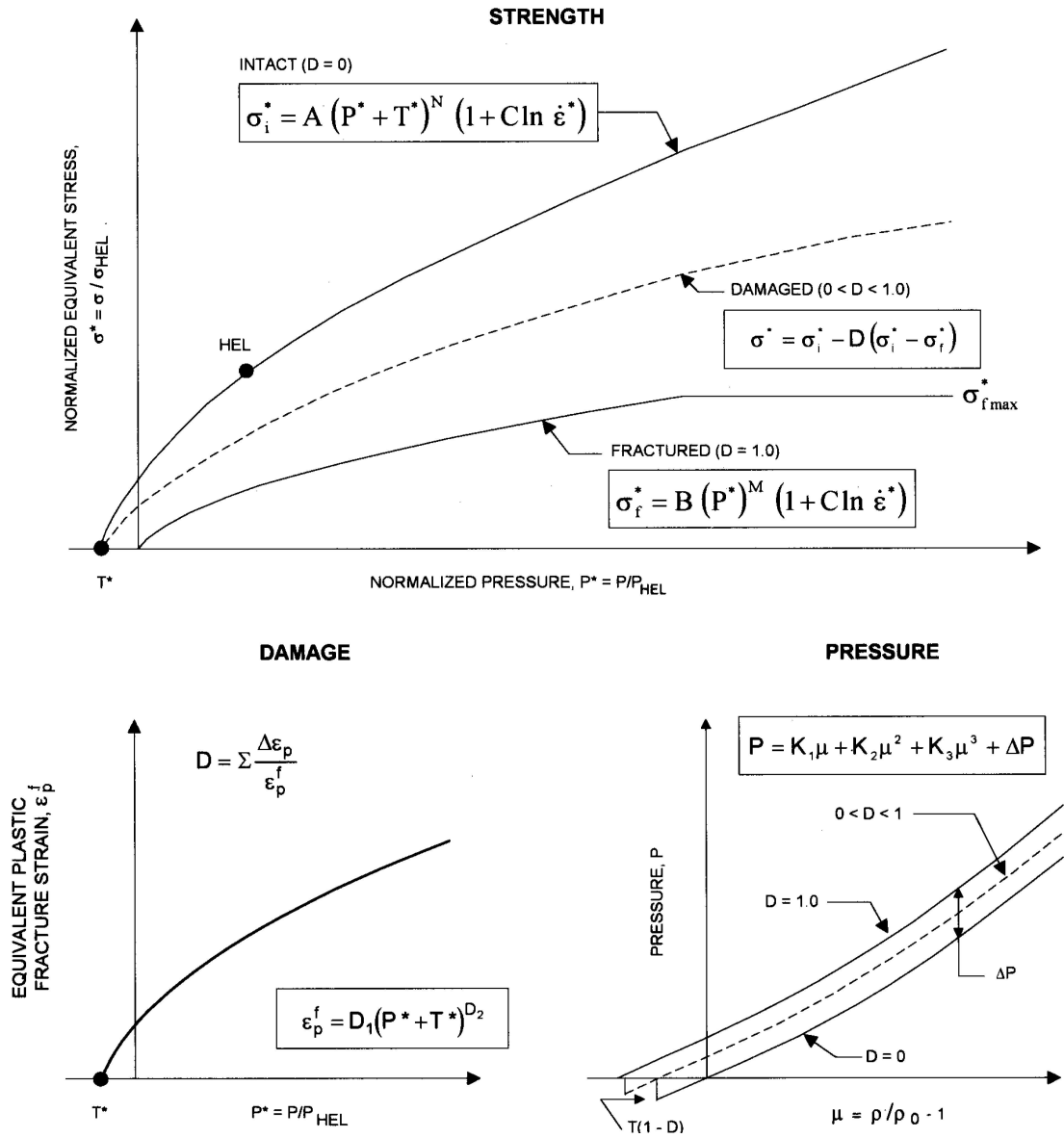


Figure 7.1: Description of JH2 model for brittle materials (from Johnson and Holmquist [1999], Figure 1).

is normalized by σ_{HEL} , the equivalent stress at Hugoniot elastic limit (HEL), is given by:

$$\sigma_i^* = A(P^* + T^*)^N(1 + C \ln \dot{\varepsilon}^*) \quad (7.2)$$

The normalized fracture strength σ_f^* is:

$$\sigma_f^* = B(P^*)^M(1 + C \ln \dot{\varepsilon}^*) \quad (7.3)$$

where $P^* = P/P_{HEL}$, T^* is the normalized maximum tensile hydrostatic pressure. The actual strain rate, $\dot{\varepsilon}$, is normalized by the reference strain rate, $\dot{\varepsilon}_0$, taken as 1.0 s^{-1} . An upper limit is applied to the fractured strength, given by σ_{fmax}^* . In other words, $\sigma_f^* \leq \sigma_{fmax}^*$.

The transition from intact to fractured strength is achieved through a damage parameter:

$$\sigma^* = \sigma_i^* - D(\sigma_i^* - \sigma_f^*) \quad (7.4)$$

D is the damage ($1 \geq D \geq 0$), defined as integrated plastic strain:

$$D = \sum \Delta \varepsilon_p / \varepsilon_p^f \quad (7.5)$$

$\Delta \varepsilon_p$ is the equivalent plastic strain during a cycle of integration and ε_p^f is the plastic strain to fracture under a constant pressure P , given as:

$$\varepsilon_p^f = D_1(P^* + T^*)^{D_2} \quad (7.6)$$

Under a constant pressure, damage begins to accumulate when the material begins to flow plastically ($D=0$). When the material is completely damaged, $D=1$. Figure 7.2 shows the definition of damage due to accumulated effective plastic strain. Equations 4.7 and 7.5 describe damage from different aspects. We take Equation 4.7 as the physical expression of accumulated effective plastic strain in Equation 7.5.

For equations 7.1-7.6, K_1 , K_2 , K_3 , A , B , C , M , N , T , $\sigma_{f_{max}}^*$, D_1 and D_2 are material constants either to be derived from quasi static measurements, or to be numerically adjusted [Johnson and Holmquist, 1999]. A detailed description of the determination of parameters for granite is given below.

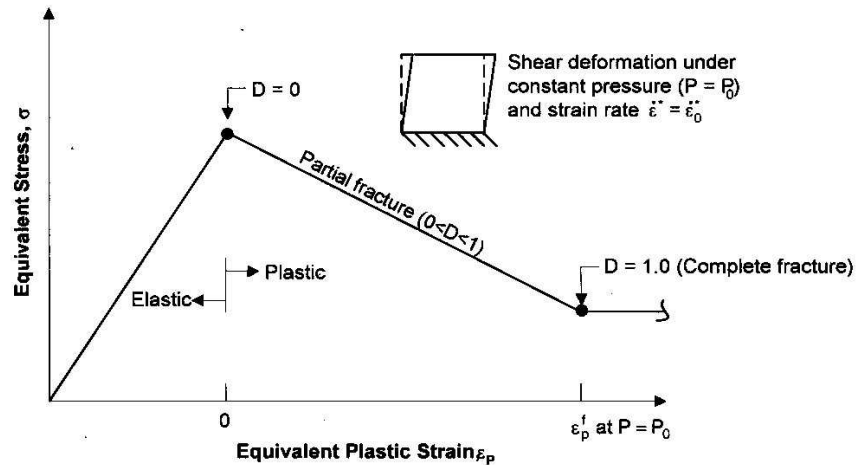


Figure 7.2: Strength, damage, and fracture under a constant pressure and strain rate for the JH2 model (from Johnson and Holmquist [1999], Figure 2).

7.2.2.2 Tensile crack softening model

The total damage for an impact event includes both shear and tensile cracks [Collins et al., 2004]. The JH-2 brittle model is appropriate for simulating the inelastic shear cracking which occurs in the high compressive region ahead of the projectile. In the far field where

tensile stress plays an important role as well, the damage is induced by the propagation of tensile crack in the material. The tensile crack softening model described in *Clegg and Hayhurst* [1999] is coupled with the JH-2 model to simulate both shear and tensile failure. The crack softening model simulates the gradual reduction of load carrying capacity of brittle materials during the late stage when the magnitude of principal tensile stress is in the same order of shear stress. In AUTODYN, the cracking softening model is implemented this way: On failure initiation, the current maximum principal tensile stress in the cell is stored. Then a linear softening slope is used to define the maximum possible principal tensile stress in the material as a function of crack strain. This softening slope is a function of the local cell size and the fracture energy (the energy needed to create a unit fracture surface) of the material, G_f . The fracture energy is related to the fracture toughness through $G_f = K_2/E$, where K is the fracture toughness, and E is the elastic modulus [AUT, 2003].

7.3 Determination of model constants for granite

A summary of the constants of JH-2 model for granite is listed in Table 7.1. Density is from the volume and mass measurement. The elastic constants are calculated from the measured compressional and shear velocity. The following will discuss how to determine the constants for pressure, strength of both intact and fractured material, and damage.

7.3.1 Pressure

Figure 7.3 shows the axial stress, σ_1 , and the mean stress/pressure, P , as a function of the volumetric strain μ during uniaxial strain loading for Westerly granite [*Brace and Riley*,

Table 7.1: JH2 baseline and crack softening constants for granite

Density	$\rho_0 = 2657 \text{ kg/m}^3$
Elastic constants	
Modulus of elasticity	$E = 80 \text{ GPa}$
Poisson's ratio	$\nu = 0.29$
Bulk modulus	$K_1 = 55.6 \text{ GPa}$
Shear modulus	$G = 30 \text{ GPa}$
Strength constants	
Hugoniot elastic limit (HEL)	$\text{HEL} = 4.5 \text{ GPa}$
HEL strength	$\sigma_{HEL} = 2.66 \text{ GPa}$
HEL pressure	$P_{HEL} = 2.73 \text{ GPa}$
HEL volumetric strain	$\mu_{HEL} = 0.045$
Tensile strength	$T = 0.15 \text{ GPa}$
Normalized tensile strength	$T^* = 0.055$
Intact strength coefficient	$A = 1.01$
Intact strength exponent	$N = 0.83$
Strain rate coefficient	$C = 0.005$
Fracture strength coefficient	$B = 0.68$
Fracture strength exponent	$M = 0.83$
Maximum fracture strength	$\sigma_{fmax}^* = 0.2$
Pressure constants	
Bulk modulus	$K_1 = 55.6 \text{ GPa}$
Pressure coefficient	$K_2 = -23 \text{ GPa}$
Pressure coefficient	$K_3 = 2980 \text{ GPa}$
Bulk factor	$\beta = 1.0$
Pressure constants	
Damage coefficient	$D_1 = 0.005 \text{ GPa}$
Damage coefficient	$D_2 = 0.7 \text{ GPa}$
Cracking softening constants	
Tensile failure stress	$T_f = 0.15 \text{ GPa}$
Fracture energy	$G_f = 70 \text{ J/m}^2$

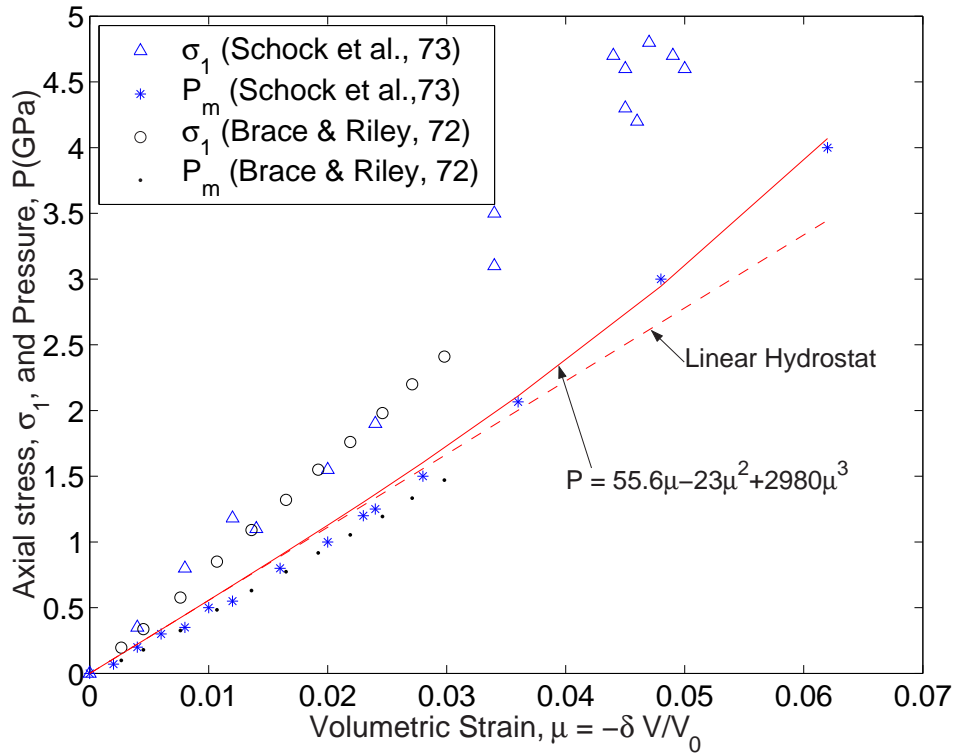


Figure 7.3: Test data and model for shock pressure-volume response of granite.

1972] and for Climax stock granodiorite [Schock *et al.*, 1973]. The two sets of data are in very good agreement. The difference between the axial stress and the pressure is an indication of the strength of the material. The linear hydrostat is also shown to provide a reference. Pressure constants K_1 , K_2 , K_3 are obtained by fitting P to μ using Equation 7.1.

Bulking or dilatancy, which is expressed as volume increase or density decrease, is noticed when brittle materials fail [Brace *et al.*, 1966]. However, a quantitative description of bulking for granite is difficult to obtain and as dilatancy decreases at high strain rates [Brace *et al.*, 1966], it has been neglected in the present calculations.

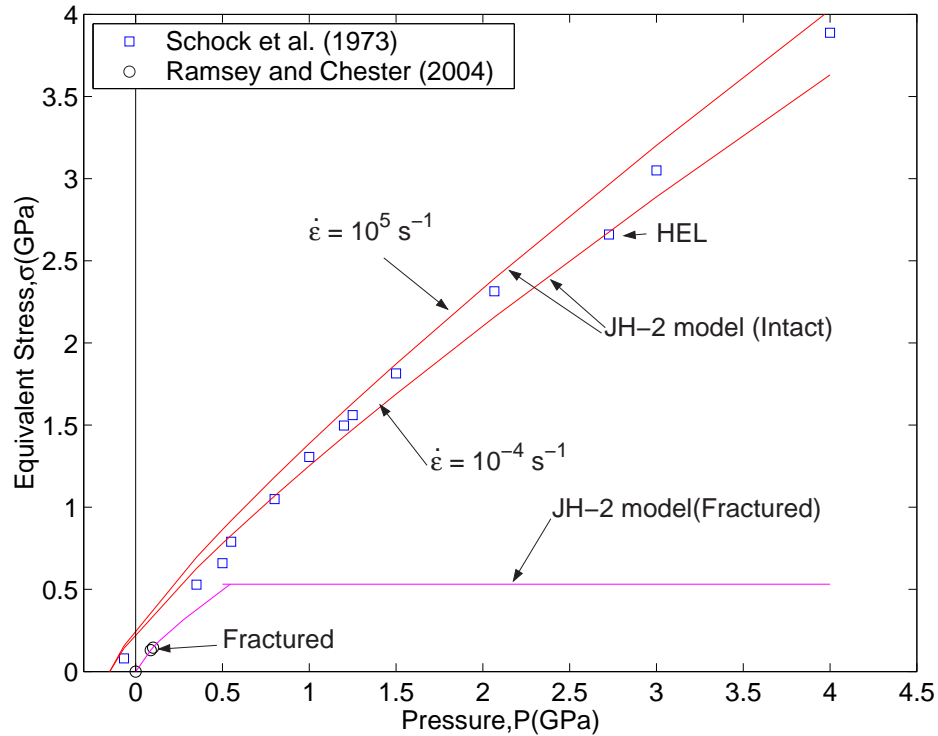


Figure 7.4: Test data and model for strength of intact and damaged granite.

7.3.2 Strength

The HEL is taken as 4.5 GPa, the average value from [Petersen, 1969]. This includes both the deviatoric stress and the hydrostatic pressure components. To determine the strength and pressure components, we follow the method described in Johnson and Holmquist [1999]. The HEL volumetric strain is solved from HEL , K_1 , K_2 , K_3 , and G as $\mu_{HEL} = 0.045$. Substitute μ_{HEL} into Equation 7.1 gives pressure at HEL of $P_{HEL} = 2.73$ GPa. The equivalent stress, defined as twice of the material shear strength, at HEL is 2.66 GPa (σ_{HEL}). The intact equivalent stress of the material as a function of pressure, from data in Figure 7.3, is shown in Figure 7.4. Also shown is the calculated value from JH-2 model using constants in Table 7.1 at two strain rates, 10^5 s^{-1} and 10^{-4} s^{-1} . It seems that the effect of strain rate is rather small. The strain rate coefficient, C , is assumed to be 0.005, taken as

the same as ceramic [Johnson and Holmquist, 1999]. Fortunately, as noted previously, this constant does not influence the result greatly.

Planar impact experiments as well as ultrasonic velocity measurements of samples before and after impact, described in Chapter 2, were used to determine the dynamic tensile strength of San Marcos granite. The targets are shaped as discs with diameters of 23 mm and thickness of 6-7 mm. A Lexan projectile carrying aluminum (Al 2024) flyer plate at its front, with the thickness of flyer plate ~ 3 mm, is accelerated by the expansion of pre-compressed air to velocities in the 13 to 30 m/s range. The peak shock pressure is calculated using impedance match method described in Ahrens [1987]. We assume the magnitude of the tensile stress is equal to that of the original compressive stress. Impact velocities, the calculated tensile stress, as well as the compressional wave velocity measurements of samples before and after impact for a few typical shots are listed in Table 7.2. The dynamic tensile strength is determined to be the tensile stress at which tensile cracks start to occur, detected as compressional wave velocity reduction in the samples. The ultrasonic velocity reduction is observed at tensile stress between 0.12 and 0.14 GPa. We determine the dynamic tensile strength of granite is 0.13 GPa.

For tensile pressure, P is given as $P = K_1 \mu$ [Johnson and Holmquist, 1999]. Similar procedure gives $P_{tensile} = -0.067$ GPa and $\sigma_{tensile} = 0.08$ GPa (Figure 7.4). Extrapolating this to $\sigma=0$ gives tensile strength GPa. This is greater than 0.1 GPa, the value used in Collins *et al.* [2004]. The normalized tensile strength is $T^* = T/P_{HEL} = 0.055$. Intact strength constants A and N are obtained by nonlinear fitting of the experimental data using Equation 7.2.

Table 7.2: One-dimensional impact parameters, as well as pre- and post-shot compressional wave velocities for Al2024 flyer plate into San Marcos granite.

Shot	Projectile Velocity m/s	Tensile Stress MPa	Pre-shot	Postshot	ΔV_p	Comments
			V_p , km/s	V_p , km/s		
Ga11	13.5	120.8	6.45	6.45	0%	No visible cracks
Ga7	15.6	140	6.5	5.65	13%	Incipient cracks; few well developed shorter cracks
Ga1	20	172	6.6	5.56	15.7%	Incipient cracks; fairly well-developed cracks; relatively long spall cracks
Ga3	30	271	6.64	–	–	Fragmented, not measurable

No proper fractured strength data for granite are found. Instead, some fractured data for marble are used for this purpose [Ramsey and Chester, 2004]. Triaxial extension experiments are carried out on Carrara marble to study fracture mechanism in their work. We fit the data available to Equation 7.3 to obtain the fracture strength constants, B and M .

More experiments for fracture strength of granite are necessary to obtain a better constrain of these fractured strength parameters. The normalized fractured strength is limited not to exceed the maximum fractured strength, σ_{fmax}^* , taken as 0.2 here, or 0.53 GPa as the equivalent stress.

7.3.3 Damage

Damage (D) describes the transition from intact to fractured strength. Under a constant pressure, damage begins to accumulate when the material begins to flow plastically ($D = 0$). When the material is completely damaged, $D = 1$. The damage parameters D_1 and D_2 used by Johnson and Holmquist [1999] are not directly measurable. Instead, numerical adjustment is applied to obtain D_1 and D_2 listed in Table 7.1.

7.3.4 Tensile cracking softening

The maximum principal tensile stress for the tensile softening model is 0.15 GPa, as noted above. The associated fracture energy is assumed to be 70 J/m^2 , which is the value obtained for ceramics [Clegg and Hayhurst, 1999].

7.4 Examples

Using the JH-2 model parameters for San Marcos granite determined above, several calculations are performed using finite element/difference package AUTODYN 2D to simulate impacts with different combinations of projectile and impact velocity. Planar impact of Al into mm scale San Marcos granite discs as well as impact into 20x20x15 cm granite block by commercial lead bullet and copper ball are simulated. The impact velocities range from 13 m/s to 1200 m/s. Parameters for projectiles are retrieved from AUTODYN library [AUT, 2003]. The results are presented below and compared with experimental results.

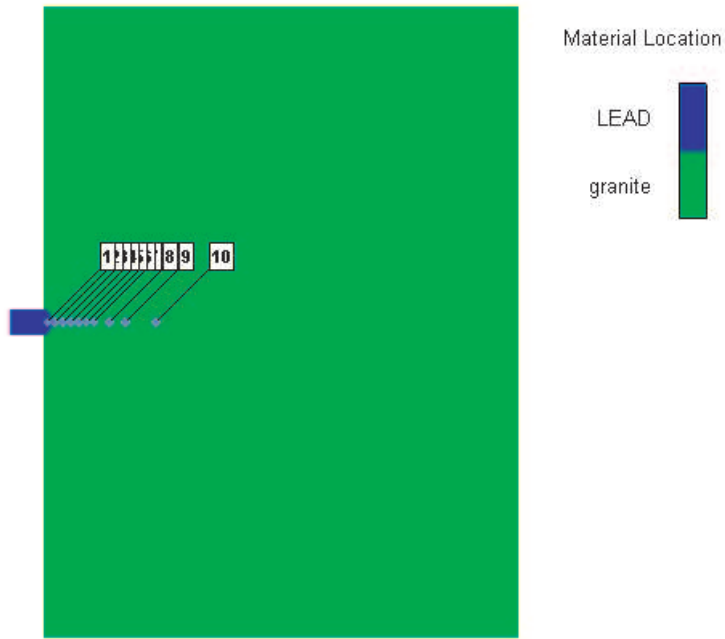
7.4.1 Lead bullet impacting granite

Simulation of shot 117, a 3.2 g lead bullet impacting a 20x20x15 cm granite block at 1200 m/s vertically is carried out and compared with our experimental result. Radius of the projectile is 3 mm. Figure 7.5a shows the initial setup of the simulation, as well as the locations of the gauges points used. The geometry of the problem setup and the response of target are assumed to be axisymmetric. The meshfree Smoothed Particle Hydrodynamics (SPH) solver [Lucy, 1977; Benz and Asphaug, 1995] is used for the projectile and rock

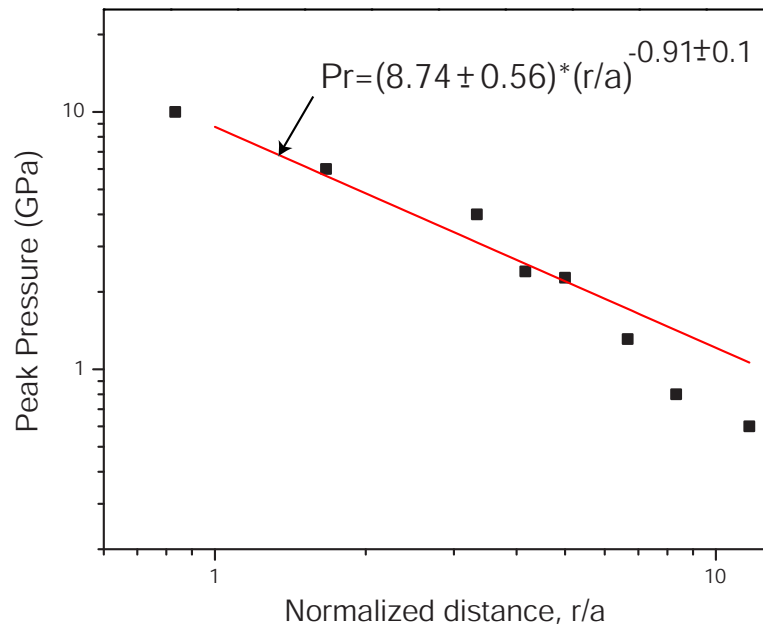
target, with smoothing particle size to be 0.125 mm for the projectile and 0.25 mm for the rock target. Figure 7.5b plots the peak shock pressure of the gauge points versus the normalized distance from impact. Exponential fit of the data gives the initial pressure, P_0 , as 8.74 ± 0.56 GPa, which is close to the analytical calculation, 10.3 GPa. The attenuation coefficient, n is 0.91 ± 0.1 , and this is lower than the predicted value, 1.3 (Chapter 3).

Figure 7.6 illustrates the damage accumulation with time for our simulation. During the early stage of formation of the impact crater, shear damage caused by shear stress is dominant near the region around the projectile (Figure 7.6a, b). During the later stage, failure mechanism changes to principal tensile stress and finger-like tensile cracks began to grow by the tensile strain localization during expansion of the shock wave (Figure 7.6c). Finally, large tensile cracks are formed and propagate further into the rock target (Figure 7.6d). The excess damage along the centerline in Figure 7.6d is believed to be caused by the numerical artifact, which is a very common problem for numerical simulation.

The simulated final damage profile is chosen at the time when no more obvious damage is produced, and the result is compared with the experimental result. For convenience, cross section showing different types of cracks and damage depth is shown again (Figure 7.7a). Asymmetry of cracking pattern in experiment is caused by the heterogeneity of the rock target. The calculated crater depth is ~ 1.5 cm, and crater diameter is ~ 7 cm (Figure 7.7b), both of which agree well with the experiment. The prediction of radial tensile cracks with the experimental result is encouraging: shape and depth of tensile cracks for both situations are very similar. The tensile cracks extend to 6-7 cm for both cases.



(a)



(b)

Figure 7.5: (a) Initial setup for simulating shot 117, lead bullet into 20x20x15 cm granite block at velocity of 1.2 km/s, and location of gauge points; (b) Peak pressure of gauges versus normalized distance from impact. r is distance, a is radius of projectile. Red line is exponential fit of data.

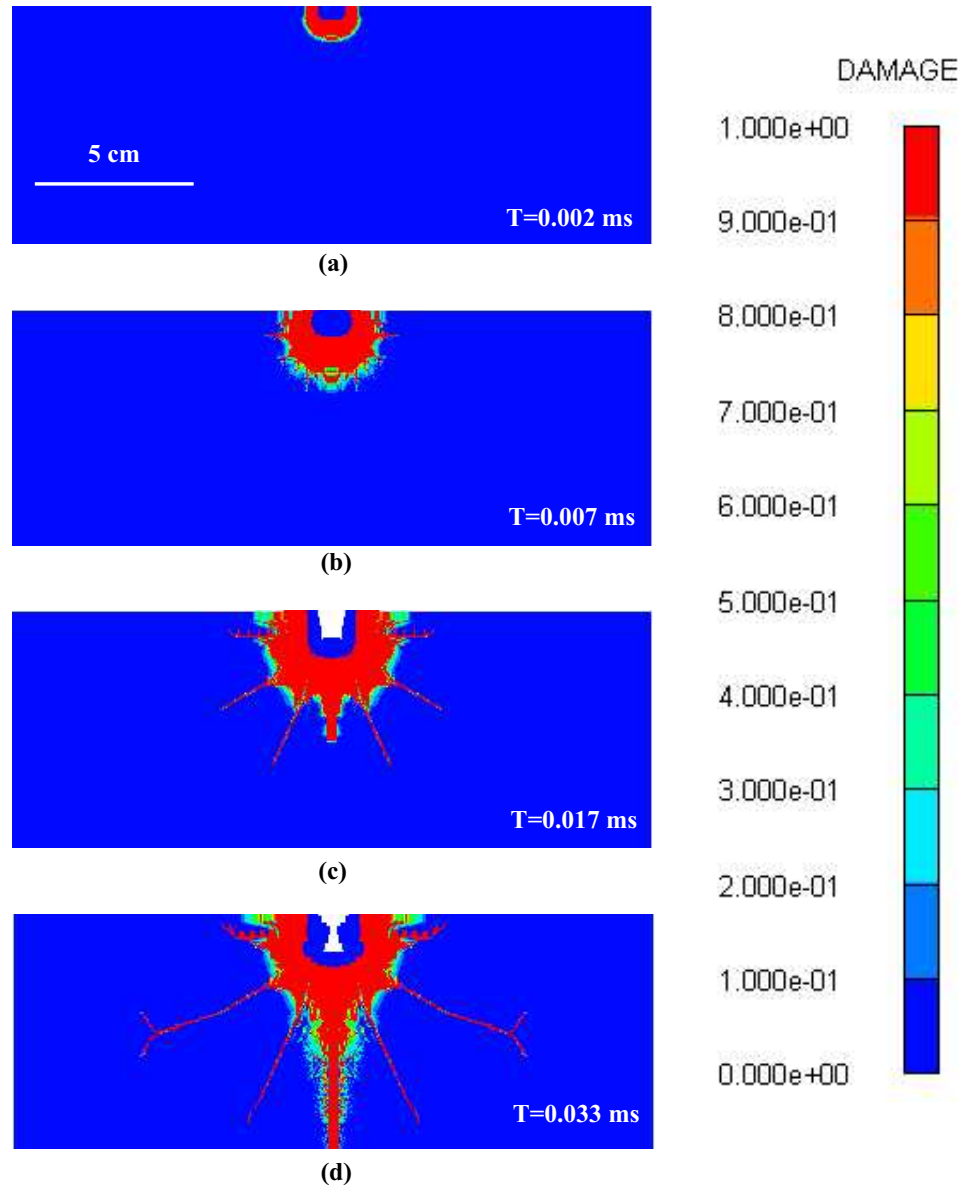


Figure 7.6: Simulated damage contour for shot 117 at several times during impact event. (a) and (b): During early stage of impact, damage caused by shear stress dominated high pressure region around projectile; (c) finger-like tensile cracks begin to form due to tensile strain localization; (d) final profile showing the propagation of tensile cracks.

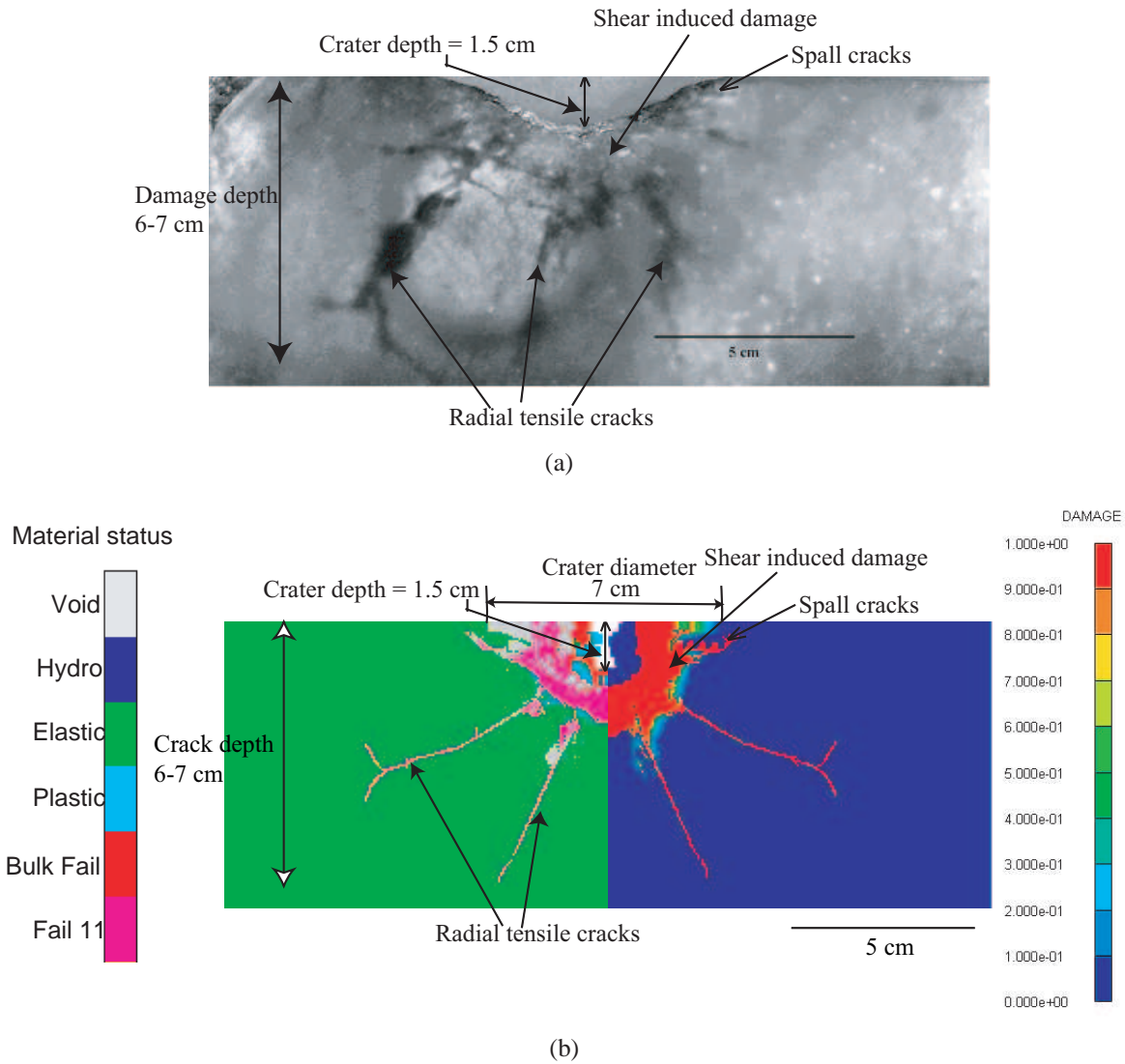


Figure 7.7: Cross section of granite impacted by lead bullet at 1200 m/s illustrating crack distribution. Normal impact. (a) Experimental result; (b) AUTODYN-2D simulation at 0.03 ms. Left panel illustrates material status; right panel illustrates damage.

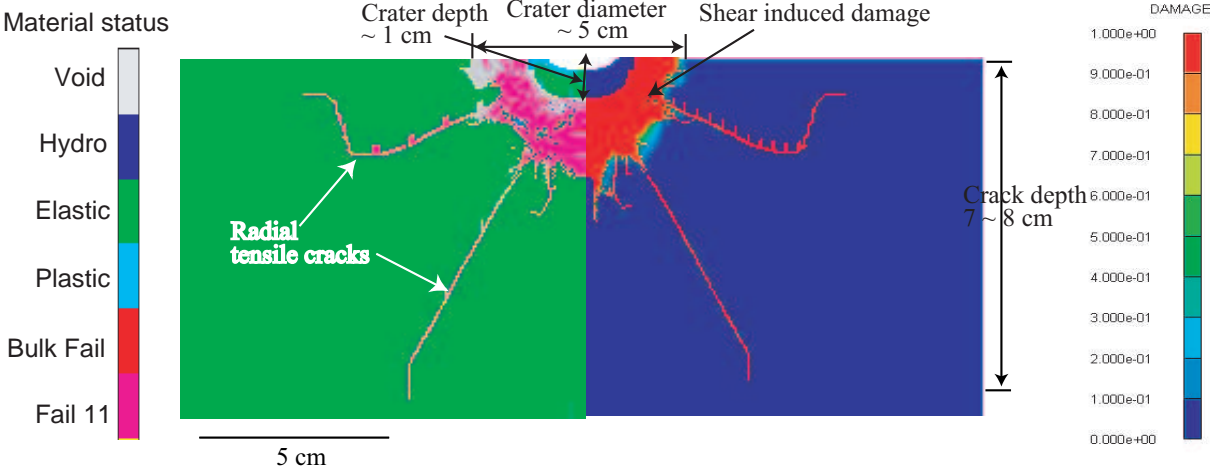
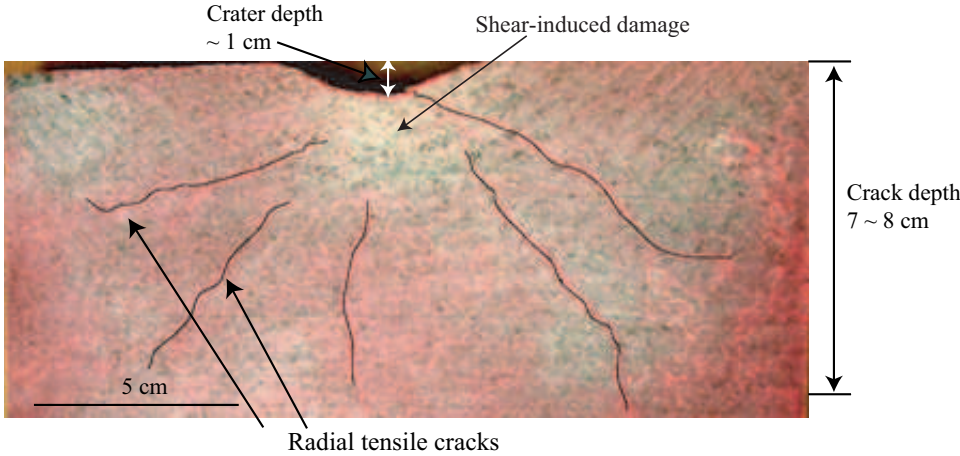


Figure 7.8: Cross section of granite impacted by copper ball at 690 m/s. Normal impact. (a) experimental result; (b) simulation at 0.04 ms. Others are the same as in Figure 7.7b.

7.4.2 Copper ball impacting granite

Shot 1194, impact of a copper ball (0.64 cm in radius) into a 20x20x15 cm San Marcos granite block at velocity of 690 m/s is simulated. Except for the impact velocity and projectile material, the simulation setup is the same as that for Shot 117. Figure 7.8 shows the comparison between the experiment and simulated result. Again, the agreement concerning the crater depth, number of radial tensile cracks as well as the crack shape and depth between these two is very good. Crater depth is ~ 1 cm, crater diameter is ~ 5 cm (Figure 7.8a, b), and tensile crack depth extends to ~ 8 cm.

7.4.3 Plate impact of Al flyer plate into granite

The four planar impacts of Al flyer plate into granite discs, listed in Table 7.2, are simulated. Lagrangian solver is used for both the flyer plate and rock target, with uniform cell size of 0.1 mm. What we measured in experiments is the ultrasonic wave velocity reduction perpendicular to the impact surface for these samples. The ultrasonic wave velocities are indirect measurements of damage.

For a fractured body, the ultrasonic velocity reduction would be high compared with that with few or no cracks. For our one dimensional planar impacts, cracks produced are mainly oriented parallel with the impact surface. These cracks would reduce ultrasonic wave velocities measured in the direction perpendicular to the crack orientation [Anderson *et al.*, 1974]. As will be discussed below, the simulated damage for the four shots correlates qualitatively well with the ultrasonic wave velocity measurements and the observations of cracks within the covered samples.

Figure 7.9 shows the different degrees of damage for the four impacts. Here $D = 0$ means intact, and $D = 1$ means fully fragmented. Crack is not observed for the lowest velocity impact, $U = 13.5$ m/s (Figure 7.9a). No velocity reduction is observed from measurements (Table 7.2). With the increase of impact velocity, tensile cracks are developed. The number of cracks increases with the impact velocity. For the weak-moderate impact with impact velocity of $U = 15.6$ m/s, only incipient and few well-developed shorter cracks are observed (Figure 7.9b). Long spall crack is seen for the moderate impact with impact velocity of $U = 20$ m/s (Figure 7.9c). The samples still remain contact for both cases ($D < 0.5$). Compressional wave velocity reduction also increases with the impact velocities (Table 7.2). When the impact velocity is as high as 30 m/s, severe damage ($D > 0.8$) is reached along the spall plane within the sample (Figure 7.9d). The sample is not measurable for ultrasonic wave velocities at this stage.

7.4.4 Oblique impact

An oblique impact into a 20x20x15 cm granite, with impact angle at 45° , is simulated using AUTODYN-3D. The projectile is the same as that in Section 7.4.2, and the impact velocity is 1000 m/s. Figure 7.10 shows the cross section of the recovered target after being cut open, while Figure 7.11 presents the calculated result for this shot. Asymmetry is observed on both figures. The pattern of damage and tensile cracks in Figure 7.11 is in good agreement with the directly measured one (Figure 7.10).

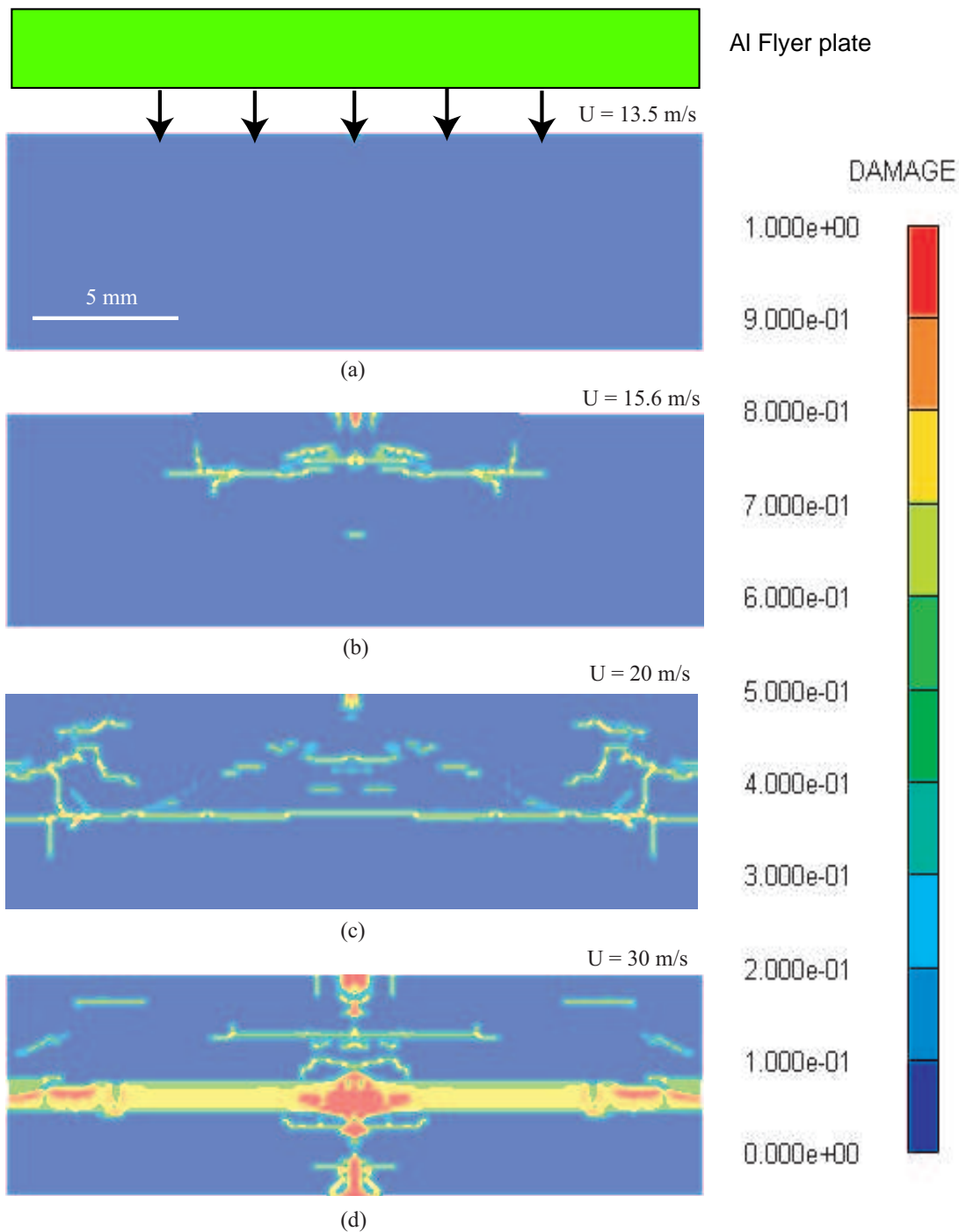


Figure 7.9: Simulated damage for plate impact of Aluminum flyer plate into San Marcos granite at different velocities. Flyer plate shown in green, is $\sim 3 \text{ mm}$ in thickness. (a) $U = 13.5 \text{ m/s}$. No visible cracks observed; (b) $U = 15.6 \text{ m/s}$. Incipient cracks as well as few well-developed shorter cracks observed. (c) $U = 20 \text{ m/s}$. Except cracks observed in (b), relatively long spall cracks observed. (d) $U = 30 \text{ m/s}$. Sample fragmented, ultrasonic wave velocity not measurable.

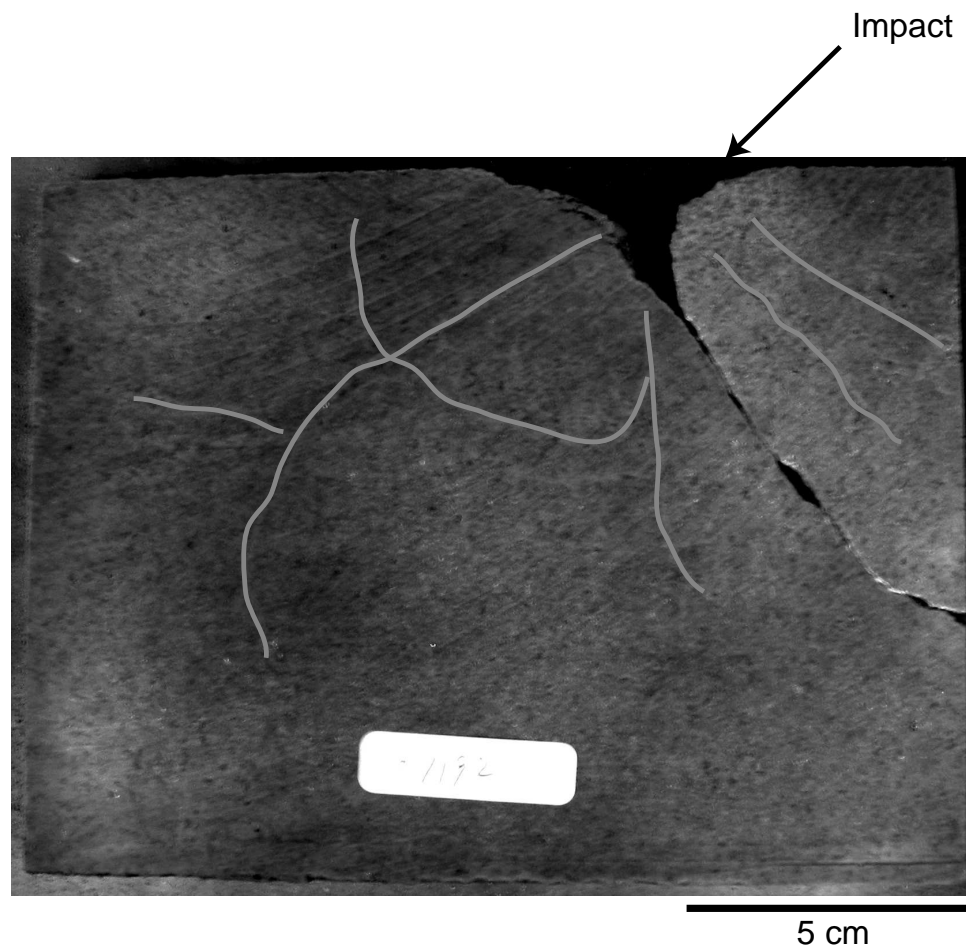


Figure 7.10: Cross section of granite impacted by copper ball at 1000 m/s, experimental result. *Vector* shows impact angle at 45° . Visible tensile cracks are highlighted.

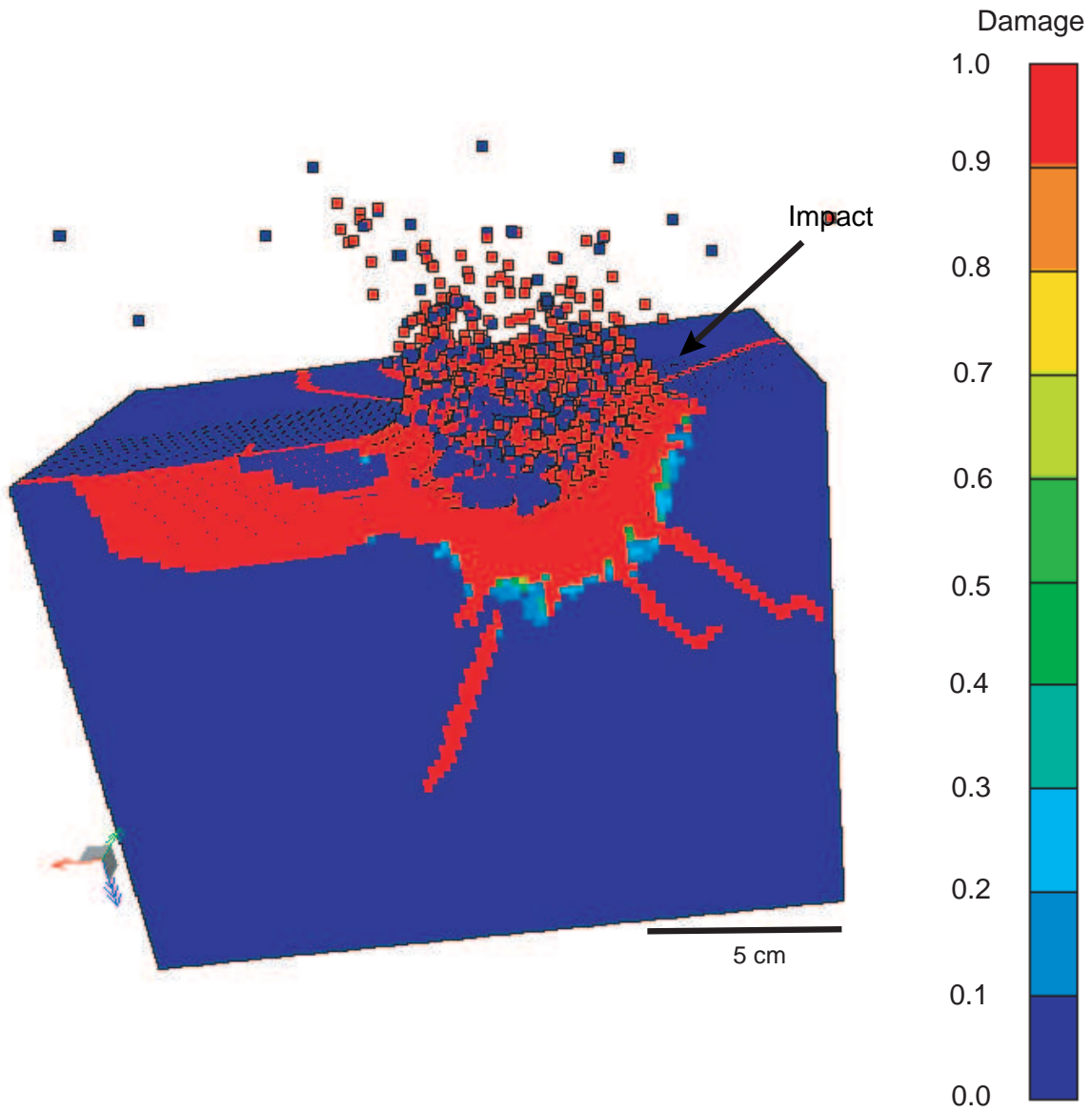


Figure 7.11: Simulated result at 0.1 ms for shot shown in Figure 7.10.

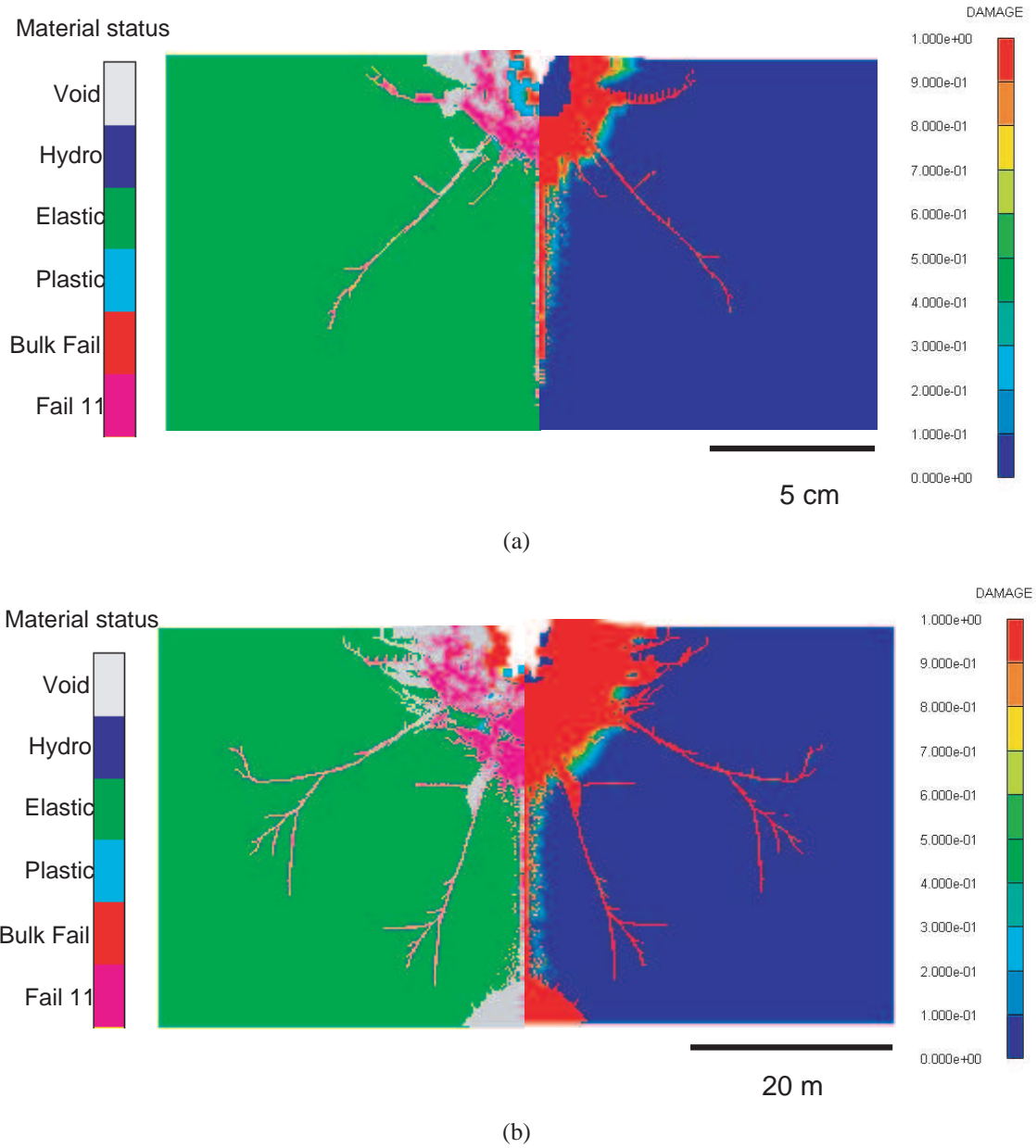


Figure 7.12: Simulated result shown effect of gravity on formation of tensile cracks. Normal impact. (a) 500 g, $a_p=3$ mm; (b) 1 g, $a_p=1500$ mm. Left panel illustrates material status, right panel for damage status. Notice different scales on the two plots. See text for discussion.

7.4.5 Effect of gravity on damage and cracks

Large craters formed in a planetary gravity field can be simulated by much smaller projectiles at elevated gravity using a geotechnical centrifuge, on the condition that similarity between the two cases is satisfied [Schmidt and Housen, 1987]. The similarity means that the product of G and a should be constant for two impacts, where G is the planetary gravity, and a is the projectile radius. Therefore, a large impact with $G=1g$, where g is the gravitational constant, and $a=1.5$ m should be similar with a small scale impact with $G=500g$, $a=3$ mm, keeping other impact conditions the same.

The effect of gravity on propagation of cracks is also investigated numerically. The two impacts mentioned above are simulated using the JH2 model parameters for granite. The dimension of target is scaled accordingly. For both cases, projectile is lead and impact velocity is 1200 m/s. Figure 7.12 compares the damage profiles at the final stage. Figure 7.12a has less tensile cracks than Figure 7.12b, especially in the deep region, no obvious tensile cracks are observed in Figure 7.12a. This phenomenon indicates that existence of high gravity prevents the propagation of cracks. This can be explained by the relatively large hydrostatic pressure in the deep depth, which has a negative effect on the propagation of tensile cracks.

7.5 Conclusion

This work is intended to provide a preliminary quantitative description of response of geological material to impact loading. The JH-2 constitutive model to describe mechanical character of brittle material is applied to granite for the first time and is coupled with a ten-

sile crack softening model to simulate impacts with different combinations of projectiles and impact velocities. The strength, pressure and damage characteristics determined either from direct experimental data, or from indirect numerical calibration, appears to predict the extent of damage and tensile crack propagation into the rock target to an encouraging degree. Uncertainties remain regarding the determination of model constants of fracture strength and energy, indicating that more detailed experimental data of fracture strength of shock damaged granites are needed.

Chapter 8

Future Work

The previous chapters describe systemically our preliminary study of shock-induced damage in rocks and the application to impact cratering. However, there is a very rich field and a lot of aspects are still to be explored.

Only two types of rocks are used in this study to obtain the scaling relation. Other typical terrestrial and planetary rocks, such as sandstone, ice, etc, should be included to have a full coverage of geological materials. Furthermore, multi layer targets, instead of one single target, should be used to represent the real geological conditions. If possible, the dimension of both target and projectile should be varied within a much larger range. More oblique impacts should be carried out, since it is a very interesting field itself and the result might be very intriguing.

The ultrasonic tomography inversion for the low porosity granite is a big improvement over the traditional dicing method. But still there is uncertainty with this method and it is not the most efficient way. In the future, other new method (such as CT inversion) is suggested to be tried and compared with previous results. The very important yet most difficult part is to carry out seismic exploration in the field and to build a database of damage depth for impact craters.

It is also true that a lot of questions are left unexplored in the field of simulation. For example, different strength models should be tested and compared for San Marcos granite and more static mechanical experiments be carried out to reduce the error of the determined model parameters. Simulation for other geological materials should also be initiated.

Bibliography

(2003), Autodyn theory manual, *Century Dynamics Inc.*

Ackermann, H. D., R. H. Godson, and J. S. Watkins (1975), A seismic refraction technique used for subsurface investigations at meteor crater, arizona, *J. Geophys. Res.*, 80, 765–775.

Ahrens, T., and J. O’Keefe (1987), Impact on the earth, ocean, and atmosphere, *Int. J. Impact Eng.*, 5, 13–32.

Ahrens, T. J. (1987), Shock wave techniques for geophysics and planetary physics, in *Methods of experimental physics*, edited by C. G. Sammis and T. L. Henyey, pp. 185–235, Academic Press, San Diego.

Ahrens, T. J., and J. V. G. Gregson (1964), Shock compression of crustal rocks; data for quartz, calcite and plagioclase rocks, *J. Geophys. Res.*, 69, 4839–4874.

Ahrens, T. J., and A. M. Rubin (1993), Impact-induced tensional failure in rock, *J. Geophys. Res.*, 98, 1185–1203.

Ai, H. A., and T. J. Ahrens (2004), Dynamic tensile strength of terrestrial rocks and application to impact cratering, *Meteoritics and Planetary Science*, 39(2), 233–246.

- Anderson, D. L., B. Minster, and D. Cole (1974), The effect of oriented cracks on seismic velocities, *J. Geophys. Res.*, *79*, 4,011–4,015.
- Ashby, M., and C. Sammis (1990), The damage mechanics of brittle solids in compression, *Pure Appl. Geophys.*, *133*, 489–521.
- Baldwin, E., L. Vocadlo, and I. Crawford (2005), Validation of autodyn in replicating large-scale planetary impact events, *LPSC 36th abstract*, p. 1380.
- Bate, M., and A. Burkert (1997), Resolution requirements for smoothed particle hydrodynamics calculations with self-gravity, *Mon. Not. R. Astron. Soc.*, *288*, 8060–8073.
- Benz, W., and E. Asphaug (1995), Simulations of brittle solids using smooth particle hydrodynamics, *Computer physics communications*, *87*, 253–265.
- Berge, P. A., J. G. Berryman, and B. P. Bonner (1993), Influence of microstructure on rock elastic properties, *Geophys. Res. Letter*, *4*, 2619–2622.
- Birch, F. (1960), The velocity of compression waves in rocks to 10 kilobars, *J. Geophys. Res.*, *65*, 1083–1102.
- Brace, W., and D. Riley (1972), Uniaxial deformation of 15 rocks to 30 kb, *Int. J. Rock. Mech. Min. Sci.*, *9*, 271–288.
- Brace, W., B. P. Jr, and C. Scholz (1966), Dilatancy in the fracture of crystalline rocks, *J. Geophys. Res.*, *71*, 3939–3953.
- Carter, W. J. (1978), Explosively produced fracture of oil shale, *Progress Report LA-7357-PR*, Los Alamos:, Los Alamos National Laboratory.

- Clegg, R., and C. Hayhurst (1999), Numerical modeling of the compressive and tensile response of brittle materials under high pressure dynamic loading, in *Shock compression of condensed matter–1999*, edited by M. Furnish, L. Chhabildas, and R. Hixson, pp. 321–324, American Institute of Physics, New York.
- Cohn, S. N., and T. J. Ahrens (1981), Dynamic tensile strength of lunar rock types, *J. Geophys. Res.*, *86*, 1,794–1,802.
- Collins, G., J. Melosh, and B. Ivanov (2004), Modeling damage and deformation in impact simulations, *Meteoritics & Planetary Science*, *39*, 217–231.
- Dahl, J., and P. Schultz (2001), Measurement of stress wave asymmetries in hypervelocity projectile impact experiments, *Int. J. Impact Eng.*, *26*, 145–155.
- Fujiwara, A. (1980), On the mechanism of catastrophic destruction of minor planets by high-velocity impact, *Icarus*, *31*, 277–288.
- Gault, D. (1978), Experimental studies of oblique impacts, *Proc. Lunar Planet. Sci. Conf.*, *9*, 3843–3875.
- Gilbert, G. (1893), The moons's surface, a study of the origin of its features, *Bull. Philos. Soc. Wash.*, *12*, 241–292.
- Grady, D., and M. Kipp (1987), Dynamic rock fragmentation, in *Fracture mechanics of rocks*, edited by B. Atkinson, pp. 429–475, Academic press, San Diego, California.
- Grady, D. E. (1998), Shock-wave compression of brittle solids, *Mechanics of Materials*, *29*, 181–203.

- Grady, D. E., and R. E. Hollenbach (1979), Dynamic fracture strength of rock, *Geophys. Res. Lett.*, *6*, 73–76.
- Grady, D. E., and L. Lipkin (1980), Criteria for impulsive rock fracture, *Geophys. Res. Lett.*, *7*, 255–258.
- Heinrich, K. (1991), *Ultrasonics fundamentals and applications*, Elsevier Science publishers LTD, New York.
- Hole, J. A. (1992), Nonlinear high-resolution three-dimensional seismic travel time tomography, *J. Geophys. Res.*, *97*, 6553–6562.
- Holsapple, K. A. (1993), The scaling of impact processes in planetary sciences, *Annu. Rev. Earth Planet. Sci.*, *21*, 333–73.
- Holsapple, K. A., and R. M. Schmidt (1982), On the scaling of crater dimensions 2. impact processes, *J. Geophys. Res.*, *87*, 1849–1870.
- Housen, K. R., and K. A. Holsapple (1990), On the fragmentation of asteroids and planetary satellites, *Icarus*, *84*, 226–253.
- Housen, K. R., R. M. Schmidt, and K. A. Holsapple (1983), Crater ejecta scaling laws: fundamental forms based on dimensional analysis, *J. Geophys. Res.*, *88*, 2485–2499.
- Hudson, J. A. (1990), Overall elastic properties of isotropic materials with arbitrary distribution of circular cracks, *Geophys. J. R. Astron. Soc.*, *102*, 465–469.
- Johnson, G., and T. Holmquist (1999), Response of boron carbide subjected to large strains, high strain rates, and high pressures, *J. Applied Phys.*, *85*, 8060–8073.

Johnston, D. H., M. N. Toksoz, and A. Timur (1979), Attenuation of seismic waves in dry and saturated rocks: II. mechanisms, *Geophysics*, *44*, 691–711.

Kachanov, M. (1993), Elastic solids with many cracks and related problems, *Adv. Appl. Mech.*, *30*, 259–445.

Kadono, T., and A. Fujiwara (2005), Cavity and crater depth in hypervelocity impact, *Int. J. Impact Eng.*, *31*, 1309–1317.

King, M. S. (2002), Elastic wave propagation in and permeability for rocks with multiple parallel fractures, *Int. J. Rock Mech. Min. Sci.*, *39*, 1033–1043.

Lange, M. A., and T. J. Ahrens (1983), The dynamic tensile strength of ice and ice-silicate mixtures, *J. Geophys. Res.*, *88*, 1197–1208.

Lange, M. A., T. J. Ahrens, and M. B. Boslough (1984), Impact-cratering and spall fracture of gabbro, *Icarus*, *58*, 383–395.

Levin, V., and M. Markvo (2005), Elastic properties of inhomogeneous transversely isotropic rocks, *Int. J. Solids and Structures*, *42*, 393–408.

Liu, C., and T. J. Ahrens (1997), Stress wave attenuation in shock-damaged rock, *J. Geophys. Res.*, *102*, 5243–5250.

Lockner, D. (1995), Rock failure, in *Rock physics and phase relations: A handbook of physical constants*, edited by T. Ahrens, pp. 127–147, American Geophysical Union, Washington DC.

- Love, S. G., F. Horz, and D. E. Brownlee (1993), Target porosity effects in impact cratering and collisional disruption, *Icarus*, *105*, 216–224.
- Lucy, L. (1977), A numerical approach to the testing of the fission hypothesis, *Astron. J.*, *82*, 1013–1024.
- Matsui, T., and H. Mizutani (1977), Why is a minor planet minor, *Nature*, *270*, 506–507.
- McQueen, R. G., S. P. Marsh, and J. N. Fritz (1967), Hugoniot equation of state of twelve rocks, *J. Geophys. Res.*, *72*, 4999–5036.
- Melosh, H. J. (1989), *Impact cratering, A Geological process*, Oxford Univ. Press, New York.
- Menke, W. (1989), *Geophysical data analysis: Discrete inverse theory*, Academic Press, San Diego.
- Monaghan, J. (1992), Smooth particle hydrodynamics, *Ann. Rev. Astron. Astrophys.*, *30*, 543–574.
- Murri, W. J., C. Young, D. A. Shockey, R. E. Tokheim, and D. R. Curran (1977), Determination of dynamic fracture parameters for oil shale, *Report PYD-5046*, final report to Sandia Laboratories, Stanford Research Institute.
- Nishizawa, O. (1982), Seismic velocity anisotropy in a medium containing oriented cracks—transversely isotropic case, *J. Phys. Earth.*, *30*, 331–347.
- Nur, A. (1971), Effects of stress on velocity anisotropy in rocks with cracks, *J. Geophys. Res.*, *76*, 2022–2034.

- O'Connell, R. J., and B. Budiansky (1974), Seismic velocities in dry and saturated cracked solids, *J. Geophys. Res.*, *79*, 5412–5426.
- O'Keefe, J., S. Stewart, M. Lainhart, and T. Ahrens (2001), Damage and rock-volatile mixture effects on impact crater formation, *Int. J. Impact Eng.*, *26*, 543–553.
- O'Keefe, J. D., and T. J. Ahrens (1976), Impact ejecta on the moon, in *Proceeding of 7th Lunar and Planetary Science Conference*, pp. 3,007–3,025.
- O'Keefe, J. D., and T. J. Ahrens (1981), Impact cratering: The effect of crustal strength and planetary gravity, *Revs. of Geophys. Space Phys.*, *19*, 1–12.
- Payne, J. (1965), Impacts of spherical projectiles of aluminum, stainless steel, titanium, magnesium, and lead into semi-infinite targets of aluminum and stainless steel, *Report AEDC-TR-65-34*, Arnold Eng. Develop. Center, Arnold Air Force Sta. Tenn.
- Petersen, C. (1969), Shock wave studies of selected rocks, Ph.D. thesis, Stanford University.
- Pierazzo, E., and J. Melosh (2000), Understanding oblique impacts from experiments, observations, and modeling, *Annu. Rev. Earth Planet. Sci.*, *28*, 141–167.
- Pilkington, M., and R. Grieve (1992), The geophysical signature of terrestrial impact craters, *Review of Geophysics*, *30*, 161–181.
- Pohl, J., D. Stoffer, H. Gall, and K. Ernstson (1977), The ries impact crater, in *Impact and Explosion Cratering*, edited by D. J. R. et al., pp. 343–404, Pergamon, New York.

- Polanskey, C. A., and T. J. Ahrens (1990), Impact spallation experiments: fracture patterns and spall velocities, *Icarus*, 87, 140–155.
- Ramsey, J., and F. Chester (2004), Hybrid fracture and the transition from extension fracture to shear fracture, *Nature*, 428, 63–66.
- Roddy, D. J., S. H. Schuster, K. N. Kreyenhagen, and D. L. Orphal (1980), Computer code simulations of the formation of meteor crater, arizona: Calculations mc-1 and mc-2, in *Proc. Lunar Planet. Sci. Conf.*, vol. 11, pp. 2,275–2,308.
- Schmidt, R. M., and K. R. Housen (1987), Some recent advances in the scaling of impact and explosion cratering, *Int. J. Impact Engng.*, 5, 543–560.
- Schock, R., H. Heard, and D. Stephens (1973), Stress-strain behavior of a granodiorite and two graywackes on compression to 20 kilobars, *J. Geophys. Res.*, 78, 5922–5941.
- Schultz, P., and R. Anderson (1996), Asymmetry of the mansion impact structure: evidence for impact angle and direction, *GSA Special Paper*, 302, 397–417.
- Schultz, P., and S. D'Hondt (1996), Cretaceous-tertiary (chicxulub) impact angle and its consequences, *Geology*, 24, 963–967.
- Shibuya, T., and I. Nakahara (1968), The semi-infinite body subjected to a concentrated impact load on the surface, *Bulletin of JSME*, 11, 983–992.
- Shipman, F. H., V. G. Gregson, and A. Jones (1971), A shock wave study of coconino sandstone, *NASA Report CR-1842*.

- Shoemaker, E. (1962), Interpretation of lunar craters, in *Physics and Astronomy of the Moon*, edited by Z. Kopal, pp. 283–359, Academic Press, New York.
- Shoemaker, E. M. (1963), Impact mechanics at meteor crater, arizona, *4*, 301–336.
- Simmons, G., T. Todd, and H. Wang (1973), The 25-km discontinuity: Implications for lunar history, *Science*, *182*, 158–161.
- Singh, M. M. (1989), Strength of rock, in *Physical properties of rocks and minerals*, vol. 2, edited by Y. S. Touloukian, W. R. Judd, and R. F. Roy, pp. 83–122, Hemisphere Publishing Corporation, New York.
- Tompkins, M. J., and N. I. Christensen (2001), Ultrasonic p- and s-wave attenuation in oceanic basalt, *Geophys. Int.*, *145*, 172–186.
- Vidale, J. E. (1990), Finite-difference calculation of traveltimes in three dimensions, *Geophysics*, *55*, 521–526.
- Weidner, D. J. (1987), Elastic properties of rocks and minerals, in *Methods of experimental physics*, edited by C. Sammis and T. Henyey, pp. 1–28, Academic press, San Diego, California.
- Wepfer, W., and N. Christensen (1990), Compressional wave attenuation in oceanic basalts, *J. Geophys. Res.*, *95*, 17,431–17,439.
- Winkler, K., and T. Plona (1982), Technique for measuring ultrasonic velocity and attenuation spectra in rocks under pressure, *J. Geophys. Res.*, *87*, 10,776–10,780.

Xia, K., and T. J. Ahrens (2001), Impact induced damage beneath craters, *Geophysical Research Letters*, 28, 3525–3527.